



Reservoir Mud Releasing May Suboptimize Fluvial Sand Supply to Coastal Sediment Budget: Modeling the Impact of Shihmen Reservoir Case on Tamsui River Estuary

Yu-Ta Hsueh¹, Fu-Chun Wu¹ , Qinghua Ye², Steven Y. J. Lai³, and Yinphan Tsang⁴

¹Department of Bioenvironmental Systems Engineering, National Taiwan University, Taipei, Taiwan, ²Deltares, Delft, The Netherlands, ³Department of Hydraulic and Ocean Engineering, National Cheng Kung University, Tainan, Taiwan, ⁴Natural Resources and Environmental Management, University of Hawai'i at Mānoa, Honolulu, HI, USA

Key Points:

- Increasingly adopted mud release strategy is effective to mitigate reservoir siltation yet suboptimal to alleviate coastal sediment deficit
- Flood-driven tributary-sourced sands dominate supply to coastal sediment budget yet sand delivery is reduced by mantling of released muds
- Sand delivery deficit (relative to sand delivery of clear-water flood release scenario) increases linearly with degree of bed mud saturation

Supporting Information:

Supporting Information may be found in the online version of this article.

Correspondence to:

F.-C. Wu,
fcwu@ntu.edu.tw

Citation:

Hsueh, Y.-T., Wu, F.-C., Ye, Q., Lai, S. Y. J., & Tsang, Y. (2024). Reservoir mud releasing may suboptimize fluvial sand supply to coastal sediment budget: Modeling the impact of Shihmen Reservoir case on Tamsui River estuary. *Water Resources Research*, 60, e2023WR036701. <https://doi.org/10.1029/2023WR036701>

Received 11 NOV 2023

Accepted 6 MAY 2024

Abstract Regular release of sediment from reservoir has been increasingly adopted as a strategy for sustainable management. Here, we use a process-based morphodynamic model to simulate the estuarine sediment dynamics impacted by turbidity current venting implemented by the Shihmen Reservoir during three typhoon events in 2008. Upon validation with the post-event bathymetries, the model hindcasts reveal that mud releasing can be effective in mitigating reservoir siltation, yet may be a suboptimal strategy for alleviating coastal sediment deficit. A vast majority of the released muds were delivered through the estuary and exported to offshore by flood advection, wave dispersion, and tidal flushing. The flood-driven sands, sourced mainly from downstream tributaries, were instead the major contributor to coastal sediment budget. However, mud mantling (covering and immobilizing sand deposits by the reservoir-released muds) reduced sand availability and thus sand delivery to the coast. For the present case, 25% of the released muds were deposited along the way, presence of these mud covers reduced sand delivery by 15%, compared to a hypothetical scenario of clear-water flood releases. The relative sand transport deficit is found to increase linearly with the degree of bed mud saturation, $1-D/R$, with D/R the ratio of single-event mud deposit to release. Given broad relevance to global reservoirs encountering the problems of siltation and coastal sediment deficit, our findings highlight that sustainable management needs to look beyond just a bulk amount of sediment, but it is critical to consider how different sediment fractions are interacting and impacted by human activities.

1. Introduction

Dams around the world impound rivers for water supply, power generation, flow regulation, and flood control. Reservoir behind dam traps sediment carried by the flow and interrupts their continuity, thereby altering the downstream flow and sediment regimes and reducing the storage capacity and useful life of a reservoir (Kondolf et al., 2014). Since fluvial sediment is an important source of the coastal sediment budget, the decline of fluvial sediment supply would lead to coastal erosion and wetland loss, rendering the global estuarine deltas such as the Mississippi, Rhône, Rhine-Meuse, Ebro, Nile, Volta, Mekong, and Yangtze at the risk of drowning in the face of sea level rise (Allison & Meselhe, 2010; Blum & Roberts, 2009; Boateng et al., 2012; Cox et al., 2021; Dunn et al., 2019; Darby et al., 2020; Dethier et al., 2022; Kondolf et al., 2018; Schmitt & Minderhoud, 2023; Schmitt et al., 2017; Syvitski et al., 2005; Tu et al., 2019; Warrick et al., 2019; Yang et al., 2014). To alleviate reservoir siltation and coastal sediment deficit, regular releases of sediment from reservoirs have been increasingly adopted as a strategy for sustainable management (Besset et al., 2017; Espa et al., 2019; Fruchard & Camenen, 2012; Kemp et al., 2016; Kondolf & Yi, 2022; Lee et al., 2022; Rovira & Ibáñez, 2007; Sumi, 2008; Wang et al., 2017).

Depending on their main objective, sediment release operations may be categorized as routing and flushing (Morris 2020a). The objective of routing is to pass the inflowing sediment-laden floods; flushing is aimed to remove the previously deposited sediments by hydraulic scour or resuspension (see Figure 1). For example, *drawdown sluicing* and *turbidity current venting* belong to the former, whereas *empty flushing* and *pressure flushing* belong to the latter. *Turbidity current venting* is only possible when the high-concentration density current has sufficient momentum and turbulence to sustain sediment in suspension and move as an underflow along the bottom (Chamoun et al., 2016).

The dominant type of sediment released from a reservoir depends largely on what was deposited closest to the dam (Asaeda & Rashid, 2012; Brandt & Swenning, 1999). Sediments transported and deposited in the reservoir

© 2024. The Author(s).

This is an open access article under the terms of the [Creative Commons Attribution-NonCommercial-NoDerivs License](https://creativecommons.org/licenses/by/4.0/), which permits use and distribution in any medium, provided the original work is properly cited, the use is non-commercial and no modifications or adaptations are made.

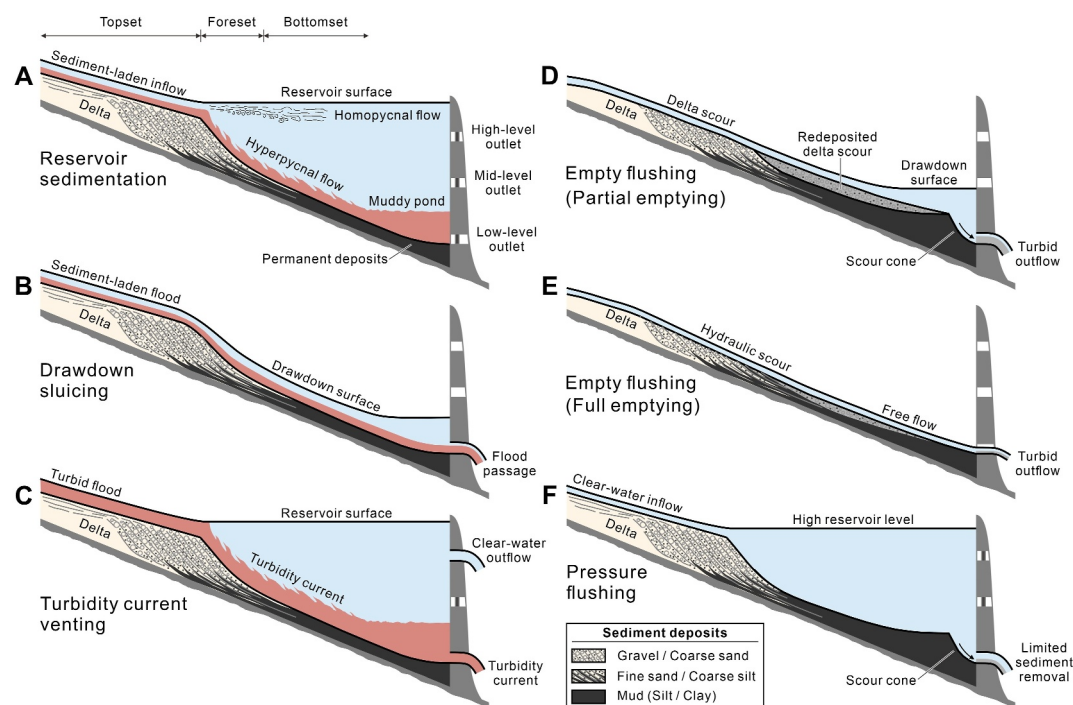


Figure 1. (a) Definition sketch of reservoir sedimentation. (b)–(c) Routing of inflowing sediment during floods by drawdown sluicing and turbidity current venting. Drawdown of water surface results in an increase of energy slope and sediment transport capacity, facilitating the passage of sediment-laden floods. Turbidity current venting is feasible when the density current has sufficient momentum and turbulence to sustain sediment motion along the bottom. The high-level outlet may be opened to concurrently release the clear water. (d)–(f) Removal of previously deposited sediment by empty flushing and pressure flushing. Drawdown of water surface during partial emptying stage facilitates hydraulic scour of delta. Free flows established during full emptying stage further enhance removal of the redeposited delta scour. Pressure flushing occurs when reservoir level is high and low-level outlet is opened to release sediment, producing a localized scour cone adjacent to the outlet. As there is no significant delta scour, removal of sediment by pressure flushing is limited to the area immediately upstream of the outlet.

exhibit a typical longitudinal gradation (Figure 1a) (Morris & Fan, 1998). The coarsest fractions (gravel and coarse sand) are transported as bedload and deposited along the topset of the delta in the upper reach of the reservoir. Finer fractions (fine sand and coarse silt) are transported as bedload and suspended load by hyperpycnal flows (turbidity currents) or homopycnal flows, and settling out as tapering deposits along the foreset and bottomset of the delta (Lai & Wu, 2021). The finest fractions, mud (silt and clay), are carried farther downstream by turbid underflows and can reach the dam to form a wedge-like muddy pond deposit (Schleiss et al., 2016; Toniolo et al., 2007). For an overview, we compiled 56 global cases of reservoir sediment release collected from the literature, distributed in 21 countries over six continents (Figure 2). Among all, 84% (=47/56) had mud as their main type of sediment released, of which 81% (=38/47) used empty flushing as the mode of operation (for a list of data, see Table S1 in Supporting Information S1). This highlights the fact that the global reservoir sediment releases are dominated by drawing down the water level to scour the muddy deposits distributed near the dam (Morris, 2020a).

Reservoir sediment releases can be also a solution to the issue of coastal sediment deficit. Field investigations revealed the importance of fluvial sediment supply in nourishing the estuarine deltas and wetlands (Allison, Nittrouer, et al., 2017; Gelfenbaum et al., 2015; Kemp et al., 2016; Nittrouer & Viparelli, 2014; Warrick et al., 2015, 2019; X. Wu et al., 2021). These field studies indicated that, although mud dominates the total sediment load delivered to the coastal waters, it is sand that actually accounts for the vast majority of coastal deposits building landforms and mitigating land losses. Sand is deposited mainly in the intertidal and shallow subtidal zones, while mud is transported farther to offshore, where a part is deposited on the seabed and resuspended by waves during high tides. Sands delivered to the coasts originate from scour of bed downstream of the dam, or the hillslope and channel erosion of the downstream tributaries (Wang et al., 2017; X. Wu et al., 2021).

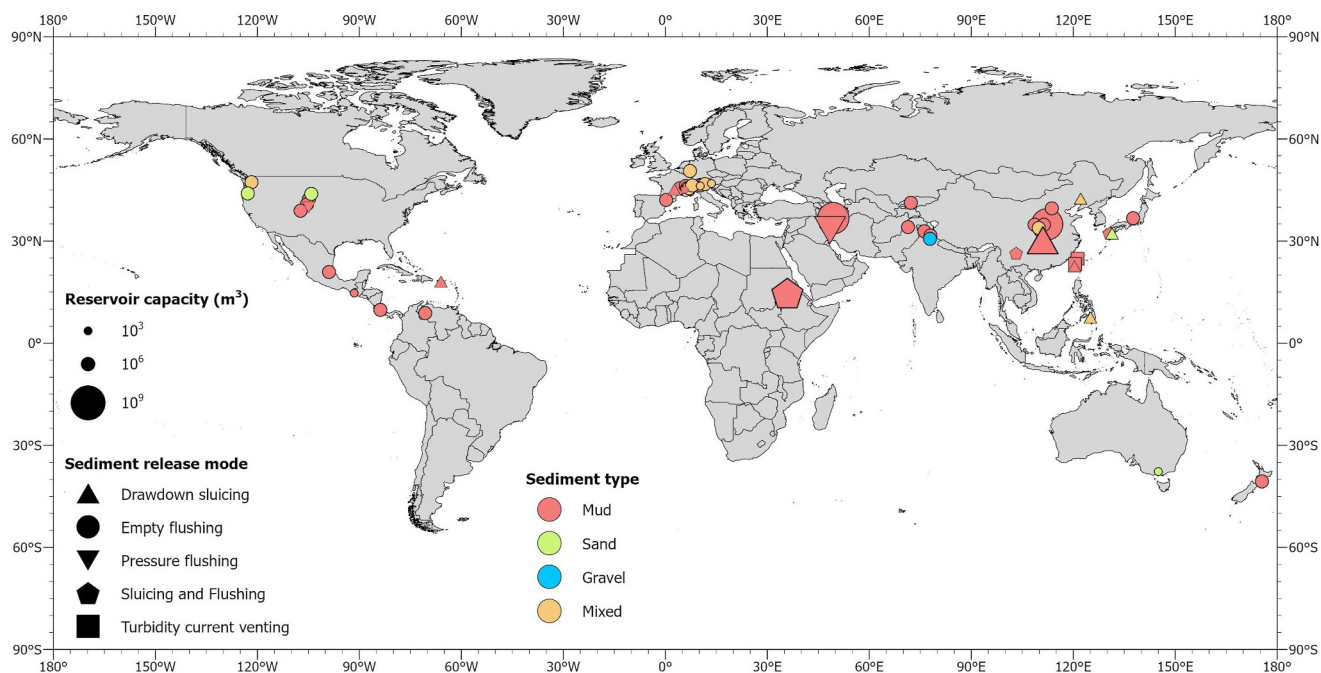


Figure 2. Global cases of reservoir sediment release. Operation mode of sediment release is represented by different symbols; main type of sediment released is represented by different colors; design capacity of the reservoir is represented by different symbol sizes. A total of 56 global cases, compiled from the literature, are distributed in 21 countries over 6 continents. Among all, 84% (=47/56) had mud as the main type of sediment released, of which 81% (=38/47) used empty flushing as the mode of operation.

Moreover, in the Mekong Delta the observed estuarine riverbed was mantled by mud layers, which was regarded as a key control on mobilization of sand from the riverbed (Allison, Dallon Weathers, & Meselhe, 2017). The effects of mud mantling on sand transport and thus on coastal sediment budget are highly relevant to the success of delta nourishment, yet these issues still remain to be elucidated.

To gain useful insights, we use a process-based morphodynamic model to simulate the sediment dynamics downstream of the dam and assess the impact of reservoir mud releases. We seek to answer the following research questions. (a) What are the impacts of the reservoir-released muds on estuarine and coastal sediment budgets? Specifically, what difference would it make were clear-water floods, instead of turbidity currents, released from the reservoir? (b) If the effects of mud mantling do exist, what impact do these reservoir-released muds have on fluvial sand transport? To answer question (a), we isolate the effect of mud releasing by simulation of a hypothetical scenario where clear-water floods were released from the reservoir. Contrasting the results of the mud-release scenario and the hypothetical clear-water release scenario allows us to identify the impact of mud releases on estuarine and coastal sediment budgets. To answer question (b), we track the fate (spatiotemporal distributions) of the reservoir-released muds, and quantify their mantling effect on fluvial sand transport. Lastly, we discuss the implications of our findings for strategies of sustainable sediment management.

2. Materials and Methods

2.1. Study Case: Shihmen Reservoir Mud Releasing

Shihmen Reservoir is located in Dahan River, a tributary of Tamsui River (Figure 3a). The latter is the largest estuary system in Taiwan, draining 2,730 km² and hosting the Taipei Metropolitan Area. The river mouth is bounded north eastly by the Fisherman's Wharf Causeway, south westly by the North Breakwater of the Taipei Port, and connected northwestward to the Taiwan Strait (Figure 3b). The littoral zone is subject to natural forcing such as tide, wave, river discharge, and typhoon (Hsieh et al., 2020). The semidiurnal M₂ tide is the principal constituent of astronomical tide. With a mean tidal range of 2.2 m and a spring tidal range up to 3 m, the estuary is classified as mesotidal (C. N. Chen & Tsai, 2017; W.-B. Chen et al., 2015), dominated by the southwestward flood currents and northeastward ebb currents. Waves and longshore currents are driven by strong northeast

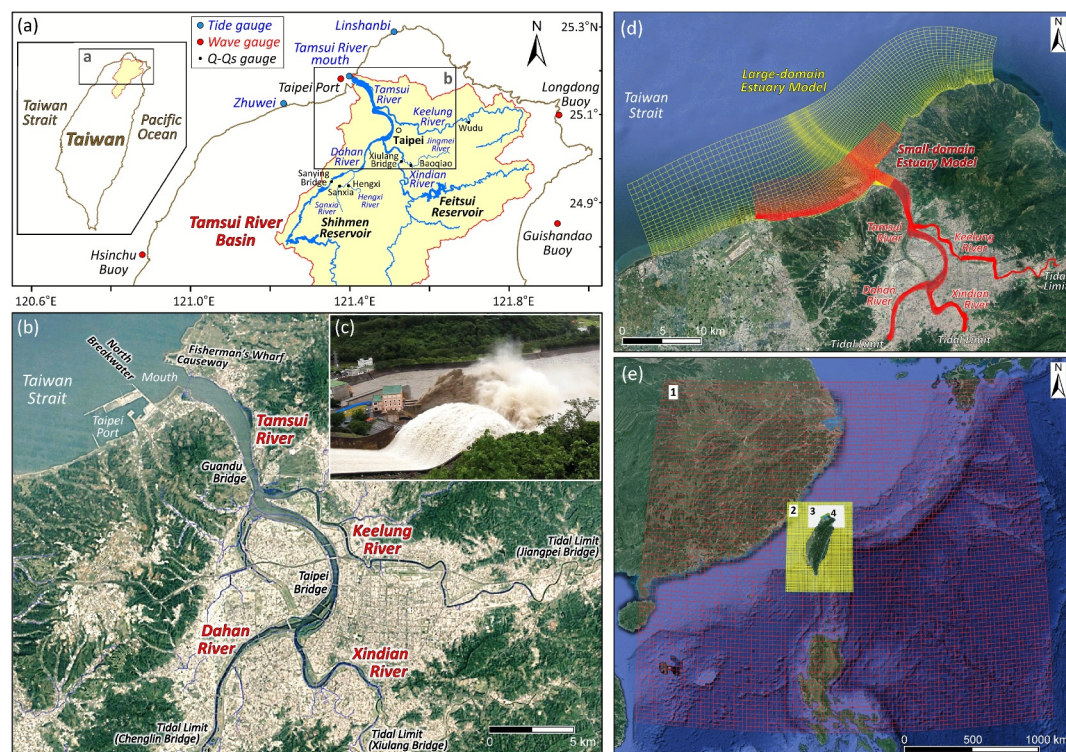


Figure 3. (a)–(b) Location maps: Tamsui River basin and estuarine system. (c) Turbidity current venting from the low-level mud sluiceway, and clear-water flood concurrently released from the high-level spillway of Shihmen Reservoir during Typhoon Soulik (2013). (d)–(e) Nested, orthogonal curvilinear grids. Estuary models: large-domain (yellow grid); small-domain (red grid). Wave models: 1—far-field open seas (red grid); 2—surrounding waters (yellow grid); 3—northern waters (white grid); 4—littoral zone (green grid). Image sources (b, d, and e) Google Earth; (c) Northern Region Water Resources Office, Taiwan.

monsoons in winters and weaker southwest monsoons in summers (Su et al., 2021). With a moderate wave climate (mean wave height of 1.4 m at the Taipei Port), the coastal area is subject to a tide-dominated mixed energy regime (Hayes, 1979). Tidal effect reaches upstream to three major tributaries, namely, Dahan, Xindian, and Keelung Rivers (Figure 3b), with their tidal limits located at Chenglin Bridge (31.3 km from river mouth), Xiulang Bridge (32.6 km from river mouth), and Jiangpei Bridge (39.4 km from river mouth). The annual mean flows of Dahan, Xindian, and Keelung Rivers are 40.3, 72.3, and 25.4 m³/s; flood peaks during typhoons can reach 6,000 m³/s in Dahan and Xindian Rivers, and 1,000 m³/s in Keelung River.

Tamsui River is the primary source of sand supply to the coastal sediment budget (Hong et al., 2000). Prior to 1958, the annual sediment delivery was 9.63 Mm³. After Shihmen and Feitsui Dams were built on Dahan and Xindian Rivers in 1964 and 1987 (Figure 3a), the annual delivery declined to 1.85 Mm³ (Lin et al., 2007). Shihmen Reservoir was built with seven outlet facilities, including three high-level outlets (a spillway; two flood tunnels), a mid-level outlet (an irrigation canal), and three low-level outlets (two power-plant penstocks; a bottom outlet). Large capacities of the high-level outlets and small capacities of the low-level outlets rendered the reservoir to discharge clear water and store turbid water during floods (Figure 1c), causing severe siltation problems (WRPI, 2008). Bathymetric records revealed that the cumulative siltation volume reached 106 Mm³ as of 2018, which exceeded 1/3 of the reservoir design capacity (NRWRO, 2022). The siltation was mainly composed of muds, as sand supplies from upstream of the Shihmen Reservoir rarely exceeded 5% of the sediment inflows (NRWRO, 2021).

For desiltation purposes, since 2008 Shihmen Reservoir has regularly implemented turbidity current venting during floods (Figure 3c), achieved by retrofitting one power-plant penstock into a dedicated mud sluiceway (Lee et al., 2022). Suspended sediment concentrations (SSC) of outflows have since been monitored routinely (WRPI, 2008). The retrofit project upgraded the capacity of the power-plant penstock from 70 to 300 m³/s

(NRWRO, 2022), increasing the mean sediment sluicing ratio (= ratio of sediment outflow to inflow) from 17% to 32% (S. T. Hsu & Wu, 2019). The mud releasing events that took place during three typhoons in 2008, Fung-Wong (7/24–8/2), Sinlaku (9/10–9/19), and Jangmi (9/24–10/3), are adopted here as the baseline scenario of hindcast simulation.

2.2. Model Description

We used the process-based morphodynamic model Delft3D (Lesser et al., 2004) to investigate the estuarine sediment dynamics in response to reservoir mud releasing. Delft3D consists of Flow, Wave, and Morphology modules that can be coupled to simulate the processes of fluvial-tidal-wave hydrodynamics, sediment transport, and morphological changes (for details see Text S1 in Supporting Information S1). It has been applied and validated in various environments (estuaries, coastal waters, inland rivers) over a wide range of timescales, such as long-term, centennial, decadal, sub-decadal, annual, sub-annual, seasonal and event scales (e.g., Gelfenbaum et al., 2015; Hibma et al., 2003; Hopkins et al., 2018; Lesser et al., 2004; Luan et al., 2017; Luijendijk et al., 2017; Meselhe et al., 2016; van der Wegen & Roelvink, 2008; van der Wegen et al., 2008, van der Wegen, Jaffe, & Roelvink, 2011; G. Wu et al., 2023; Zhu & Wiberg, 2022; Zhu et al., 2017).

The Flow Module can be run in 3D or depth-averaged 2DH mode. In this study 2DH mode was used, because significant sediment transports only occurred during typhoon periods when flood flows and turbidity currents were concurrently released from the reservoir. Under such extreme flow conditions, salinity intrusion and stratification of SSC in Tamsui River estuary are very limited (C. N. Chen & Tsai, 2017; W.-B. Chen et al., 2015; W.-C. Liu et al., 2007), rendering the 2DH approach an effective one for analyses of sediment budgets, as suggested by previous studies (Akter et al., 2021; Barrera Crespo et al., 2019; Nardin et al., 2020).

The Flow Module computes the flowfield using the unsteady shallow-water equation discretized on a rectangular staggered finite difference grid, and solves the system by an alternate direction implicit time-integration scheme. The Wave Module can be coupled to account for the enhanced bed shear stress due to wave-current interactions (Fredsoe, 1984; Soulsby et al., 1993), which plays a key role in the nearshore sediment resuspension. The resulting flowfield is used to compute the sediment transport field. Morphology module then uses this transport field to update the bed elevation and composition, based on the continuity equations of individual sediment fractions (Lesser et al., 2004):

$$(1 - \varepsilon) \frac{\partial z_b^{(i)}}{\partial t} = f_{\text{mor}} \left(D^{(i)} - E^{(i)} - \frac{\partial S_{bx}^{(i)}}{\partial x} - \frac{\partial S_{by}^{(i)}}{\partial y} \right) \quad (1)$$

where superscripts (i) imply that the quantities apply to the i th fraction; $z_b^{(i)}$ is bed elevation; ε is bed porosity; t is time; $D^{(i)}$ and $E^{(i)}$ are deposition and erosion fluxes between water column and bed surface; $(S_{bx}^{(i)}, S_{by}^{(i)})$ are bedload transport rates in (x, y) directions; f_{mor} is the morphological acceleration factor, introduced to deal with the gap between the hydrodynamic and morphodynamic timescales (see Section 2.3). The sediment mixture is comprised of non-cohesive sands ($>63 \mu\text{m}$) and cohesive muds ($<63 \mu\text{m}$). Sands are transported as bedload and suspended load, evaluated using the approach of van Rijn (1993) and van Rijn et al. (2001). Mud is transported as suspended load only, computed with the advection-diffusion equations and finite volume approximation (Deltares, 2014a), where $D^{(i)}$ and $E^{(i)}$ are treated as sink and source terms. For muds, $D^{(i)}$ and $E^{(i)}$ are evaluated via the Partheniades-Krone formulation (Partheniades, 1965) (for details see Text S1 in Supporting Information S1).

For each time step Δt , Equation 1 is used to calculate the fractional changes $\Delta z_b^{(i)}$ in each grid cell, the summation of $\Delta z_b^{(i)}$ over i yields the total change Δz_b . Bed composition is then updated by incorporating $\Delta z_b^{(i)}$ in the bed surface. As finer grains settle slower than coarser ones, finer fractions tend to be more prevalent in the upper part of the bed, covering coarser fractions and becoming more susceptible to erosion. To account for this, the erosion flux $E^{(i)}$ and bedload transports $(S_{bx}^{(i)}, S_{by}^{(i)})$ of fraction i are set proportional to its availability in the bed surface (Deltares, 2014a). In this way, the effect of mud mantling on sand erosion and transport is taken into account. Morphology module also includes a multi-layer stratigraphy model that keeps track of bed composition by bookkeeping the order in which sediments were deposited or eroded (for details see Text S1 in Supporting Information S1). In view of the sediment and hydrodynamic characteristics investigated in this study (see

Section 2.3), a surface layer of 0.2 m and 10 bookkeeping layers each of 1 m were chosen, based on those suggested for similar sediment mixtures and morphodynamics (Dissanayake et al., 2012; Geleynse et al., 2010; Valencia et al., 2023; van der Veegt et al., 2016; van der Wegen, Dastgheib, et al., 2011).

2.3. Model Setting

For simulations involving typhoons, the computational domain must be large enough to resolve the wind and atmospheric pressure fields, that is, large-scale meteorological forcing that affects waves and tides. Two sets of nested orthogonal curvilinear grid were generated. The first set was used for hydrodynamic and morphodynamic simulations focused on coastal and estuarine areas (Figure 3d). To save computational costs, a small-domain estuary model (red grid) was nested in a large-domain estuary model (yellow grid). The small-domain model covered the estuarine and nearshore areas, using finer grid (cell sizes: 50–350 m) to resolve local flow, sediment transport, and morphological processes. The large-domain model was extended to offshore (cell sizes: 150–800 m), providing hydrodynamic boundary conditions required by the small-domain model. To cover the propagation of tidal wave to its full extent, both models share the same river subdomains (cell sizes: 10–100 m), which used the tidal limits as the landward boundaries (for details see Text S2 in Supporting Information S1).

The second set of grid was used in the Wave Module (Figure 3e). To incorporate the typhoon tracks and swells that developed and propagated in open seas and to save computational costs, four layers of grid with increasing resolution were nested to supply boundary conditions layer by layer: (a) far-field open seas (red grid, cell sizes: 25 km); (b) surrounding waters (yellow grid, cell sizes: 5 km); (c) northern waters (white grid, cell sizes: 0.8–2 km); (d) littoral zone (green grid, cell sizes: 40–800 m). The littoral-zone wave models supplied offshore wave conditions required by the estuary models.

To pair with the grid, bathymetries of three different scales were derived. Bathymetries of river channels (Figure 4a) were interpolated from the cross-sectional surveys of 2008. Bathymetries of the nearshore and estuarine areas (Figure S1a in Supporting Information S1) were derived using the multibeam echo-sounding surveys of 2008. Bathymetries of the open seas (Figure S1b in Supporting Information S1) were retrieved from Taiwan Ocean Data Bank.

Boundary conditions were used to drive the Flow and Wave Modules. During typhoon periods, hourly flood hydrographs (Figure 5b) were specified on the landward tributary boundaries. Over the seaward boundary of the large-domain estuary model, time series of water levels were generated by eight primary astronomical tide constituents (M_2 , S_2 , N_2 , K_2 , K_1 , O_1 , P_1 , and Q_1). The amplitude and phase angle of each constituent were derived from the TPXO global tide model (Egbert & Erofeeva, 2002). Over the cross-shore lateral boundaries, Neumann boundary conditions were imposed for free development of water-level and velocity profiles (Roelvink & Walstra, 2004). For the Wave Module, wind fields at 10 m above sea surface, retrieved from the ERA5 reanalysis data of European Center for Medium-Range Weather Forecasts, were used. The ERA5 typhoon wind and atmospheric pressure fields (Figure S2 in Supporting Information S1) were also input to the large-domain estuary model to account for the tide level rises (or storm surges) caused by the meteorological forcing (Hu et al., 2009; Zhu & Wiberg, 2022).

During non-typhoon periods, the tributary boundaries were specified steady annual mean flows. The input reduction and morphological acceleration techniques (Roelvink & Reniers, 2012) were used to speed up the computation (for details see Text S3 in Supporting Information S1). Swells propagating from the far-field open seas are negligible under calm climate, thus only the littoral-zone wave model was used, with schematized *representative waves* specified on the seaward boundary, executed via a parallel computing approach. *Representative waves* are a set of partitioned waves with equal energy fluxes that best reproduce the longshore sediment transport by full wave climate (Figure S3 in Supporting Information S1) (Benedet et al., 2016). In addition, the schematized *morphological tide* (Figure 5c) and the morphological acceleration factor f_{mor} were also used. *Morphological tide* is aimed to reproduce the same morphological changes as the full tidal time series, using a shorter diurnal tidal period, which best retains the spring-neap cycle-averaged residual sediment transports (Figure S4 in Supporting Information S1) (Lesser, 2009). A value of $f_{\text{mor}} = 10$ was adopted herein, based on sensitivity tests over a range of values. These techniques were not used in Stage 1 as typhoon events demand a more detailed account of the processes involved (Luijendijk et al., 2017; G. Wu et al., 2023).

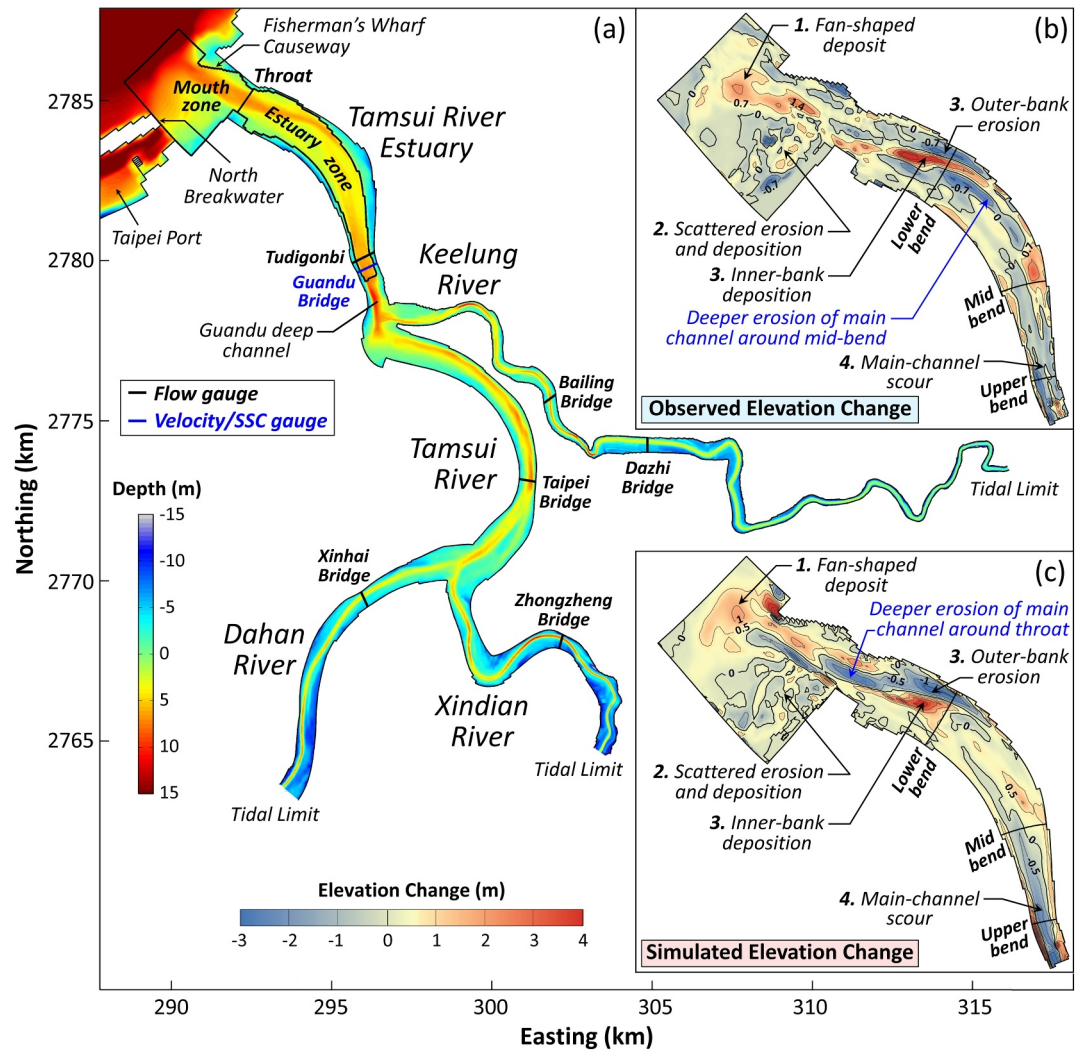


Figure 4. (a) Bathymetries of river channels, interpolated from cross-sectional surveys of 2008 using an elliptical inverse distance weighted method (Merwade et al., 2006). The high-resolution, multibeam echo-sounding bathymetries of the validation area (covering a mouth zone and an estuary zone, bounded by thick black lines) were used for validation of morphological changes. (b)–(c) Observed and simulated bed elevation changes after Scenario 1. Observed main channel had deeper erosion around the mid bend, while simulated main channel had deeper erosion at the throat. Four common morphological features were identified, which are numbered by 1–4.

Three sand and two mud fractions were considered in this study: (a) coarse, medium, and fine sands with $D_{50} = 500, 200,$ and $100 \mu\text{m}$, based on data collected from Tamsui River estuary and its nearshore area (TRMO, 2015); (b) coarse ($8\text{--}63 \mu\text{m}$) and fine ($<8 \mu\text{m}$) muds with settling velocities $w_s = 0.26$ and 0.011 mm/s , determined from sensitivity tests that reproduced the observed SSC and depositional patterns. The effect of flocculation on settling velocity was not considered since salinity intrusion was negligible during typhoons. These sediment fractions were used in the bed material and SSC inputs. An initial bed composition was generated with an iterative approach presented by van der Wegen, Dastgheib, et al. (2011), using the observed spatial data (TRMO, 2015) as a starting point. The observed time series of reservoir outflow SSC during the mud release events were used as the mud inputs to the Dahan River. The proportions of coarse and fine fractions in the mud SSC were 40% and 60%, based on the data sampled from the bottom outlet (WRPI, 2008). Over the landward boundaries, the time series inputs of sand SSC were specified with the flow versus suspended sand load ($Q\text{--}Q_s$) rating curves (for details see Text S4 in Supporting Information S1) derived from the long-term records (1991–2018) at six gauges on the downstream tributaries (Figure 3a), namely, Sanying Bridge, Sanxia, Hengxi, Xiulang Bridge, Baoqiao and Wudu. The proportions of coarse, medium, and fine sands in the SSC were also determined

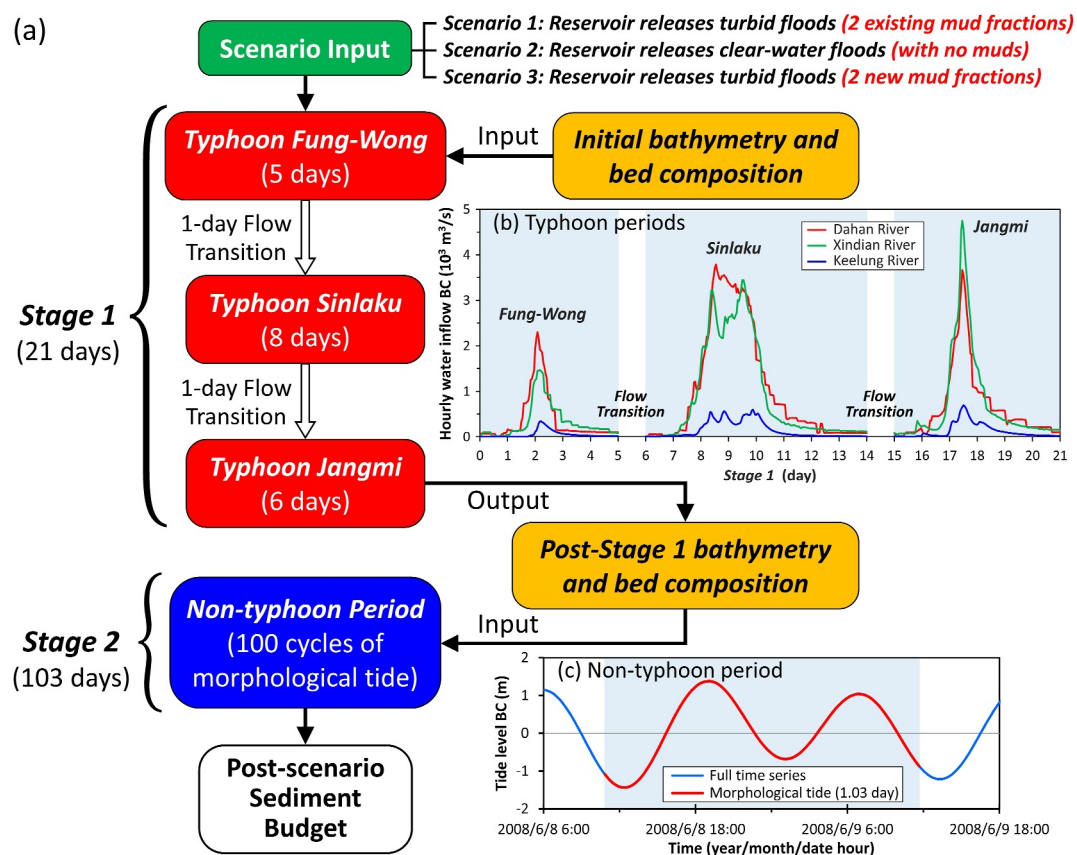


Figure 5. (a) Flowchart of scenario simulations. Mud release events during three typhoons were simulated consecutively in Stage 1, followed by tidal cycles during non-typhoon periods in Stage 2. (b) Hourly water inflow boundary conditions used in Stage 1. The 21-day duration encompassed three typhoons (19 days) and two 1-day flow transitions in between. (c) Morphological tide used in Stage 2. The 103-day duration was schematized by 100 cycles of morphological tide. During Stage 2, water inflows from tributary boundaries were specified steady annual mean flows.

with the iterative approach (van der Wegen, Dastgheib, et al., 2011). The SSC on the seaward boundaries were set to be zero since they were negligible compared to the fluvial SSC inputs (Lin et al., 2017). The calibrated parameter values of the Flow/Morphology Modules are summarized in Table S2 in Supporting Information S1. For the remaining parameters (including those of the Wave Module), the default values were used (Delatares, 2014a, 2014b).

2.4. Scenario Simulations

Three scenario simulations were performed. Scenario 1 is a *baseline scenario* aimed to mimic the mud release events that took place during three typhoons in 2008. The hindcast results may as well be used for model validation. Scenario 2 is a *hypothetical scenario* where clear-water floods (of zero SSC) were released from the reservoir, with the same hydrographs as used in Scenario 1. This is equivalent to 100% trapping of sediment inflow to the reservoir. Contrasting the results of Scenarios 1 and 2 allows us to unravel the effect of mud releasing on coastal sediment budget. Scenario 3 is a *tracking scenario* where the reservoir-released muds were distinguished from the preexisting ones, achieved by including two additional mud fractions. The mud fractions released from the reservoir were identical to the preexisting ones but were assigned new codes, that is, mud_Res_c and mud_Res_f for the coarse and fine muds. As a result, a total of seven fractions (three sands, two preexisting muds, and two additional muds) were used in this scenario. Scenario 3 enables us to track the fate of the reservoir-released muds, and quantify their impact on fluvial sand transport.

The flowchart of scenario simulations is shown in Figure 5a, the model setup is summarized in Table 1. Mud release events during three typhoons were simulated consecutively in Stage 1 (21 days), followed by tidal cycles

Table 1
Model Setup for Scenario Simulations

Module	Stage	Model setup	Values or data used
Flow/Morphology	Stage 1 (typhoon periods)	Grid	2 nested layers (with different scales and sizes)
		Typhoon wind field and atmospheric pressure field	ERA5 reanalysis data (input to large-domain estuary model for storm surge effects)
		Time step	0.1 min
		Flow spin-up interval	1 day
		Morphology spin-up interval	1 day
		Duration of flow simulation	21 days
		Duration of morphology simulation	19 days (= duration of three typhoon events)
		Tributary inflow discharges	Hourly flow data
		Tributary inflow sand SSC	Rating curves
		Mud inflow to Dahhan River	Scenarios 1 and 3; reservoir outflow mud SSC
			Scenario 2: none (clear-water flood releases)
			Time series of tide level generated by eight primary astronomical tide constituents
			Neumann boundary conditions
			0 g/L
		Wave	Stage 2 (non-typhoon periods)
Time step	0.2 min		
Flow spin-up interval	1.03 days (1 cycle of <i>morphological tide</i>)		
Morphology spin-up interval	4.12 days (4 cycles of <i>morphological tide</i>)		
Duration of flow simulation	10.3 days (10 cycles of <i>morphological tide</i>)		
Morfac f_{mor} (duration of morphology simulation)	10 (103 days = 10 times the duration of flow simulation)		
Tributary inflow discharges	Annual mean flows (Dahan: 40.3 m ³ /s; Xindian: 72.3 m ³ /s; Keelung: 25.4 m ³ /s)		
Tributary inflow sand SSC	Rating curves		
Mud inflow to Dahhan River	None (no mud releases)		
Tide level on seaward boundary	Repeated cycles of <i>morphological tide</i>		
Water level and velocity on cross-shore boundaries	Neumann boundary conditions		
SSC on seaward boundaries	0 g/L		
	4 nested layers (with different scales and sizes)		
	Typhoon wind field (ERA5 reanalysis data)		
	30 min		
	1 layer (littoral-zone wave model)		
	5 <i>representative waves</i> (run in parallel)		
	30 min		

during non-typhoon periods in Stage 2 (103 days). This two-stage simulation strategy was adopted for two reasons. First, as stated above, four layers of wave models were used in Stage 1 while only one layer was used in Stage 2. Second, the schematization/acceleration techniques were used in Stage 2 but not in Stage 1. Use of different model setups and computational techniques in Stages 1 and 2 motivated us to perform these simulations separately. Such strategy is most useful when substantial differences in the magnitude and rate of morphological change are present between different stages (Roelvink & Reniers, 2012).

Prior to Stage 1, a 24-hr flow spin-up and a 24-hr morphology spin-up without morphological updating were performed. Stage 1 included three typhoons total of 19 days, and two 1-day transition periods in between. This 1-day period was deemed sufficient for smooth transitions of flow and SSC, during which most residual suspended muds would settle out since the estuarine baroclinic circulation induced by salinity intrusion was not considered in 2DH model, lacking the drive for sustaining muds in suspension. Morphology module was turned off during flow transitions, so the bed topography and composition remained unchanged. After Stage 1, the output bathymetry and bed composition were input to Stage 2, whose simulation was performed for 100 cycles of *morphological tide* (103 days). The total duration of Stages 1 and 2 was 124 days, consistent with the time interval between the pre- and post-event bathymetric surveys that were conducted in June and October 2008. The time steps used in Stages 1 and 2 were 0.1 and 0.2 min, based on a series of sensitivity tests aimed to secure numerical stability and accuracy, that is, the CFL condition. The Wave and Flow Modules were coupled every 30 min. The computation time required for a scenario simulation was 72 hr (48 and 24 hr for Stages 1 and 2) using an Acer Altos P30 F6 workstation.

2.5. Model Validation

The hydrodynamics, SSC, and morphological changes during typhoon and non-typhoon periods were used for model validation. The water levels, velocities, wave heights, and SSCs used were from 14 gauging stations (locations see Figures 3a and 4a). These include: (a) 3 tide gauges in the northeast and southwest coasts of the river mouth; (b) 6 flow gauges, 2 in Tamsui River, 1 in Dahan River, 1 in Xindian River, and 2 in Keelung River; (c) a velocity/SSC gauge in Tamsui River; (d) 4 wave gauges along the northern nearshore. The high-resolution, multibeam echo-sounding bathymetries of the validation area were used for morphological changes, this area covers a mouth zone and an estuary zone (Figure 4a). The former is bounded by the 20 m isobath, Fisherman's Wharf Causeway, and North Breakwater of the Taipei Port; the latter is a 40° bend connected to the mouth via a 700-m-wide throat and bounded upstream by a cross-section near Guandu Bridge. In addition, 3 cross-sections from the lower, mid, and upper bends (locations see Figures 4b and 4c) were used for validation of the transverse morphological changes.

Three statistical metrics used to assess the model performance include the bias, root mean square error (RMSE) and Willmott skill score, defined as follows:

$$\text{Bias} = \frac{1}{n} \sum_{i=1}^n (X_{\text{mod},i} - X_{\text{obs},i}) \quad (2)$$

$$\text{RMSE} = \sqrt{\frac{1}{n} \sum_{i=1}^n (X_{\text{mod},i} - X_{\text{obs},i})^2} \quad (3)$$

$$\text{Skill} = 1 - \frac{\sum_{i=1}^n |X_{\text{mod},i} - X_{\text{obs},i}|^2}{\sum_{i=1}^n (|X_{\text{mod},i} - \bar{X}_{\text{obs}}| + |X_{\text{obs},i} - \bar{X}_{\text{obs}}|)^2} \quad (4)$$

where X_{mod} and X_{obs} = modeled and observed values; \bar{X}_{obs} = mean observed values; n = number of observed values. A positive or negative bias indicates a trend of overestimation or underestimation. The RMSE represents the mean deviation of the modeled from the observed value. A skill score of 1 indicates perfect model performance, skills ranging 1–0.65, 0.65–0.5, and 0.5–0.2 indicate excellent, very good, and good model performances, while poor performances for <0.2 (Willmott, 1981). For hydrodynamic and morphodynamic simulations in the estuarine and coastal areas, the skill scores of water level and velocity are usually higher than those of wave height, SSC, and morphology due to greater uncertainties present in the computations of waves and sediment

Table 2
Statistical Metrics of Model Performances

Category	Validation data (event or time period)	Station (or site)	Statistical metrics		
			Bias	RMSE	Skill
Tide	Water level (non-typhoon period, 6/10–7/9, 2008)	Linshanbi	−0.03 (m)	0.11 (m)	0.99
		Tamsui River mouth	−0.01 (m)	0.10 (m)	1.00
		Zhuwei	−0.02 (m)	0.10 (m)	1.00
Flow	Water level (Typhoon Sinlaku, 9/10–9/19, 2008)	Linshanbi	0.00 (m)	0.13 (m)	0.99
		Tamsui River mouth	0.05 (m)	0.13 (m)	0.99
		Zhuwei	−0.03 (m)	0.14 (m)	0.99
		Tudigonbi	−0.10 (m)	0.16 (m)	0.99
		Taipei Bridge	−0.07 (m)	0.17 (m)	0.99
		Xinhai Bridge	−0.09 (m)	0.23 (m)	0.99
		Zhongzheng Bridge	−0.10 (m)	0.18 (m)	1.00
		Bailing Bridge	−0.25 (m)	0.39 (m)	0.96
		Dazhi Bridge	−0.32 (m)	0.55 (m)	0.93
		Guandu Bridge	0.05 (m/s)	0.19 (m/s)	0.97
		Taipei Bridge	0.02 (m/s)	0.11 (m/s)	0.99
		Xinhai Bridge	0.00 (m/s)	0.07 (m/s)	0.98
		Zhongzheng Bridge	0.08 (m/s)	0.14 (m/s)	0.75
Wave	Significant wave height (Typhoon Sinlaku, 9/10–9/20, 2008)	Taipei Port	−0.21 (m)	0.33 (m)	0.97
		Hsinchu Buoy	0.15 (m)	0.40 (m)	0.95
		Longdong Buoy	0.01 (m)	0.59 (m)	0.97
		Guishandao Buoy	0.40 (m)	0.62 (m)	0.95
		Guandu Bridge	−0.31 (g/L)	0.60 (g/L)	0.71
Sediment Transport	SSC (Typhoon Fung-Wong, 7/24–8/2, 2008)		−0.62 (g/L)	1.19 (g/L)	0.83
	SSC (Typhoon Sinlaku, 9/10–9/19, 2008)		−0.68 (g/L)	0.97 (g/L)	0.77
	SSC (Typhoon Jangmi, 9/24–10/3, 2008)				
Morphological Change	Bed elevation change	Entire validation area	−0.04 (m)	0.57 (m)	0.65
	Cross-sectional bed profile change	Lower-bend (XS-LB)	0.15 (m)	0.63 (m)	0.98
		Mid-bend (XS-MB)	−0.25 (m)	0.41 (m)	0.99
		Upper-bend (XS-UB)	0.30 (m)	0.87 (m)	0.98

transports (Zhu & Wiberg, 2022). As such, a skill score of 0.7 for wave height and SSC, and 0.65 for morphology are normally perceived as reasonably excellent performances. The statistical metrics of all validation results are summarized in Table 2. To see the outcomes in terms of water level, velocity, wave height, and SSC, the readers are referred to Text S5 and Figures S5–S9 in Supporting Information S1 therein.

In view of the skill scores, overall, the model performances are excellent in reproducing the tide and water levels, flow velocities, wave heights, and SSC observed during typhoon and non-typhoon periods. The RMSE of tide levels are <5% of the mean tidal range; the RMSE of river flood levels are $O(10^{-1})$ m at most gauges. Both of these exhibit a slight trend of underestimation. The estuarine velocity reversal and asymmetric flow over a tidal cycle were well captured, with the RMSE being $O(10^{-2}–10^{-1})$ m/s. The modeled and observed wave heights during typhoon exhibit good agreement, with the RMSE at the Taipei Port <25% of the mean wave height. Wave height and estuarine flow velocity both exhibit a slight trend of overestimation. For SSC, the skill scores ranging 0.71–0.83 indicate a reasonably excellent model performance. The sustained high SSC (Figures S9a–S9c in Supporting Information S1) observed during the post-peak low-flow periods of Sinlaku and Jangmi and during lower floods of Fung-Wong are attributed to the well-known local turbidity maximum present near the Guandu Bridge (W.-B. Chen et al., 2015; M.-H. Hsu et al., 2006; W.-C. Liu et al., 2022, 2007). This local turbidity maximum is induced by salinity intrusion and estuarine baroclinic circulation that occur particularly during low

flows, trapping suspended sediment in the Guandu deep channel (see Figure 4a and Figure S9d in Supporting Information S1 for locations). Although such locally sustained high SSC during low flows were not reproduced by the 2DH model, its effects on the model domain would be minimal given the tributary inflow flood hydrographs used in Stage 1 and the moderate annual mean flows used in Stage 2 (see Section 2.3).

Figures 4b and 4c show the observed bed elevation change and the simulated result from Scenario 1. Overall, the simulated result is in satisfactory agreement with the observed, except that the observed main channel had deeper erosion around the mid bend while the simulated result had deeper erosion at the throat. Four common features are identified. (a) A fan-shaped deposit off the mouth toward the seaward boundary, attributable to the swinging of exiting jet flows over tidal cycles during typhoons (Figure S10 in Supporting Information S1). Moreover, waves exerted additional bed shear stress causing resuspension and transport of bottom sediments, spreading out an otherwise concentrated mouth deposit (Figure S11 in Supporting Information S1). (b) On the south of the fan-shaped deposit was a subzone of scattered erosion and deposition (bounded by North Breakwater and land boundary). This was also attributed to the wave actions as the wave-induced bed shear stress resuspended and transported the otherwise evenly deposited sediments. (c) At the lower bend, substantial amounts of outer-bank erosion and inner-bank deposition were observed. (d) At the narrow upper bend, distinct scour of the main channel, as much as 1.5 m, was present.

To facilitate further validation, we present areal and volumetric histograms of the observed and simulated bed elevation changes (Figure S12 in Supporting Information S1). Overall, the simulated and observed histograms are in satisfactory agreement. The simulated *total volume change* (= sum of absolute volume changes) and *net volume change* (= deposition volume—erosion volume) were smaller than the observed ones by 10%–20%. Such trend of underestimation was reflected by a negative bias of -0.04 m; the RMSE of 0.57 m implied mean relative errors of 16% and 14% for *total* and *net volume changes*. We looked into the histograms of individual zones, and found that these errors arose mainly from the estuary zone, due in part to the uncertainties in the $Q-Q_s$ rating curves used for tributary sand SSC inputs, and factors not considered in this study (see Section 4.3). Nevertheless, a cell-by-cell comparison of the simulated and observed bed elevation changes yields a skill score of 0.65, suggesting a reasonably excellent model performance. We also compared the observed and simulated transverse bed profiles (Figure S13 in Supporting Information S1) along three cross-sections in the lower, mid, and upper bends (see Figures 4b and 4c for locations). The skill scores ranging 0.98–0.99 indicate an excellent model performance. In sum, the model hindcast reproduced satisfactorily the observed morphological changes.

3. Results

3.1. Scenario 1: Baseline Mud Release Events

Based on the simulation results from typhoon and non-typhoon periods, we derived the stage-wise maps of bed elevation change (Figures 6a and 6b), where the cumulative sediment transports and zonal sediment budgets are also shown. Below, we present separately the results of Stages 1 and 2.

3.1.1. Stage 1—Typhoon Periods

The morphological change during Stage 1 (Figure 6a) highly resembled the full morphological change of Scenario 1 (Figure 4c), indicating that the morphologic development mainly took place in Stage 1. Moreover, the cumulative sediment transports (white arrows) were all seaward, suggesting that the morphological change was dominated by fluvial sediment supplies during typhoons. In total, 6.96 M ton of sediment was delivered to the estuary zone, of which 82% (5.68 M ton) was further transported to the mouth zone, rendering a net budget of $+0.72$ Mm³ in the estuary zone. The total input to the mouth zone, 6.13 M ton, was the sum of fluvial supply (5.68 M ton) and wave-induced longshore drift (0.45 M ton) (see Figures S11a and S11c in Supporting Information S1 for longshore currents and the induced scour). The amount of sediment exported to offshore, 4 M ton, was 65% of the total input to the mouth zone; the resulting net budget, $+1.35$ Mm³, was nearly twice the budget in the estuary zone.

Breaking down the budgets of individual typhoon events, we present in Figure 6c the event-wise zonal sediment budgets. Sediment budgets in the two zones were positive during Stage 1. In either zone, Sinlaku played the most pivotal role, contributing >70% of the total budgets due to the longest flood duration (Figure 5b);

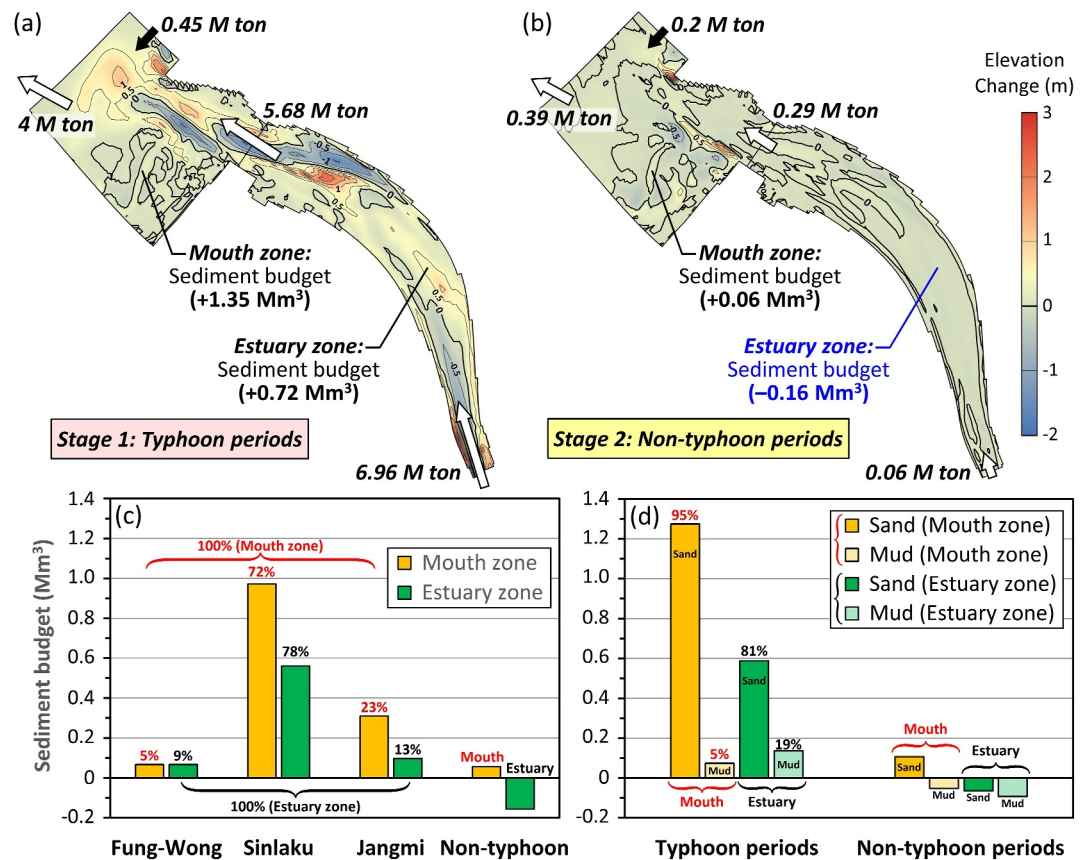


Figure 6. Simulation results of Scenario 1 (baseline). (a–b) Bed elevation changes, cumulative sediment transports, and zonal sediment budgets during Stage 1 (typhoon periods) and Stage 2 (non-typhoon periods). White arrows indicate directions of sediment transport by fluvial flows and tidal currents; black arrows indicate directions of sediment transport by wave-induced longshore currents. (c) Event-wise sediment budgets in mouth and estuary zones. (d) Sand and mud budgets in mouth and estuary zones during typhoon and non-typhoon periods.

Jangmi, despite the largest peak, contributed <25% of the total budgets due to its short duration; Fung-Wong accounted for <10% of the total budgets due to the smallest flood magnitude and duration. Echoing the trend presented in Figure 6a, the event-wise sediment budgets in the mouth zone were consistently greater than those in the estuary zone.

Breaking down the contributions of sand and mud fractions, we show in Figure 6d the fractional zonal sediment budgets. In either zone, sand was the major contributor to the sediment budget. Sand contributed 95% of the budget in the mouth zone and 81% of the budget in the estuary zone (see Text S6; Figures S14a and S14b in Supporting Information S1). As no sand was released from the reservoir, these sand budgets were mainly sourced from hillslope and channel erosion of the tributaries. During Stage 1, 3.62 M ton of sand and 3.34 M ton of mud were input by river flows, 0.35 M ton of sand and 0.09 M ton of mud were input by longshore currents. The total inputs of sand and mud, 3.97 and 3.43 M ton, differed a little, yet sands and muds exported to offshore, 0.83 and 3.17 M ton, were of notable difference. Specifically, 80% of sand input was deposited yet 92% of mud input was exported. Of the total sand deposit (1.87 Mm³), 70% was in the mouth zone, whereas only 30% of the mud deposit (0.21 Mm³) was in the mouth zone. These results corroborate the earlier observation, that is, the fan-shaped deposit off the Tamsui River mouth was mainly composed of sandy river-borne sediments transported by floods (Hong et al., 2000). In the estuary zone, the mud deposit (0.14 Mm³), despite less than 1/4 of the sand deposit (0.59 Mm³), revealed that during the release events muds did make a small contribution to the estuarine sediment budget (see Section 3.3).

3.1.2. Stage 2—Non-Typhoon Periods

Due to weak bed shear stress during non-typhoon periods (Figure 6b), the total sediment supply (0.06 M ton) was two orders of magnitude smaller than that of Stage 1 (6.96 M ton), among which sand supply 0.002 M ton (Figure S14c in Supporting Information S1) was three orders of magnitude smaller, mud supply 0.06 M ton (Figure S14d in Supporting Information S1) was two orders of magnitude smaller. During Stage 2, sediments deposited in the estuary zone during typhoon periods were resuspended and transported by tidal currents. Due to tidal asymmetry (W.-C. Liu et al., 2022), seaward sediment transport during ebb tides was greater than landward transport during flood tides, leading to a seaward residual transport and a negative budget -0.16 Mm^3 in the estuary zone, of which 60% was mud and 40% was sand (Figures 6c and 6d). The residual transport to the mouth zone, 0.29 M ton (with 70% mud), plus the input of longshore drift, 0.2 M ton (with 85% sand), was mostly (80%) exported to offshore. The net budget in the mouth zone, $+0.06 \text{ Mm}^3$ (with $+0.11 \text{ Mm}^3$ sand and -0.05 Mm^3 mud), was $<1/20$ the net budget of Stage 1 ($+1.35 \text{ Mm}^3$).

3.1.3. Summary of Key Findings

Model hindcast reveals that the flood-driven sand, sourced from hillslope and channel erosion of the downstream tributaries, was the major contributor to the estuarine and coastal sediment budgets. During typhoon periods, a total of 4.19 M ton of sand was supplied from the downstream tributaries (Figure 3a), of which 73% was from Xindian and Jingmei Rivers, 26% was from Dahan, Sanxia, and Hengxi Rivers, 1% was from Keelung River; 86% of these sand supplies reached the estuary zone. In the wave-affected mouth zone, sand accounted for 98% of the total sediment deposit, where 92% took place during typhoons. Despite a vast amount of mud released from the reservoir, muds transported to the mouth zone were almost entirely ($>97\%$) exported to offshore by flood advection and wave dispersion. These results coincide with the observations from the world's mouth bar deposits, which remain sandy in spite of the mud-dominated sediment supply (see Braat et al. (2023), van der Veet et al. (2020), and references therein). In the tide-dominated estuary zone, sand also contributed $>90\%$ of the sediment deposit. During non-typhoon periods, tidal currents resuspended and transported seaward those sediments deposited during typhoons. The amount of mud so eroded was 50% more than the amount of sand so eroded. Observations on the flushing of estuarine mud deposits by tidal currents have been reported by, for example, Guo et al. (2014) and Braat et al. (2017).

These results motivated us to seek answers to the research questions posed in Section 1. To be specific, we aim to unravel the mantling effect of the reservoir-released muds on transport of sands. In the following sections, Scenario 2 isolates the effect of mud releasing, while Scenario 3 tracks the fate of the reservoir-released muds.

3.2. Scenario 2: Hypothetical Clear-Water Flood Releases

Two outcomes of Scenario 2 deserve special attention. First, bed elevation changes of Scenario 2 were very similar to those of Scenario 1 (Figures S14e–S14f in Supporting Information S1). Cell-by-cell comparison yields a coefficient of determination $R^2 = 0.99$, indicating highly coherent morphological changes. Hence, whether muds were included in the reservoir-released floods did not affect substantially the resulting morphologies. While such outcome confirmed the result noted earlier (i.e., sand was the major landform builder), second, the zonal sediment budgets of Scenarios 1 and 2 did exhibit distinct differences. Relative to Scenario 1, sediment budgets of Scenario 2 increased by 0.193 Mm^3 in the mouth zone yet decreased by 0.045 Mm^3 in the estuary zone. To look into the details, we show in Figure 7 the zonal sand and mud budgets from Scenarios 1 and 2. An apparent trend emerged, that is, Scenario 2 had greater sand budgets yet negative mud budgets. Specifically, for Scenario 2, the increase of total sediment budget in the mouth zone was attributed to the larger surplus of sand budget over the deficit of mud budget, while the reduction of total budget in the estuary zone was due to the larger deficit of mud budget over the surplus of sand budget.

The deficits of mud budget with Scenario 2 are no surprise, as no muds were released from the reservoir and only muds preexisting in the downstream channels were eroded by floods. To explain the surpluses of sand budget with Scenario 2, we show in Figure 8 the post-Stage 1 bed mud contents of Scenarios 1 and 2. Throughout the estuary system, bed mud contents of Scenario 2 were invariably lower. For example, at three selected cross-sections (Taipei and Guandu Bridges, and River Mouth), bed mud contents of Scenario 2 were 12%, 8%, and 5% lower than the corresponding ones of Scenario 1. Lower mud contents meant higher sand contents, which in turn led to higher sand transport rates (as described in Section 2.2) and thus larger sand budgets. Based on the results of

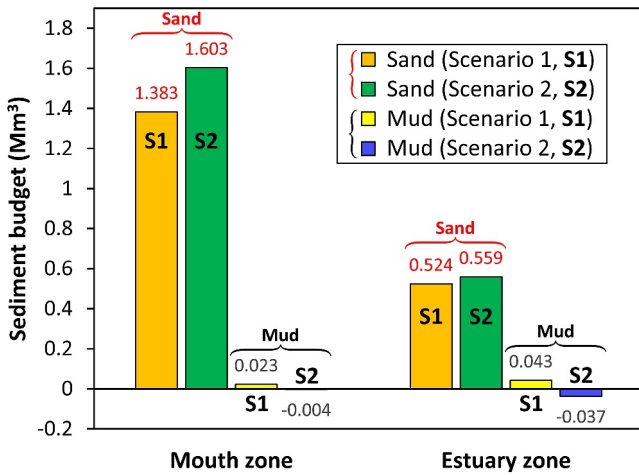


Figure 7. Zonal sand and mud budgets resulting from Scenarios 1 and 2 (baseline and clear-water release scenarios). Compared to Scenario 1, Scenario 2 had greater sand budgets yet negative mud budgets. For Scenario 2, the increase of total sediment budget in mouth zone was attributed to the larger surplus of sand budget over the deficit of mud budget, yet the reduction of total budget in estuary zone was attributed to the larger deficit of mud budget over the surplus of sand budget.

Scenario 2, the smaller sand budgets of Scenario 1 are thus attributable to the mantling effect of the reservoir-released muds on sand transports, as reported by a number of researchers. For example, field observations from the Mekong Delta revealed that mobilization of bottom sands and suspended and bedload sand transports were restricted by estuarine mud mantling (Allison, Dallon Weathers, & Meselhe, 2017; Stephens et al., 2017). Field studies of the Scheldt estuary showed that up to 40% of the intertidal area was mantled by muds, limiting the transport of sands that made up 95% of the estuary sediment volume (Braat et al., 2023). A numerical study applying the Delft3D model on an idealized estuary revealed that as the mud supply increased, larger proportions of the bed were mantled by muds whose contents would rise to a mud-dominated regime, as a result sands became even less erodible (Braat et al., 2017).

To quantify the effect of mud mantling, we present in Figure 9 the scenario-wise results during typhoons at three selected cross-sections. Figures 9a–9c are flow velocities (with positive and negative values indicating seaward and landward), where peak and post-peak periods of Sinlaku and Jangmi were identified based on the rise/fall of velocities. Figures 9d–9f are the simulated mud SSC compared to the SSC observed at the bottom outlet. As shown, the reservoir-released mud SSC remained high even after the flood peaks, which sustained the rise of the simulated mud SSC during the post-peak periods, particularly evidential at Taipei and Guandu Bridges. The decreasing velocity

and increasing mud SSC during the post-peak periods led to deposition of muds and increase of bed mud contents (Figures 9g–9i). Without mud releases (Scenario 2), the rise of bed mud contents during the post-peak periods would not occur (see black lines).

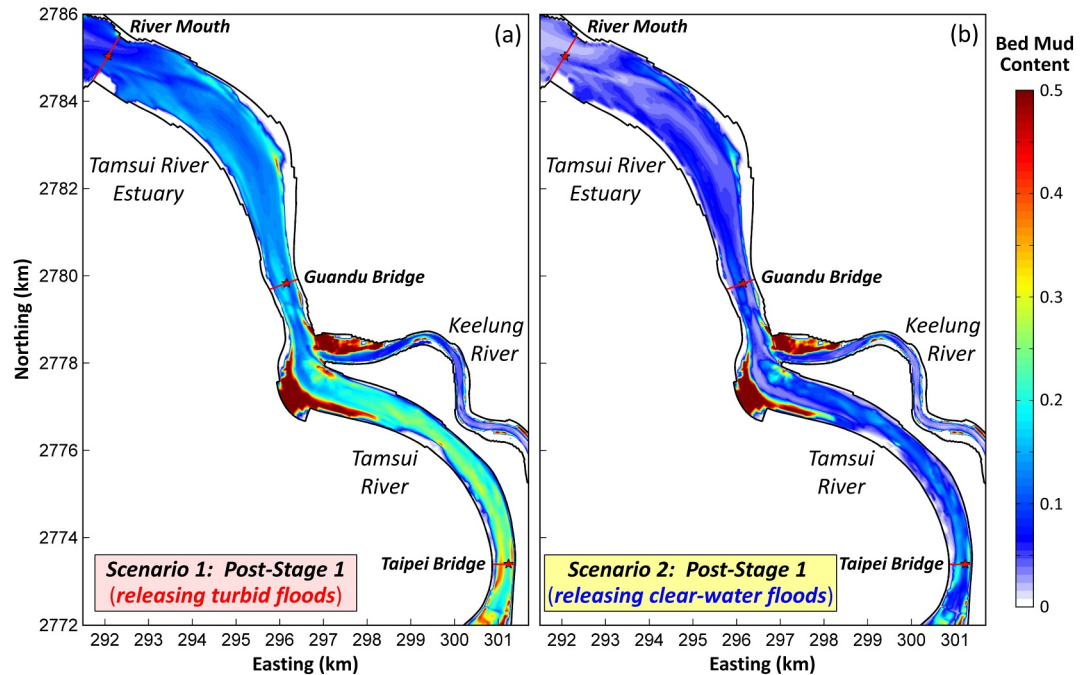


Figure 8. Post-Stage 1 bed mud contents resulting from (a) Scenario 1 (baseline mud-release scenario), and (b) Scenario 2 (hypothetical clear-water release scenario). Throughout the estuary system, bed mud contents of Scenario 2 are consistently lower. Shown here are the mainstem Tamsui River and lower Keelung River, and three cross-sections used for analyses (Taipei Bridge, Guandu Bridge, and River Mouth).

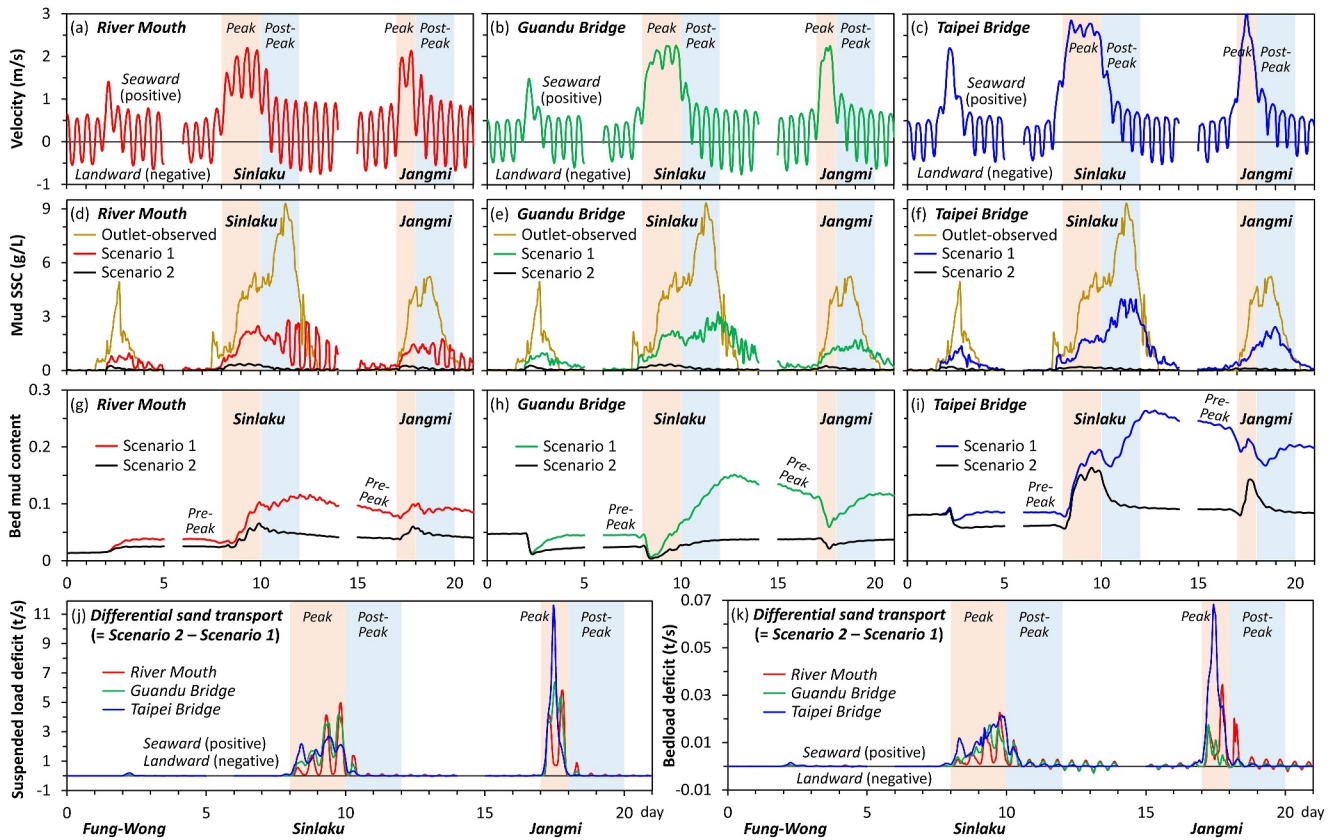


Figure 9. (a–i) Simulation results in typhoon periods at three cross-sections: velocities, scenario-wise mud suspended sediment concentrations and bed mud contents. (j–k) Suspended-load and bedload sand transport deficits (= differential sand transports between Scenarios 1 and 2). Positive and negative values indicate seaward and landward.

Sand transports were greater without mud releases, either seaward or landward. Figures 9j and 9k show the differential sand transports between Scenarios 1 and 2, which represent the sand transport deficits caused by mud mantling. The differential sand transports were dominated by suspended load, being two orders of magnitude greater than bedload. During peak periods there were only seaward (positive) differential transports, while during non-peak periods there were seaward and landward cycles of small differential transports. Shown in Table 3 are the cumulative sand transports during typhoon periods at three cross-sections. On average, suspended load accounted for 97% of the total load (for either Scenario), the suspended load deficit accounted for >99% of the

Table 3

Cumulative Sand Transports (Suspended Load, Bedload, and Total Load) at Three Cross-Sections During Typhoon Periods Resulting From Scenarios 1 and 2 (With and Without Reservoir Mud Releases)

Cross-section	Scenario	Cumulative sand transport (Mt)			Differential sand transport (Mt)		
		Suspended load	Bedload	Total load	Suspended load deficit	Bedload deficit	Total load deficit
River Mouth	Scenario 1	2.442	0.081	2.523	0.411	0.002	0.413
	Scenario 2	2.853	0.084	2.937			
Guandu Bridge	Scenario 1	3.489	0.090	3.579	0.580	0.002	0.583
	Scenario 2	4.070	0.092	4.162			
Taipei Bridge	Scenario 1	2.798	0.084	2.882	0.595	0.005	0.600
	Scenario 2	3.393	0.089	3.482			

Note. Differential sand transports between Scenarios 1 and 2 represent sand transport deficits caused by mud mantling.

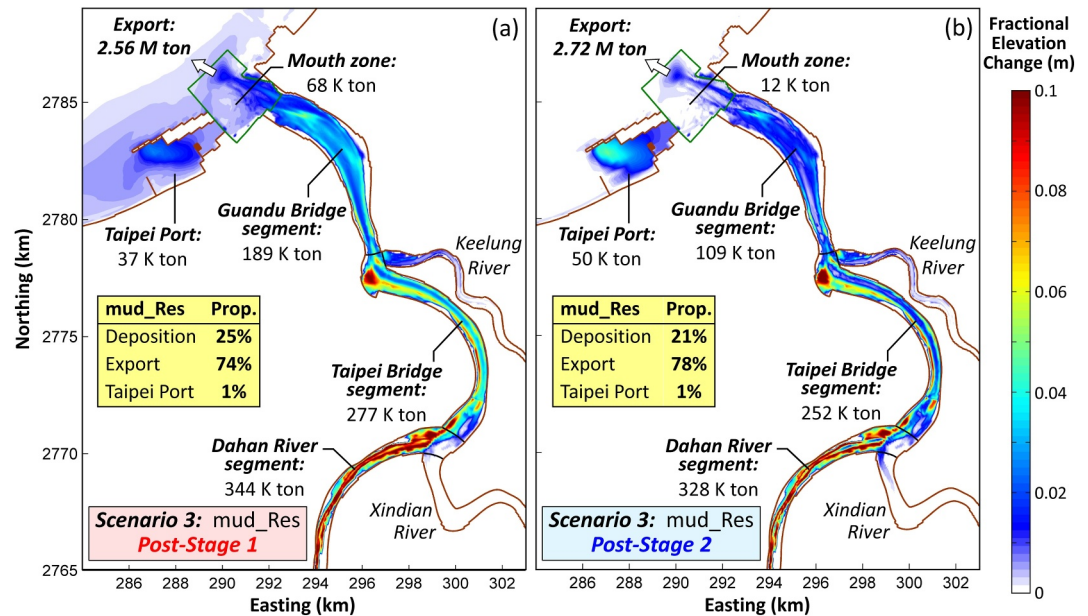


Figure 10. Simulation results of Scenario 3 (tracking released muds): bed elevation changes and budgets of reservoir-released muds (*mud_Res*) in four subareas (Dahan River segment, Taipei Bridge segment, Guandu Bridge segment, and mouth zone) and Taipei Port, after (a) Stage 1, and (b) Stage 2. Summarized in the inset tables are the proportions of *mud_Res* deposited in four subareas, exported to offshore and transported to the Taipei Port.

total load deficit. Overall, with reservoir-released muds and the consequential effect of mud mantling, the mean sand transport during typhoons was 15% less than that without reservoir-released muds.

Here is the answer to the first research question posed. Reservoir mud releasing did bear impacts on estuarine and coastal sediment budgets. The effects of the reservoir-released muds were indirect, not through direct contributions to the sediment budgets or morphological changes, yet by deposition of muds along the way and mantling the bed to restrict sand delivery, thus reducing the sand budgets. To what degree were the estuarine and coastal sand budgets impacted by the reservoir-released muds then depends on the fate of these muds, as further elucidated below.

3.3. Scenario 3: Tracking Reservoir-Released Mud

To track the spatiotemporal distributions of the reservoir-released muds, the mainstem Tamsui River study area was split into four subareas (Figure 10), that is, Dahan River segment, Taipei Bridge segment, Guandu Bridge segment, and mouth zone. The coarse and fine fractions of the reservoir-released muds are denoted as *mud_Res_c* and *mud_Res_f*, and their sum is denoted as *mud_Res*.

Distributions of *mud_Res* after Stages 1 and 2 are shown in Figures 10a and 10b, where the fractional bed elevation changes and zonal budgets are presented. During Stage 1, a total of 3.48 M ton of muds were released from the reservoir, 74% of which was exported to offshore, 25% was deposited in the study area, and 1% was transported to the Taipei Port (see Figure 10a and inset table). Mud deposits declined seaward, from 344 K ton in the Dahan River segment to 68 K ton in the mouth zone. As noted earlier, the reservoir-released muds consisted of 40% coarse muds and 60% fine muds, 57% of the coarse muds were deposited while 95% of the fine muds were exported to offshore (see Figures S15a and S15b in Supporting Information S1 and inset tables). During Stage 2, those muds deposited during Stage 1 were resuspended and transported by asymmetric tidal currents, resulting in seaward residual transports (Figures S15c and S15d in Supporting Information S1). After Stage 2, the *mud_Res* deposits decreased by 4% while the *mud_Res* exports increased by 4% (see Figure 10b and inset table). This tidal flushing took place primarily in the main channels.

Figure 11 shows the time series zonal budgets of *mud_Res* during Stages 1 and 2. Three results deserve mention here. First, the budgets of coarse and fine muds during Stage 1 are shown in Figures 11a and 11b. The coarse

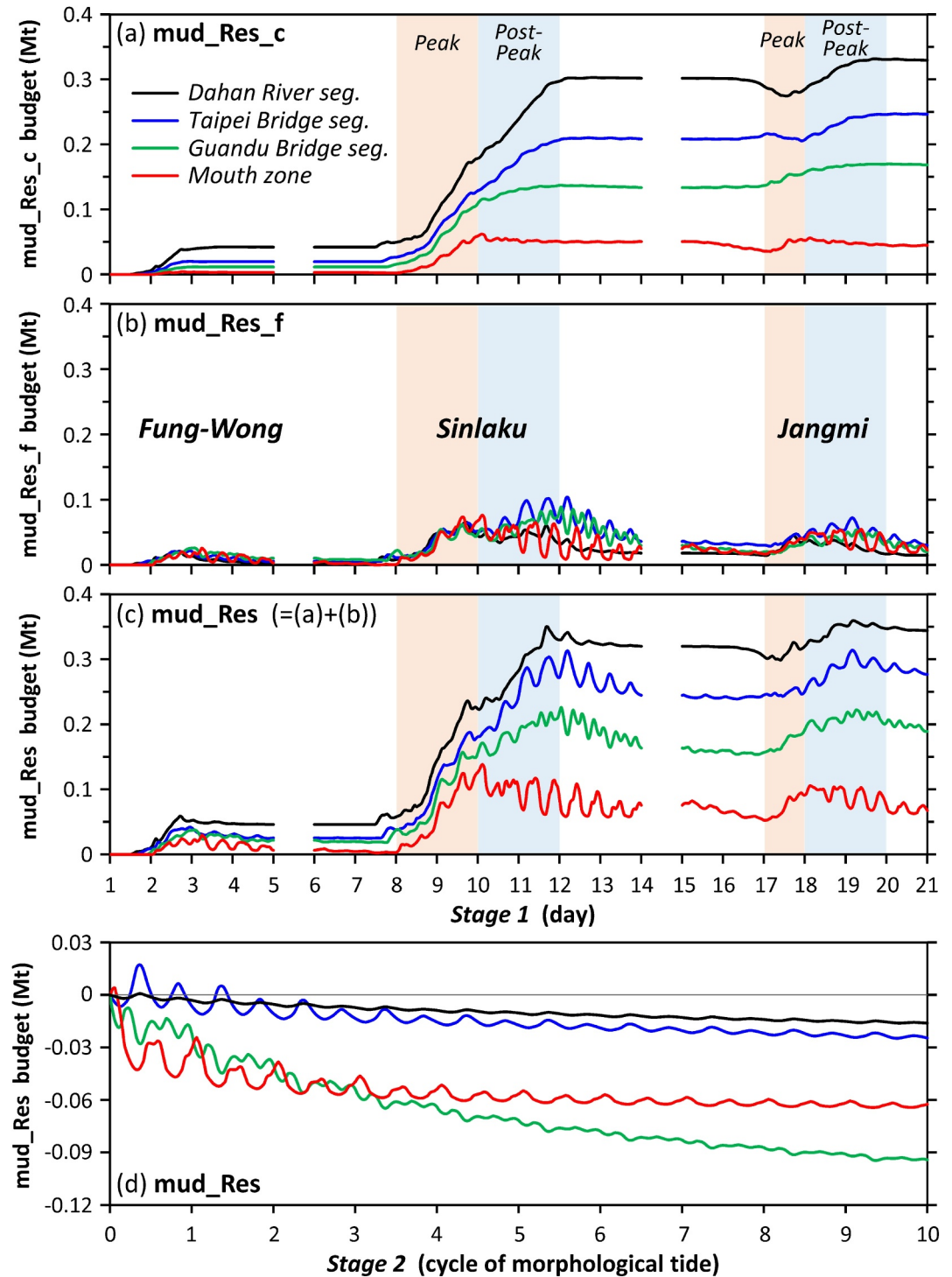


Figure 11. Time series budgets of reservoir-released muds in four subareas (Dahan River segment, Taipei Bridge segment, Guandu Bridge segment, mouth zone) (a–c) during Stage 1, coarse and fine mud fractions (mud_Res_c and mud_Res_f) and total muds (mud_Res); (d) during Stage 2, mud_Res .

muds, with a greater w_s , were less susceptible to tidal actions, showing increasing trends with cumulative mud releases. Coarse mud deposits also exhibited a strong trend of seaward decreasing. By contrast, fine mud deposits varied more closely with the tidal cycle, exhibiting no apparent spatial trend, and was an order of magnitude smaller than the coarse mud deposits. Second, summing the coarse and fine muds results in Figure 11c, which

exhibits the effects of both cumulative mud deposits and tidal resuspension during Stage 1. Third, the time series of mud_Res budgets during Stage 2 are shown in Figure 11d, where tidal flushing of mud deposits from the estuarine segments is clear. This flushing effect exhibits a landward decreasing trend due to attenuation of tidal wave. After 10 cycles of morphological tide, the mud_Res budget in the wave-affected mouth zone approached a dynamic equilibrium, while the mud_Res budgets in the tide-dominated estuarine segments remained a mild decreasing trend.

We are now able to answer the second research question posed. During typhoon periods, 74% of the reservoir-released muds were exported to offshore, the remaining 25% were deposited along the way. It was these mud deposits that covered the bed, reduced the sand availability, and caused a 15% reduction in sand transports compared to a hypothetical scenario of releasing clear-water floods. The major ingredient of the mud covers was mud_Res_c, accounting for >90% of the mud_Res deposits. The amount of mud_Res exported to offshore constituted 62% of the total export, the latter included preexisting sands and muds.

4. Discussion

4.1. Broad Implications

Our results revealed that the synchronized release of mud and flood pulse from the reservoir can be an efficient measure to mitigate reservoir siltation yet may be a suboptimal solution to addressing coastal sediment deficit. For the case studied here, during three typhoons in 2008 a total of 11.8 Mm³ muds were released, removing equivalently >10% of the siltation volume. A majority part (74%) of the reservoir-released muds were transported through the estuary and river mouth, and exported to offshore. The remaining part (25%) of the reservoir-released muds were deposited along the way, increasing the bed mud contents by 5%–12% compared to a hypothetical scenario of clear-water flood releases. On average, mud mantling caused a 15% deficit in fluvial sand transports, thus reducing the sand budget of river mouth by 14%. The decrease of sand budget suboptimized the efforts to address coastal sediment deficits, given that these flood-driven, tributary-sourced sands play a pivotal role in delta nourishment, contributing >98% of the sediment budget in river mouth.

From the perspective of reservoir trapping, consider a hypothetical pre-damming scenario, assuming that everything else remains as the present. As mentioned in Section 3.1.3, Xindian River dominated tributary sand supplies, which were mainly sourced from hillslope and channel erosion. Sand supplies from upstream of the Shihmen Reservoir rarely exceeded 5% of the sediment inflows (NRWRO, 2021), thus the amount of sand trapped by the reservoir may be neglected. Without a dam the turbidity current inflows during typhoons would be fully delivered to downstream. This would increase mud deliveries by at least a factor of 3, as the sediment sluicing ratio of Shihmen Reservoir is at maximum 30% (Section 2.1). With more mud deliveries and deposits, the effect of mud mantling would be stronger, reducing even more fluvial sand transports and coastal sand budgets. Thus, if the mud-release scenario is compared to the pre-damming scenario, one could argue that the presence of a dam may bear some merits over demerits. This advantage, however, comes at the cost of trapping at least 70% of sediment inflows, just like the hypothetical optimal scenario of clear-water releases that trapped 100% of sediment inflows. Based on the speculation from the pre-damming scenario, we can conclude that reservoir desiltation and delta nourishment are, among others, competing objectives to be compromised in the framework of multi-objective optimization. The clear-water release scenario (trapping 100% of sediment inflows) and pre-damming scenario (trapping 0% of sediment inflows) are two extreme cases of this framework. For reservoirs with considerable upstream sand supplies, however, dams could interrupt the natural transport of sands, which would be then made even worse by mud mantling. Our findings thus highlight that sustainable sediment management needs to look beyond just a bulk amount of sediment, but for achieving the desired morphologic goals it is critical to consider how different sediment fractions interact and how they are impacted by human activities.

At the global scale, among the world's 56 cases of reservoir sediment release shown in Figure 2, there are 34% (19/56) experiencing coastal erosions at the downstream ends (Table S1 in Supporting Information S1). This number is consistent with those reported by other researchers. For example, Luijendijk et al. (2018), based on analyses of the satellite derived shorelines, estimated that 24% of the world's sandy coasts are being persistently eroded due in part to the diminishing sand supplies; Besset et al. (2019), based on data collected from literature and satellite images for the world's 54 major deltas, found that over a 30-year period (1985–2015), 54% (29/54) of them were in net erosion. Further, Table S1 in Supporting Information S1 reveals that among the 19 cases with coastal erosion, 84% (16/19) had muds as the major type of sediment released, of which 63% (10/16) had reservoir

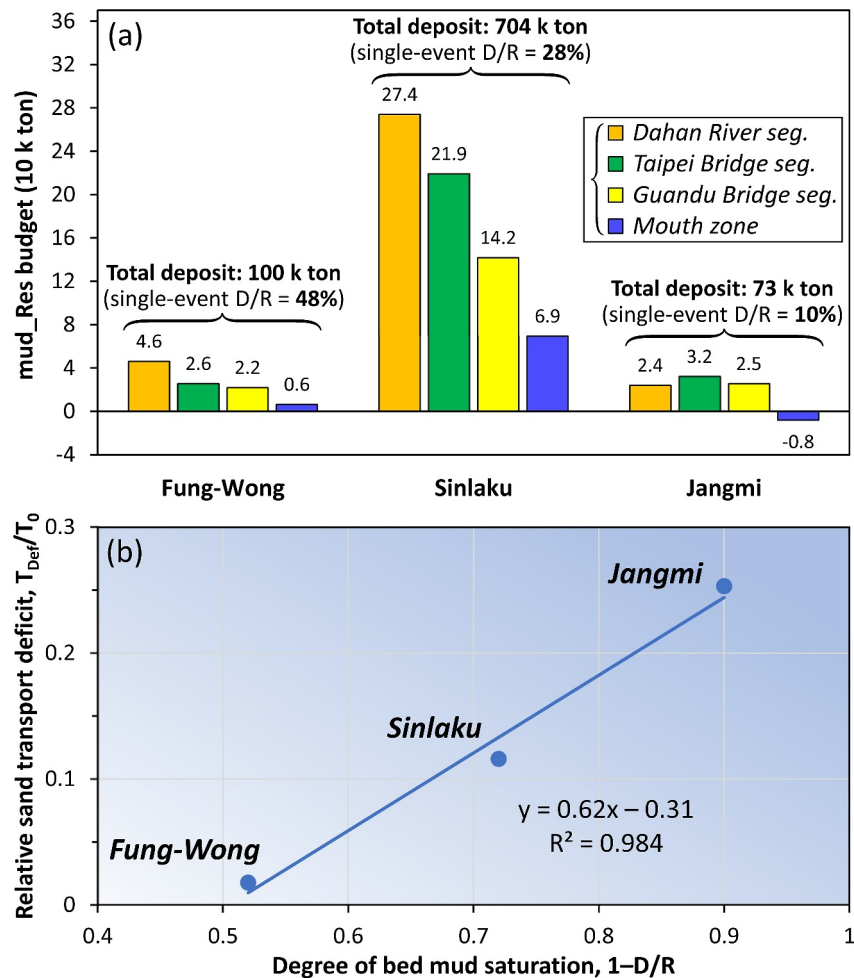


Figure 12. (a) Event-wise zonal budgets of reservoir-released muds (mud_Res) in four subareas. Event-wise total mud deposits, and ratios of single-event mud deposit to mud release (D/R) are also shown. (b) Relation between relative sand transport deficit (T_{Def}/T_0) and degree of bed mud saturation ($1-D/R$), in which T_{Def} is single-event sand transport deficit (sum of suspended-load and bedload deficits shown in Figures 9j–9k), and T_0 is single-event sand transport of Scenario 2 (hypothetical clear-water release scenario).

capacities on the order of 10^6 m^3 , close to the overall percentage, 75% (42/56), of reservoirs belonging to that class. Given these resemblances, our study case should bear sufficient generality to offer useful implications for global reservoirs facing similar problems of siltation and coastal sediment deficit.

4.2. Potential Application

In an attempt to develop optimal strategies for reservoir mud releasing, it may be useful to learn from the evolutions of mud deposit and sand transport with the proceed of mud release events. Figure 12a shows the event-wise zonal budgets of mud_Res , which exhibit a seaward decreasing trend. The event-wise mud releases were 210, 2,538, and 735 k ton, or expressed as the proportions to their sum, 6%: 73%: 21%. The event-wise mud deposits were 100, 704, and 73 k ton, or 11%: 80%: 8%. The ratios of the latter to the former are 1.9:1.1:0.4, implying that for the first event about twice the proportion released was deposited, whereas for the last event less than half the proportion released was deposited. This is echoed by the ratio of single-event mud deposit to release, denoted as D/R (see Figure 12a), which decreased from 48% to 28%–10% with the proceed of mud release events. The decreasing trend of D/R is necessarily a complex function of the operation and state variables, such as the mode of mud release, flow magnitude and duration, mud concentration, composition, and settling velocity, flow velocity, bed shear stress, and most notably the preexisting bed mud content. As shown in Figures 9g–9i, when the bed mud contents were <0.1 in the pre-peak period of Sinlaku, bed mud contents remained fixed even though the

flow velocities increased. By contrast, when the bed mud contents were >0.1 in the pre-peak period of Jangmi, mud contents decreased as the flow velocities increased. Accordingly, for Jangmi, flushing of the already mud-rich bed during the pre-peak and peak periods, and limited mud deposits during the post-peak period, were both responsible for the smallest D/R ratio among the three events.

The single-event deposit to release ratio D/R is an indicator of the intensity of mud deposition, ranging from 0 (for zero deposition on a mud-rich bed) to 1 (for full deposition on a mud-free bed), hence $1-D/R$ may be used to indicate the degree of bed mud saturation. Figure 12b shows the relation between relative sand transport deficit T_{Def}/T_0 and $1-D/R$, where T_{Def}/T_0 is the ratio of single-event sand transport deficit to the corresponding sand transport of the clear-water flood release scenario. The relative sand transport deficit increases linearly with the degree of mud saturation ($R^2 = 0.984$), implying that the relative sand transport deficit could be reduced were the mud release implemented at a smaller value of bed mud content. The trend line also implies that no sand transport deficit would be present when the degree of bed mud saturation is <0.5 .

A potential application of Figure 12b could be made in conjunction with the two-phase flushing strategy, where a clear-water releasing phase is implemented first, followed by a mud releasing phase. The first phase is aimed to lower the bed mud content, so that sand transport deficit during the second phase can be reduced. As the D/R ratio of the second phase is not known in advance, the target degree of bed mud saturation $1-D/R$ in the first phase can be determined for an established target of T_{Def}/T_0 . Once $1-D/R$ (or D/R) is determined, the maximum allowable mud deposit corresponding to the single-event mud release can be evaluated, where the mud release is estimated from the projected mud inflow and the sluicing ratio of the reservoir. The remaining task, hence, is to design a flood release hydrograph that achieves the goal to constrain mud deposits in the allowable range. A similar two-phase strategy has been adopted by the Xiaolangdi Reservoir for flushing the reservoir-trapped mud deposits (Wang et al., 2017; X. Wu et al., 2020). How to optimize the two-phase strategy in order to minimize mud trapped in the reservoir and mud deposited in the downstream channel, and maximize sand supply to coastal sediment budget, applying the approach presented here, is a prospective topic for future studies.

4.3. Future Research

Several factors not considered in the present study warrant incorporation in future research. (a) Density currents, caused by salinity intrusion and SSC stratification during low flows, would confine sediment transport to the near-bottom range and deposition to a shorter distance (Wang et al., 2010; G. Wu et al., 2023). Salinity intrusion also induces baroclinic flows promoting sediment import to the estuary, as well as flocculation leading to greater settling velocity and mud deposits (Olabarrieta et al., 2018; Zhou et al., 2020). Estuarine baroclinic circulation would further trap suspended sediment in the topographic low, leading to a local turbidity maximum present during low flows. To resolve the density stratification effects would require the model to be run in 3D mode. (b) Sand-mud interaction, which affects sand erosion flux through the variations of erodibility (critical shear stress for erosion) and bed roughness (bed shear stress due to skin drag) as a function of bed mud content (Alonso et al., 2023; Braat et al., 2017). Sand erosion flux would decrease with the increase of bed mud content because of the reduced erodibility and bed shear stress, not just because of the reduced availability. (c) Decline of sand supply due to armoring, or supply-limited condition, in channels downstream of the dam (Wang et al., 2017; X. Wu et al., 2020) was not considered in our event-scale morphodynamic study. This factor would potentially reduce coastal sand budget, thus may be taken into account to assess the evolving sediment budget due to *subdecadal*- to *decadal-scale* regular flood releases. (d) Despite that the effect of storm surge (the rise of sea water level above the astronomical tide level due to typhoon-related strong wind, low atmospheric pressure, and wave setup) was incorporated in our large-domain estuary model, the large-scale storm surge effect (with the large-domain estuary model covering the full path of a typhoon) was not considered. This large-scale storm surge effect has the potential to further increase the landward sediment flux (Zhang et al., 2004; Zhu & Wiberg, 2022). To include this large-scale effect would require the large-domain estuary model to be expanded to cover, at least, the entire Taiwan Strait.

5. Conclusions

We show that the event-based mud releasing can be effective in mitigating reservoir siltation yet may be a suboptimal strategy for alleviating coastal sediment deficit. Despite a vast amount of muds were released from the reservoir during typhoon events, a majority part of these muds were delivered through the estuary

and exported to offshore. Rather, the flood-driven sands, sourced from tributaries downstream of the dam, were the major contributor to coastal sediment budget. However, delivery of these sands was restricted by the remaining part of muds that were deposited along the way, mantling the sand deposits and reducing the sands available for transport. The sand transport deficit, relative to a hypothetical scenario of releasing clear-water floods, increases linearly with the degree of bed mud saturation, a novel finding of this study applicable to the design of optimal release strategy. Although sand supplies from upstream of the reservoir are minimal in our case, for reservoirs with considerable upstream sand supplies, however, the dam could interrupt the natural transport of sands, which is then made even worse by mud mantling. Given broad relevance to global reservoirs that face the problems of siltation and coastal sediment deficit, our results present insightful implications for optimal release strategy aimed to minimize muds trapped in the reservoir and deposited in the downstream channel, and maximize sand supplies to coastal sediment budget. Our findings also highlight that sustainable sediment management needs to look beyond just a bulk amount of sediment, but for accomplishing the desired morphologic objectives it is critical to consider how different sediment fractions interact and how they are impacted by human interventions.

Data Availability Statement

The model input and output files are available at the Zenodo repository (Hsueh & Wu, 2023): <https://doi.org/10.5281/zenodo.8435788>. Delft3D source codes are downloadable from the Deltares model repository (<https://oss.deltares.nl/web/delft3d>). ERA5 reanalysis wind field and atmospheric pressure field are available from the ECMWF (<https://www.ecmwf.int/>). TPXO global tide model is accessible at: <https://www.tpxo.net/global>.

Acknowledgments

Research funding was granted by the National Science and Technology Council (NSTC) Taiwan to FC Wu (107-2221-E-002-029-MY3, 109-2221-E-002-012-MY3, 112-2221-E-002-073-MY3). Data used in this study were supported by the Harbor and Marine Technology Center (IOT, MOTC), Tenth River Management Office, Northern Region Water Resources Office, and Water Resources Planning Institute (WRA, MOEA), and Taiwan Ocean Data Bank (NSTC). We appreciate Rafael J. P. Schmitt and two anonymous reviewers for constructive feedback that helped improve this paper substantially.

References

- Akter, J., Roelvink, D., & van der Wegen, M. (2021). Process-based modeling deriving a long-term sediment budget for the Ganges-Brahmaputra-Meghna Delta, Bangladesh. *Estuarine, Coastal and Shelf Science*, 260, 107509. <https://doi.org/10.1016/j.ecss.2021.107509>
- Allison, M. A., Dallon Weathers, H., & Meselhe, E. A. (2017). Bottom morphology in the Song Hau distributary channel, Mekong River delta, Vietnam. *Continental Shelf Research*, 147, 51–61. <https://doi.org/10.1016/j.csr.2017.05.010>
- Allison, M. A., & Meselhe, E. A. (2010). The use of large water and sediment diversions in the lower Mississippi River (Louisiana) for coastal restoration. *Journal of Hydrology*, 387(3–4), 346–360. <https://doi.org/10.1016/j.jhydrol.2010.04.001>
- Allison, M. A., Nittrouer, C., Ogston, A., Mullarney, J., & Nguyen, T. (2017). Sedimentation and survival of the Mekong Delta: A case study of decreased sediment supply and accelerating rates of relative sea level rise. *Oceanography*, 30(3), 98–109. <https://doi.org/10.5670/oceanog.2017.318>
- Alonso, C., van Maren, D. S., van Weerdenburg, R. J. A., Huisman, Y., & Wang, Z. B. (2023). Morphodynamic modeling of tidal basins: The role of sand-mud interaction. *Journal of Geophysical Research: Earth Surface*, 128(9), e2023JF007391. <https://doi.org/10.1029/2023JF007391>
- Asaeda, T., & Rashid, M. H. (2012). The impacts of sediment released from dams on downstream sediment bar vegetation. *Journal of Hydrology*, 430–431, 25–38. <https://doi.org/10.1016/j.jhydrol.2012.01.040>
- Barrera Crespo, P. D., Mosselman, E., Giardino, A., Becker, A., Ottevanger, W., Nabi, M., & Arias-Hidalgo, M. (2019). Sediment budget analysis of the Guayas River using a process-based model. *Hydrology and Earth System Sciences*, 23(6), 2763–2778. <https://doi.org/10.5194/hess-23-2763-2019>
- Benedet, L., Dobrochinski, J., Walstra, D., Klein, A., & Ranasinghe, R. (2016). A morphological modeling study to compare different methods of wave climate schematization and evaluate strategies to reduce erosion losses from a beach nourishment project. *Coastal Engineering*, 112, 69–86. <https://doi.org/10.1016/j.coastaleng.2016.02.005>
- Besset, M., Anthony, E. J., & Bouchette, F. (2019). Multi-decadal variations in delta shorelines and their relationship to river sediment supply: An assessment and review. *Earth-Science Reviews*, 193, 199–219. <https://doi.org/10.1016/j.earscirev.2019.04.018>
- Besset, M., Anthony, E. J., & Sabatier, F. (2017). River delta shoreline reworking and erosion in the Mediterranean and Black Seas: The potential roles of fluvial sediment starvation and other factors. *Elementa: Science of the Anthropocene*, 5, 54. <https://doi.org/10.1525/elementa.139>
- Blum, M. D., & Roberts, H. H. (2009). Drowning of the Mississippi Delta due to insufficient sediment supply and global sea-level rise. *Nature Geoscience*, 2(7), 488–491. <https://doi.org/10.1038/ngeo553>
- Boateng, I., Bray, M., & Hooke, J. (2012). Estimating the fluvial sediment input to the coastal sediment budget: A case study of Ghana. *Geomorphology*, 138(1), 100–110. <https://doi.org/10.1016/j.geomorph.2011.08.028>
- Braat, L., Pierik, H. J., van Dijk, W. M., van de Lageweg, W. I., Brückner, M. Z. M., van der Meulen, B., & Kleinhans, M. G. (2023). Observed and modelled tidal bar sedimentology reveals preservation bias against mud in estuarine stratigraphy. *The Depositional Record*, 9(2), 380–402. <https://doi.org/10.1002/dep2.190>
- Braat, L., van Kessel, T., Leuven, J. R. F. W., & Kleinhans, M. G. (2017). Effects of mud supply on large-scale estuary morphology and development over centuries to millennia. *Earth Surface Dynamics*, 5(4), 617–652. <https://doi.org/10.5194/esurf-5-617-2017>
- Brandt, S. A., & Swenning, J. (1999). Sedimentological and geomorphological effects of reservoir flushing: The Cachí Reservoir, Costa Rica, 1996. *Geografiska Annaler - Series A: Physical Geography*, 81(3), 391–407. <https://doi.org/10.1111/1468-0459.00069>
- Chamoun, S., De Cesare, G., & Schleiss, A. J. (2016). Managing reservoir sedimentation by venting turbidity currents: A review. *International Journal of Sediment Research*, 31(3), 195–204. <https://doi.org/10.1016/j.ijsrc.2016.06.001>
- Chen, C.-N., & Tsai, C.-H. (2017). Estimating sediment flushing efficiency of a shaft spillway pipe and bed evolution in a reservoir. *Water*, 9(12), 924. <https://doi.org/10.3390/w9120924>
- Chen, W.-B., Liu, W. C., Hsu, M. H., & Hwang, C. C. (2015). Modeling investigation of suspended sediment transport in a tidal estuary using a three-dimensional model. *Applied Mathematical Modelling*, 39(9), 2570–2586. <https://doi.org/10.1016/j.apm.2014.11.006>

- Cox, J. R., Huismans, Y., Knaake, S. M., Leuven, J. R. F. W., Vellinga, N. E., van der Vegt, M., et al. (2021). Anthropogenic effects on the contemporary sediment budget of the lower Rhine-Meuse Delta channel network. *Earth's Future*, 9(7), e2020EF001869. <https://doi.org/10.1029/2020ef001869>
- Darby, S. E., Appeaning Addo, K., Hazra, S., Rahman, M. M., & Nicholls, R. (2020). Fluvial sediment supply and relative sea-level rise. In R. J. Nicholls (Ed.), *Deltas in the Anthropocene* (pp. 103–126). Palgrave Macmillan.
- Deltares. (2014a). *Delft3D-FLOW, user manual. Version 3.15*. Delft.
- Deltares. (2014b). *Delft3D-WAVE, user manual. Version 3.05*. Delft.
- Dethier, E. N., Renshaw, C. E., & Magilligan, F. J. (2022). Rapid changes to global river suspended sediment flux by humans. *Science*, 376(6600), 1447–1452. <https://doi.org/10.1126/science.abn7980>
- Dissanayake, D. M. P. K., Wurpts, A., Miani, M., Knaack, H., Niemeyer, H., & Roelvink, J. (2012). Modelling morphodynamic response of a tidal basin to an anthropogenic effect: Ley Bay, East Frisian Wadden Sea – Applying tidal forcing only and different sediment fractions. *Coastal Engineering*, 67, 14–28. <https://doi.org/10.1016/j.coastaleng.2012.04.001>
- Dunn, F. E., Darby, S. E., Nicholls, R. J., Cohen, S., Zarfl, C., & Fekete, B. M. (2019). Projections of declining fluvial sediment delivery to major deltas worldwide in response to climate change and anthropogenic stress. *Environmental Research Letters*, 14(8), 084034. <https://doi.org/10.1088/1748-9326/ab304e>
- Egbert, G. D., & Erofeeva, S. Y. (2002). Efficient inverse modeling of barotropic ocean tides. *Journal of Atmospheric and Oceanic Technology*, 19(2), 183–204. [https://doi.org/10.1175/1520-0426\(2002\)019<0183:eimobo>2.0.co;2](https://doi.org/10.1175/1520-0426(2002)019<0183:eimobo>2.0.co;2)
- Espa, P., Batalla, R. J., Brignoli, M. L., Crosa, G., Gentili, G., & Quadroni, S. (2019). Tackling reservoir siltation by controlled sediment flushing: Impact on downstream fauna and related management issues. *PLoS One*, 14(6), e0218822. <https://doi.org/10.1371/journal.pone.0218822>
- Fredsoe, J. (1984). Turbulent boundary layer in wave-current motion. *Journal of Hydraulic Engineering*, 110(8), 1103–1120. [https://doi.org/10.1061/\(asce\)0733-9429\(1984\)110:8\(1103\)](https://doi.org/10.1061/(asce)0733-9429(1984)110:8(1103))
- Fruchard, F., & Camenen, B. (2012). Reservoir sedimentation: Different type of flushing—Friendly flushing example of genissiat dam flushing. In *Proceedings of the International Symposium on Dams for a Changing World*. ICOLD.
- Geleynse, N., Storms, J. E. A., Stive, M. J. F., Jagers, H. R. A., & Walstra, D. J. R. (2010). Modeling of a mixed-load fluvio-deltaic system. *Geophysical Research Letters*, 37(5), L05402. <https://doi.org/10.1029/2009GL042000>
- Gelfenbaum, G., Stevens, A. W., Miller, I., Warrick, J. A., Ogston, A. S., & Eidam, E. (2015). Large-scale dam removal on the Elwha River, Washington, USA: Coastal geomorphic change. *Geomorphology*, 246, 649–668. <https://doi.org/10.1016/j.geomorph.2015.01.002>
- Guo, L., van der Wegen, M., Roelvink, J. A., & He, Q. (2014). The role of river flow and tidal asymmetry on 1-D estuarine morphodynamics. *Journal of Geophysical Research: Earth Surface*, 119(11), 2315–2334. <https://doi.org/10.1002/2014jf003110>
- Hayes, M. O. (1979). Barrier island morphology as a function of wave and tide regime. In S. Leatherman (Ed.), *Barrier Islands from the Gulf of St. Lawrence to the Gulf of Mexico* (pp. 1–29). Academic Press.
- Hibma, A., de Vriend, H., & Stive, M. (2003). Numerical modelling of shoal pattern formation in well-mixed elongated estuaries. *Estuarine, Coastal and Shelf Science*, 57(5–6), 981–991. [https://doi.org/10.1016/s0272-7714\(03\)00004-0](https://doi.org/10.1016/s0272-7714(03)00004-0)
- Hong, E., Ou, C. H., Tseng, S. S., Kuo, N. J., Huang, T. C., & Lee, W. C. (2000). The future impact of the Tanshui Harbor on its nearby coastal environment. *Journal of the Geological Society of China*, 43, 341–360.
- Hopkins, J., Elgar, S., & Raubenheimer, B. (2018). Storm impact on morphological evolution of a sandy inlet. *Journal of Geophysical Research: Oceans*, 123(8), 5751–5762. <https://doi.org/10.1029/2017JC013708>
- Hsieh, T.-C., Ding, Y., Yeh, K. C., & Jhong, R. K. (2020). Investigation of morphological changes in the Tamsui River estuary using an integrated coastal and estuarine processes model. *Water*, 12(4), 1084. <https://doi.org/10.3390/w12041084>
- Hsu, M.-H., Wu, C. R., Liu, W. C., & Kuo, A. Y. (2006). Investigation of turbidity maximum in a mesotidal estuary, Taiwan. *Journal of the American Water Resources Association*, 42(4), 901–914. <https://doi.org/10.1111/j.1752-1688.2006.tb04503.x>
- Hsu, S. T., & Wu, C.-H. (2019). The conversion of Shihmen Reservoir's #2 penstock into a silt-sludge way. In *Proceedings of the 3rd International Workshop on Sediment Bypass Tunnels*. NTU.
- Hsueh, Y.-T., & Wu, F.-C. (2023). Dataset accompanying the publication: Reservoir mud releasing may suboptimize fluvial sand supply to coastal sediment budget: Modeling the impact of Shihmen Reservoir case on Tamsui River estuary [Dataset]. *Zenodo*. <https://doi.org/10.5281/zenodo.8435788>
- Hu, K., Ding, P., Wang, Z., & Yang, S. (2009). A 2D/3D hydrodynamic and sediment transport model for the Yangtze Estuary, China. *Journal of Marine Systems*, 77(1–2), 114–136. <https://doi.org/10.1016/j.jmarsys.2008.11.014>
- Kemp, G. P., Day, J. W., Rogers, J. D., Giosan, L., & Peyronnin, N. (2016). Enhancing mud supply from the Lower Missouri River to the Mississippi River Delta USA: Dam bypassing and coastal restoration. *Estuarine, Coastal and Shelf Science*, 183, 304–313. <https://doi.org/10.1016/j.ecss.2016.07.008>
- Kondolf, G. M., Gao, Y., Annandale, G. W., Morris, G. L., Jiang, E., Zhang, J., et al. (2014). Sustainable sediment management in reservoirs and regulated rivers: Experiences from five continents. *Earth's Future*, 2(5), 256–280. <https://doi.org/10.1002/2013ef000184>
- Kondolf, G. M., Schmitt, R. J., Carling, P., Darby, S., Arias, M., Bizzi, S., et al. (2018). Changing sediment budget of the Mekong: Cumulative threats and management strategies for a large river basin. *Science of the Total Environment*, 625, 114–134. <https://doi.org/10.1016/j.scitotenv.2017.11.361>
- Kondolf, G. M., & Yi, J. (2022). Dam renovation to prolong reservoir life and mitigate dam impacts. *Water*, 14(9), 1464. <https://doi.org/10.3390/w14091464>
- Lai, S. Y. J., & Wu, F.-C. (2021). Two-stage transition from Gilbert to hyperpycnal delta in reservoir. *Geophysical Research Letters*, 48(14), e2021GL093661. <https://doi.org/10.1029/2021GL093661>
- Lee, F.-Z., Lai, J. S., & Sumi, T. (2022). Reservoir sediment management and downstream river impacts for sustainable water resources—Case study of Shihmen Reservoir. *Water*, 14(3), 479. <https://doi.org/10.3390/w14030479>
- Lesser, G. R. (2009). *An approach to medium-term coastal morphological modelling* (PhD thesis). Delft University of Technology and UNESCO-IHE.
- Lesser, G. R., Roelvink, J., van Kester, J., & Stelling, G. (2004). Development and validation of a three-dimensional morphological model. *Coastal Engineering*, 51(8–9), 883–915. <https://doi.org/10.1016/j.coastaleng.2004.07.014>
- Lin, P.-C., Chou, H.-T., Capart, H., Lin, W.-J., & Ho, L.-S. (2007). *Sediment transport at Danshui River Mouth and surrounding coastlines*. Report 96-58-7272. Harbor and Marine Technology Center, Institute of Transportation.
- Lin, P.-C., Wei, C.-H., & Ho, L.-S. (2017). *2016 field investigation of sediment transport in the shore vicinity of harbors*. Report 106-036-7936. Harbor and Marine Technology Center, Institute of Transportation.
- Liu, W.-C., Chen, W. B., Cheng, R. T., Hsu, M. H., & Kuo, A. Y. (2007). Modeling the influence of river discharge on salt intrusion and residual circulation in Danshuei River estuary, Taiwan. *Continental Shelf Research*, 27(7), 900–921. <https://doi.org/10.1016/j.csr.2006.12.005>

- Liu, W.-C., Liu, H. M., & Huang, W. C. (2022). Flood-ebb and discharge variations in observed salinity and suspended sediment in a mesotidal estuary. *The Standard*, 2, 209–225. <https://doi.org/10.3390/standards2020016>
- Luan, H. L., Ding, P. X., Wang, Z. B., & Ge, J. Z. (2017). Process-based morphodynamic modeling of the Yangtze Estuary at a decadal timescale: Controls on estuarine evolution and future trends. *Geomorphology*, 290, 347–364. <https://doi.org/10.1016/j.geomorph.2017.04.016>
- Luijendijk, A., Hagenaars, G., Ranasinghe, R., Baart, F., Donchyts, G., & Aarminkhof, S. (2018). The state of the world's beaches. *Scientific Reports*, 8(1), 6641. <https://doi.org/10.1038/s41598-018-24630-6>
- Luijendijk, A. P., Ranasinghe, R., de Schipper, M. A., Huisman, B. A., Swinkels, C. M., Walstra, D. J., & Stive, M. J. (2017). The initial morphological response of the sand engine: A process-based modelling study. *Coastal Engineering*, 119, 1–14. <https://doi.org/10.1016/j.coastaleng.2016.09.005>
- Merwade, V. M., Maidment, D. R., & Goff, J. A. (2006). Anisotropic considerations while interpolating river channel bathymetry. *Journal of Hydrology*, 331(3–4), 731–741. <https://doi.org/10.1016/j.jhydrol.2006.06.018>
- Meselhe, E. A., Sadid, K. M., & Allison, M. A. (2016). Riverside morphological response to pulsed sediment diversions. *Geomorphology*, 270, 184–202. <https://doi.org/10.1016/j.geomorph.2016.07.023>
- Morris, G. L. (2020a). Classification of management alternatives to combat reservoir sedimentation. *Water*, 12(3), 861. <https://doi.org/10.3390/w12030861>
- Morris, G. L., & Fan, J. (1998). *Reservoir sedimentation handbook*. McGraw-Hill.
- Nardin, W., Lera, S., & Nienhuis, J. (2020). Effect of offshore waves and vegetation on the sediment budget in the Virginia Coast Reserve (VA). *Earth Surface Processes and Landforms*, 45(12), 3055–3068. <https://doi.org/10.1002/esp.4951>
- Nittrouer, J. A., & Viparelli, E. (2014). Sand as a stable and sustainable resource for nourishing the Mississippi River delta. *Nature Geoscience*, 7(5), 350–354. <https://doi.org/10.1038/ngeo2142>
- NRWRO. (2021). *Sediment transport monitoring facility maintenance and flood event observations in Shihmen Reservoir (1/2)*. Report MOEAWRA1100123. Northern Region Water Resources Office, WRA, MOEA.
- NRWRO. (2022). *Shihmen reservoir website*. Northern Region Water Resources Office, WRA, MOEA. Retrieved from <https://shihmen.wranb.gov.tw/>
- Olabarrieta, M., Geyer, W. R., Coco, G., Friedrichs, C. T., & Cao, Z. (2018). Effects of density-driven flows on the long-term morphodynamic evolution of funnel-shaped estuaries. *Journal of Geophysical Research: Earth Surface*, 123(11), 2901–2924. <https://doi.org/10.1029/2017jf004527>
- Partheniades, E. (1965). Erosion and deposition of cohesive soils. *Journal of the Hydraulics Division*, 91(1), 105–139. <https://doi.org/10.1061/jyceaj.0001165>
- Roelvink, D., & Reniers, A. (2012). *A guide to modeling coastal morphology*. World Scientific.
- Roelvink, D., & Walstra, D.-J. (2004). Keeping it simple by using complex models. In M. S. Altınakar (Ed.), *Advances in Hydro-science and Engineering* (Vol. 6, pp. 335–346). National Center for Computational Hydroscience and Engineering.
- Rovira, A., & Ibáñez, C. (2007). Sediment management options for the lower Ebro River and its delta. *Journal of Soils and Sediments*, 7(5), 285–295. <https://doi.org/10.1065/jss2007.08.244>
- Schleiss, A. J., Franca, M. J., Juez, C., & De Cesare, G. (2016). Reservoir sedimentation. *Journal of Hydraulic Research*, 54(6), 595–614. <https://doi.org/10.1080/00221686.2016.1225320>
- Schmitt, R. J. P., & Minderhoud, P. S. J. (2023). Data, knowledge, and modeling challenges for science-informed management of river deltas. *One Earth*, 6(3), 216–235. <https://doi.org/10.1016/j.oneear.2023.02.010>
- Schmitt, R. J. P., Rubin, Z., & Kondolf, G. (2017). Losing ground - Scenarios of land loss as consequence of shifting sediment budgets in the Mekong Delta. *Geomorphology*, 294, 58–69. <https://doi.org/10.1016/j.geomorph.2017.04.029>
- Soulsby, R. L., Hamm, L., Klopman, G., Myrhaug, D., Simons, R., & Thomas, G. (1993). Wave-current interaction within and outside the bottom boundary layer. *Coastal Engineering*, 21(1–3), 41–69. [https://doi.org/10.1016/0378-3839\(93\)90045-a](https://doi.org/10.1016/0378-3839(93)90045-a)
- Stephens, J. D., Allison, M., Di Leonardo, D., Weathers, H., Ogston, A., McLachlan, R., et al. (2017). Sand dynamics in the Mekong River channel and export to the coastal ocean. *Continental Shelf Research*, 147, 38–50. <https://doi.org/10.1016/j.csr.2017.08.004>
- Su, C.-H., Liaw, C.-T., Huang, M.-H., Luo, G.-S., Wei, C.-H., Lee, J.-D., et al. (2021). *Annual statistic report of oceanographical observation data in Taipei offshore region at 2019*. Institute of Transportation, Ministry of Transportation, and Communications.
- Sumi, T. (2008). Evaluation of efficiency of reservoir sediment flushing in Kurobe River. In T. Sekiguchi (Ed.), *Proceedings 4th International Conference on scour and erosion* (pp. 608–613).
- Syvitski, J. P. M., Vörösmarty, C. J., Kettner, A. J., & Green, P. (2005). Impact of humans on the flux of terrestrial sediment to the global coastal ocean. *Science*, 308(5720), 376–380. <https://doi.org/10.1126/science.1109454>
- Toniolo, H., Parker, G., & Voller, V. (2007). Role of ponded turbidity currents in reservoir trap efficiency. *Journal of Hydraulic Engineering*, 133(6), 579–595. [https://doi.org/10.1061/\(asce\)0733-9429\(2007\)133:6\(579\)](https://doi.org/10.1061/(asce)0733-9429(2007)133:6(579))
- TRMO. (2015). *Impact assessment of sediment transport at Tansui estuary on surrounding coast (2/2)*. Tenth River Management Office, WRA, MOEA.
- Tu, L. X., Thanh, V. Q., Reynolds, J., Van, S. P., Anh, D. T., Dang, T. D., & Roelvink, D. (2019). Sediment transport and morphodynamical modeling on the estuaries and coastal zone of the Vietnamese Mekong Delta. *Continental Shelf Research*, 186, 64–76. <https://doi.org/10.1016/j.csr.2019.07.015>
- Valencia, A. A., Storms, J. E. A., Walstra, D. R., van der Vegt, H., & Jagers, H. R. A. (2023). The impact of clastic syn-sedimentary compaction on fluvial-dominated delta morphodynamics. *The Depositional Record*, 9(2), 233–252. <https://doi.org/10.1002/dep2.219>
- van der Vegt, H., Storms, J., Walstra, D., & Howes, N. (2016). Can bed load transport drive varying depositional behaviour in river delta environments? *Sedimentary Geology*, 345, 19–32. <https://doi.org/10.1016/j.sedgeo.2016.08.009>
- van der Vegt, H., Storms, J. E., Walstra, D. R., Nordahl, K., Howes, N. C., & Martinus, A. W. (2020). Grain size fractionation by process-driven sorting in sandy to muddy deltas. *The Depositional Record*, 6(1), 217–235. <https://doi.org/10.1002/dep2.85>
- van der Wegen, M., Dastgheib, A., Jaffe, B. E., & Roelvink, D. (2011). Bed composition generation for morphodynamic modeling: Case study of San Pablo Bay in California, USA. *Ocean Dynamics*, 61(2–3), 173–186. <https://doi.org/10.1007/s10236-010-0314-2>
- van der Wegen, M., Jaffe, B. E., & Roelvink, J. A. (2011). Process-based, morphodynamic hindcast of decadal deposition patterns in San Pablo Bay, California, 1856–1887. *Journal of Geophysical Research*, 116(F2), F02008. <https://doi.org/10.1029/2009jf001614>
- van der Wegen, M., & Roelvink, J. A. (2008). Long-term morphodynamic evolution of a tidal embayment using a two-dimensional, process-based model. *Journal of Geophysical Research*, 113(C3), C03016. <https://doi.org/10.1029/2006jc003983>
- van der Wegen, M., Wang, Z. B., Savenije, H. H. G., & Roelvink, J. A. (2008). Long-term morphodynamic evolution and energy dissipation in a coastal plain, tidal embayment. *Journal of Geophysical Research*, 113(F3), F03001. <https://doi.org/10.1029/2007jf000898>
- van Rijn, L. C. (1993). *Principles of sediment transport in rivers, estuaries and coastal seas*. Aqua Publications.

van Rijn, L. C., Roelvink, J. A., & Horst, W. T. (2001). *Approximation formulae for sand transport by currents and waves and implementation in DELFT-MOR*. Hydraulic Engineering Report Z3054.20/40. Deltares (WL). Retrieved from <http://resolver.tudelft.nl/uuid:c226bf0a-79d6-4357-80ff-c68c4d5f0416>

Wang, H., Bi, N., Wang, Y., Saito, Y., & Yang, Z. (2010). Tide-modulated hyperpycnal flows off the Huanghe (Yellow River) mouth, China. *Earth Surface Processes and Landforms*, 35(11), 1315–1329. <https://doi.org/10.1002/esp.2032>

Wang, H., Wu, X., Bi, N., Li, S., Yuan, P., Wang, A., et al. (2017). Impacts of the dam-orientated water-sediment regulation scheme on the lower reaches and delta of the Yellow River (Huanghe): A review. *Global and Planetary Change*, 157, 93–113. <https://doi.org/10.1016/j.gloplacha.2017.08.005>

Warrick, J. A., Bountry, J. A., East, A. E., Magirl, C. S., Randle, T. J., Gelfenbaum, G., et al. (2015). Large-scale dam removal on the Elwha River, Washington, USA: Source-to-sink sediment budget and synthesis. *Geomorphology*, 246, 729–750. <https://doi.org/10.1016/j.geomorph.2015.01.010>

Warrick, J. A., Stevens, A. W., Miller, I. M., Harrison, S. R., Ritchie, A. C., & Gelfenbaum, G. (2019). World's largest dam removal reverses coastal erosion. *Scientific Reports*, 9(1), 13968. <https://doi.org/10.1038/s41598-019-50387-7>

Willmott, C. J. (1981). On the validation of models. *Physical Geography*, 2, 184–194. <https://doi.org/10.1080/02723646.1981.10642213>

WRPI. (2008). *Observation and measurement of sediment transport and application/development of density current simulation model in Shihmen Reservoir (1/2)*. Report 096D27125050000. Water Resources Planning Institute.

Wu, G., Wang, K., Liang, B., Wu, X., Wang, H., Li, H., & Shi, B. (2023). Modeling the morphological responses of the Yellow River Delta to the water-sediment regulation scheme: The role of impulsive river floods and density-driven flows. *Water Resources Research*, 59(7), e2022WR033003. <https://doi.org/10.1029/2022WR033003>

Wu, X., Bi, N., Syvitski, J., Saito, Y., Xu, J., Nittrouer, J. A., et al. (2020). Can reservoir regulation along the Yellow River be a sustainable way to save a sinking delta? *Earth's Future*, 8(11), e2020EF001587. <https://doi.org/10.1029/2020ef001587>

Wu, X., Wang, H., Bi, N., Xu, J., Nittrouer, J. A., Yang, Z., et al. (2021). Impact of artificial floods on the quantity and grain size of river-borne sediment: A case study of a dam regulation scheme in the yellow river catchment. *Water Resources Research*, 57(5), e2021WR029581. <https://doi.org/10.1029/2021WR029581>

Yang, S. L., Milliman, J., Xu, K., Deng, B., Zhang, X., & Luo, X. (2014). Downstream sedimentary and geomorphic impacts of the Three Gorges Dam on the Yangtze River. *Earth-Science Reviews*, 138, 469–486. <https://doi.org/10.1016/j.earscirev.2014.07.006>

Zhang, Q., Lei, Y., & Wang, C. (2004). Analysis of sediment outflow of turbidity current in Naodehai Reservoir In. M. Wieland (Ed.), *New developments in dam engineering* (pp. 1053–1057). Taylor and Francis.

Zhou, Z., Chen, L., Tao, J., Gong, Z., Guo, L., van der Wegen, M., et al. (2020). The role of salinity in fluvio-deltaic morphodynamics: A long-term modelling study. *Earth Surface Processes and Landforms*, 45(3), 590–604. <https://doi.org/10.1002/esp.4757>

Zhu, Q., Wang, Y. P., Gao, S., Zhang, J., Li, M., Yang, Y., & Gao, J. (2017). Modeling morphological change in anthropogenically controlled estuaries. *Anthropocene*, 17, 70–83. <https://doi.org/10.1016/j.ancene.2017.03.001>

Zhu, Q., & Wiberg, P. L. (2022). The importance of storm surge for sediment delivery to microtidal marshes. *Journal of Geophysical Research: Earth Surface*, 127(9), e2022JF006612. <https://doi.org/10.1029/2022JF006612>

References From the Supporting Information

Adam, E., & Suleiman, M. (2022). Reservoir sediment management practices in Sudan: A case study of Khashm El-Girba Dam. In C. Sumi (Ed.), *Wadi flash floods, natural disaster science and mitigation engineering: DPR1 reports* (pp. 455–471). Springer Nature.

Alliau, D., Peteuil, C., & Huybrechts, N. (2016). Using an eco-friendly flushing event to calibrate 3D sediment transport model through a reservoir: The case study of Champagneux run-of-river dam on the Rhône River, France. In S. Bourban (Ed.), *Proceedings of the 23rd TELEMAC-MASCARET User Conference 2016* (pp. 49–53). HR Wallingford.

Avendaño-Salas, C., Sanz Montero, M. E., & Cobo Rayán, R. (2000). State of the art of reservoir sedimentation management in Spain. In *Proceedings of International Workshop and Symposium on Reservoir Sedimentation Management* (pp. 27–34). WEC.

Atkinson, E. (1996). *The feasibility of flushing sediment from reservoirs*. HR Wallingford.

Besnier, A.-L., Secher, M., & Tassi, P. (2016). Numerical modelling of the sediment dynamics in the Saint-Martin-la-Porte reservoir, France. In G. Constantinescu (Ed.), *River flow 2016* (pp. 1426–1434).

Booij, N., Ris, R. C., & Holthuijsen, L. H. (1999). A third-generation wave model for coastal regions: 1. Model description and validation. *Journal of Geophysical Research*, 104(C4), 7649–7666. <https://doi.org/10.1029/98jc02622>

Camenen, B., Naudet, G., Dramais, G., Le Coz, J., & Paquier, A. (2019). A multi-technique approach for evaluating sand dynamics in a complex engineered piedmont river system. *Science of the Total Environment*, 657, 485–497. <https://doi.org/10.1016/j.scitotenv.2018.11.394>

Cattaneo, F., Guillard, J., Diouf, S., O'Rourke, J., & Grimardias, D. (2021). Mitigation of ecological impacts on fish of large reservoir sediment management through controlled flushing – The case of the Verbois dam (Rhône River, Switzerland). *Science of the Total Environment*, 756, 144053. <https://doi.org/10.1016/j.scitotenv.2020.144053>

Chaudhry, M. A., Habib-ur-Rehman, M., Akhtar, M. N., & Hashmi, H. N. (2014). Modeling sediment deposition and sediment flushing through reservoirs using 1-D numerical model. *Arabian Journal for Science and Engineering*, 39(2), 647–658. <https://doi.org/10.1007/s13369-013-0670-6>

Chaudhry, M. R. (1982). Flushing operations of Warsak reservoir sediment. In *Proceedings of the Pakistan Engineering Congress* (Vol. 454, pp. 246–265).

Deltares. (2014c). *RGFGRID, user manual. Version 4.00*. Delft.

den Boer, V. J. E. (2011). *Preliminary study of the flushing operations of the Langmann reservoir, Austria* (Master thesis). Delft University of Technology.

Dhivert, E., Grosbois, C., Coynel, A., Lefèvre, I., & Desmet, M. (2015). Influences of major flood sediment inputs on sedimentary and geochemical signals archived in a reservoir core (Upper Loire Basin, France). *Catena*, 126, 75–85. <https://doi.org/10.1016/j.catena.2014.10.030>

Doretto, A., Bo, T., Bona, F., Apostolo, M., Bonetto, D., & Fenoglio, S. (2019). Effectiveness of artificial floods for benthic community recovery after sediment flushing from a dam. *Environmental Monitoring and Assessment*, 191(2), 88. <https://doi.org/10.1007/s10661-019-7232-7>

Eriksen, K., & Easthouse, K. (2010). Howard Hanson Dam sediment management project. In *Paper presented at 2nd Joint Federal Interagency Conference*. Las Vegas.

Folegot, S., Bruno, M. C., Larsen, S., Kaffas, K., Pisaturo, G. R., Andreoli, A., et al. (2021). The effects of a sediment flushing on Alpine macroinvertebrate communities. *Hydrobiologia*, 848(17), 3921–3941. <https://doi.org/10.1007/s10750-021-04608-8>

- Frémion, F., Bordas, F., Mourier, B., Lenain, J. F., Kestens, T., & Courtin-Nomade, A. (2016a). Influence of dams on sediment continuity: A study case of a natural metallic contamination. *Science of the Total Environment*, *547*, 282–294. <https://doi.org/10.1016/j.scitotenv.2016.01.023>
- Frémion, F., Courtin-Nomade, A., Bordas, F., Lenain, J. F., Jugé, P., Kestens, T., & Mourier, B. (2016b). Impact of sediments resuspension on metal solubilization and water quality during recurrent reservoir sluicing management. *Science of the Total Environment*, *562*, 201–215. <https://doi.org/10.1016/j.scitotenv.2016.03.178>
- Furukawa, H., Fukushige, Y., Okumura, H., Asaoka, Y., & Nagabayashi, H. (2019). Measurement of non-uniform suspended sediment transport during sluicing and flushing operations at the Seto-Ishi Dam on the Kumagawa River. *Journal of Japan Society of Civil Engineers, Ser. B1 (Hydraulic Engineering)*, *75*(2), 853–858. https://doi.org/10.2208/jsejhe.75.2_i_853
- Gellis, A. C., Webb, R. M. T., McIntyre, S. C., & Wolfe, W. J. (2006). Land-use effects on erosion, sediment yields, and reservoir sedimentation: A case study in the Lago Loíza Basin, Puerto Rico. *Physical Geography*, *27*(1), 39–69. <https://doi.org/10.2747/0272-3646.27.1.39>
- Gibson, S., & Boyd, P. (2016). Monitoring, measuring, and modeling a reservoir flush on the Niobrara River in the Sandhills of Nebraska. In G. Constantinescu (Ed.), *River flow 2016* (pp. 1448–1455).
- Gibson, S., & Crain, J. (2019). *Modeling sediment concentrations during a drawdown reservoir flush: Simulating the fall creek operations with HEC-RAS*. ERDC/TN RSM-19-7. U.S. Army Engineer Research and Development Center.
- Guertault, L., Camenen, B., Peteuil, C., & Paquier, A. (2014). Long term evolution of a dam reservoir subjected to regular flushing events. *Advances in Geosciences*, *39*, 89–94. <https://doi.org/10.5194/adgeo-39-89-2014>
- Guertault, L., Camenen, B., Paquier, A., & Peteuil, C. (2018). A one-dimensional process-based approach to study reservoir sediment dynamics during management operations. *Earth Surface Processes and Landforms*, *43*(2), 373–386. <https://doi.org/10.1002/esp.4249>
- Hassanzadeh, Y. (1995). The removal of reservoir sediment. *Water International*, *20*(3), 151–154. <https://doi.org/10.1080/02508069508686467>
- Huang, J., Greimann, B., & Kimbrel, S. (2019). Simulation of sediment flushing in Paonia reservoir of Colorado. *Journal of Hydraulic Engineering*, *145*(12), 06019015. [https://doi.org/10.1061/\(asce\)hy.1943-7900.0001651](https://doi.org/10.1061/(asce)hy.1943-7900.0001651)
- IHA. (2022). *Sediment management case studies: India - Nathpa Jhakri*. International Hydropower Association. Retrieved from <https://www.hydropower.org/sediment-management-case-studies/india-nathpa-jhakri>
- Kaffas, K., Pisinaras, V., Al Sayah, M. J., Santopietro, S., & Righetti, M. (2021). A USLE-based model with modified LS-factor combined with sediment delivery module for Alpine basins. *Catena*, *207*, 105655. <https://doi.org/10.1016/j.catena.2021.105655>
- Launay, M., Dugué, V., Faure, J. B., Coquery, M., Camenen, B., & Le Coz, J. (2019). Numerical modelling of the suspended particulate matter dynamics in a regulated river network. *Science of the Total Environment*, *665*, 591–605. <https://doi.org/10.1016/j.scitotenv.2019.02.015>
- Legout, C., Droppo, I., Coutaz, J., Bel, C., & Jodeau, M. (2018). Assessment of erosion and settling properties of fine sediments stored in cobble bed rivers: The Arc and Isère alpine rivers before and after reservoir flushing. *Earth Surface Processes and Landforms*, *43*(6), 1295–1309. <https://doi.org/10.1002/esp.4314>
- Leobacher, A., & Blauhut, A. (2010). Gerlos power station/Gmünd dam – Stabilization of a reservoir slope (Grasegger slope). *Geomechanics and Tunneling*, *3*(5), 462–469. <https://doi.org/10.1002/geot.201000041>
- Lepage, H., Launay, M., Le Coz, J., Angot, H., Miège, C., Gairoard, S., et al. (2020). Impact of dam flushing operations on sediment dynamics and quality in the upper Rhône River, France. *Journal of Environmental Management*, *255*, 109886. <https://doi.org/10.1016/j.jenvman.2019.109886>
- Liu, D., Nie, Q., Xiong, C., Yu, Z., Lv, Y., Zhang, S., et al. (2022). Sediment particle size composition in the riparian zone of the Three Gorges Reservoir. *Frontiers of Environmental Science*, *10*, 820700. <https://doi.org/10.3389/fenvs.2022.820700>
- Liu, W.-C., Hsu, M. H., & Kuo, A. Y. (2002). Modelling of hydrodynamics and cohesive sediment transport in Tanshui River estuarine system, Taiwan. *Marine Pollution Bulletin*, *44*(10), 1076–1088. [https://doi.org/10.1016/s0025-326x\(02\)00160-1](https://doi.org/10.1016/s0025-326x(02)00160-1)
- Luijendijk, A. P., Schipper, M., & Ranasinghe, R. (2019). Morphodynamic acceleration techniques for multi-timescale predictions of complex sandy interventions. *Journal of Marine Science and Engineering*, *7*(3), 78. <https://doi.org/10.3390/jmse7030078>
- Marot, D., Bouchard, J. P., & Alexis, A. (2005). Reservoir bank deformation modeling: Application to Grangent reservoir. *Journal of Hydraulic Engineering*, *131*(7), 586–595. [https://doi.org/10.1061/\(asce\)0733-9429\(2005\)131:7\(586\)](https://doi.org/10.1061/(asce)0733-9429(2005)131:7(586))
- Meile, T., Bretz, N. V., Imboden, B., & Boillat, J. L. (2014). Reservoir sedimentation management at Gebidem dam (Switzerland). In M. R. Schleiss (Ed.), *Reservoir sedimentation* (pp. 245–255). Taylor and Francis.
- Milne, B. E. (1969). A note on siltation in the Mangahao power project. In J. A. Hayward (Ed.), *Watershed management, Part 2, Proceedings of a Symposium on Watershed Management in Water Resources Development* (pp. 42–50). New Zealand Agricultural Engineering Institute.
- Moridi, A., & Yazdi, J. (2017). Sediment flushing of reservoirs under environmental considerations. *Water Resources Management*, *31*(6), 1899–1914. <https://doi.org/10.1007/s11269-017-1620-y>
- Morris, G. L. (2020b). Solving persistent water supply problems in Puerto Rico: Critical problems and actions. In *White paper for ASCE infrastructure committee*. San Juan.
- Nukazawa, K., Kajiwara, S., Saito, T., & Suzuki, Y. (2020). Preliminary assessment of the impacts of sediment sluicing events on stream insects in the Mimi River, Japan. *Ecological Engineering*, *145*, 105726. <https://doi.org/10.1016/j.ecoleng.2020.105726>
- OJSCEPP. (2018). Initial environmental examination, Kyrgyz republic: Uch-Kurgan hydropower plant modernization project. Document prepared by the consulting joint venture tractebel engineering and industriel elektrik maden LLC for the Asian development bank. In *Open joint stock company electric power plants*. Bishkek.
- Peteuil, C., Jodeau, M., De Linares, M., Valette, E., Alliau, D., Wirz, C., et al. (2018). Toward an operational approach for the characterization and modelling of fine sediments dynamics in reservoirs. In A. Paquier & N. Rivière (Eds.), *River flow 2018—9th International Conference on Fluvial Hydraulics, E3S web of conferences* (Vol. 40, p. 03028). <https://doi.org/10.1051/e3sconf/20184003028>
- Ranasinghe, R., Swinkels, C., Luijendijk, A., Roelvink, D., Bosboom, J., Stive, M., & Walstra, D. (2011). Morphodynamic upscaling with the MORFAC approach: Dependencies and sensitivities. *Coastal Engineering*, *58*(8), 806–811. <https://doi.org/10.1016/j.coastaleng.2011.03.010>
- Reckendorfer, W., Badura, H., & Schütz, C. (2019). Drawdown flushing in a chain of reservoirs - Effects on grayling populations and implications for sediment management. *Ecology and Evolution*, *9*(3), 1437–1451. <https://doi.org/10.1002/ece3.4865>
- Ren, S., Zhang, B., Wang, W. J., Yuan, Y., & Guo, C. (2021). Sedimentation and its response to management strategies of the Three Gorges Reservoir, Yangtze River, China. *Catena*, *199*, 105096. <https://doi.org/10.1016/j.catena.2020.105096>
- Roelvink, J. A. (2006). Coastal morphodynamic evolution techniques. *Coastal Engineering*, *53*(2–3), 277–287. <https://doi.org/10.1016/j.coastaleng.2005.10.015>
- Rollo, C., Bonnani, S., Sayah, S. M., Arbolí, J., & Braghini, M. (2018). Sedimentation management of Cerro del Águila Reservoir in Peru: A “mobile dam” for a highly erosive Andean watershed. In *Proceedings of the 26th international congress on large dams*. CRC Press.
- Schenk, L. N., & Bragg, H. M. (2014). Assessment of suspended-sediment transport, bedload, and dissolved oxygen during a short-term drawdown of Fall Creek Lake, Oregon, winter 2012–13. In *Open file report 2014–1114*. U.S. Geological Survey.

- Shelley, J., Hotchkiss, R. H., Boyd, P., & Gibson, S. (2022). Discharging sediment downstream: Case studies in cost effective, environmentally acceptable reservoir sediment management in the United States. *Journal of Water Resources Planning and Management*, 148(2), 05021028. [https://doi.org/10.1061/\(asce\)wr.1943-5452.0001494](https://doi.org/10.1061/(asce)wr.1943-5452.0001494)
- Shelley, J. E., Boyd, P. M., Dahl, T. A., Floyd, I. E., & Ramos-Villanueva, M. (2018). *Reservoir sediment management workshop for regulators, planners, and managers, Regional sediment management technical note ERDC/TN RSM-18-7*. U.S. Army Corps of Engineers.
- Sumi, T., Baoligao, B., & Morita, S. (2007). Characteristics of fine sediment discharge during sediment flushing of Unazuki Dam. *Journal of Hydroscience and Hydraulic Engineering, JSCE*, 25, 99–106.
- Sumi, T., Yoshimura, T., Asazaki, K., Kaku, M., Kashiwai, J., & Sato, T. (2015). Retrofitting and change in operation of cascade dams to facilitate sediment sluicing in the Mimikawa River Basin. In *Proceedings of 25th ICOLD Congress* (pp. 597–611).
- SWAN Team. (2021). *Swan: Scientific and technical documentation. Version 41.31AB*. Delft University of Technology. Retrieved from <http://www.swan.tudelft.nl>
- Tabios, III, G. Q. (2020). Reservoir sedimentation studies. In *Water Resources Systems of the Philippines: Modeling studies* (Vol. 4, pp. 165–209). Springer. https://doi.org/10.1007/978-3-030-25401-8_6
- TRMO. (2014). *Flood early warning and flood control integration project under the jurisdiction of the Tenth River Management Office in 2014*. Tenth River Management Office, WRA, MOEA.
- van Rijn, L. C. (2007). Unified view of sediment transport by currents and waves. I: Initiation of motion, bed roughness, and bed-load transport. *Journal of Hydraulic Engineering*, 133(6), 649–667. [https://doi.org/10.1061/\(asce\)0733-9429\(2007\)133:6\(649\)](https://doi.org/10.1061/(asce)0733-9429(2007)133:6(649))
- van Rijn, L. C. (2013). Sedimentation of sand and mud in reservoirs in rivers. Retrieved from <https://www.leovanrijn-sediment.com/papers/Reservoirsiltation2013.pdf>
- Wang, G., Wu, B., & Wang, Z. (2005). Sedimentation problems and management strategies of Sanmenxia Reservoir, Yellow River, China. *Water Resources Research*, 41(9), W09417. <https://doi.org/10.1029/2004WR003919>
- Wang, H.-W., Kondolf, M., Tullos, D., & Kuo, W. C. (2018). Sediment management in Taiwan's reservoirs and barriers to implementation. *Water*, 10(8), 1034. <https://doi.org/10.3390/w10081034>
- White, R. (2001). *Evacuation of sediments from reservoirs*. Thomas Telford.
- Wohl, E. E., & Cenderelli, D. A. (2000). Sediment deposition and transport patterns following a reservoir sediment release. *Water Resources Research*, 36(1), 319–333. <https://doi.org/10.1029/1999wr900272>
- Xia, Q., & Liu, J. (2003). Sediment management at Naodehai reservoir. In *Paper presented at World Water and Environmental Resources Congress 2003*. [https://doi.org/10.1061/40685\(2003\)54](https://doi.org/10.1061/40685(2003)54)
- Yang, X. (2003). Manual on sediment management and measurement. In *Operational hydrology report* (Vol. 47). World Meteorological Organization.
- Yu, Y., Xuefa, S., Houjie, W., Chengkun, Y., Shenliang, C., Yanguang, L., et al. (2013). Effects of dams on water and sediment delivery to the sea by the Huanghe (Yellow River): The special role of Water-Sediment Modulation. *Anthropocene*, 3, 72–82. <https://doi.org/10.1016/j.ancene.2014.03.001>
- Zamora, J. (2018). *Assessment of sediment handling strategies in the regulation pond of El Canadá hydropower plant, Guatemala*. Master thesis. Norwegian University of Science and Technology.
- Zhang, W.-Z., Shi, F., Hong, H., Shang, S., & Kirby, J. T. (2010). Tide-surge interaction intensified by the Taiwan Strait. *Journal of Geophysical Research*, 115(C6), C06012. <https://doi.org/10.1029/2009jc005762>
- Zhou, Z. (2007). *Reservoir sedimentation management in China*. Lecture notes. International Research and Training Center on Erosion and Sedimentation. Retrieved from <http://www.irtces.org/nszx/zt/training2007/ppt/Lecture%20-Zhou%20Zhide.pdf>
- Zhuang, S., Lu, X., Yu, B., Fan, X., & Yang, Y. (2021). Ascertain the pollution, ecological risk and source of metal(loid)s in the upstream sediment of Danjiang River, China. *Ecological Indicators*, 125, 107502. <https://doi.org/10.1016/j.ecolind.2021.107502>

**Reservoir mud releasing may suboptimize fluvial sand supply to coastal sediment budget:
Modeling the impact of Shihmen Reservoir case on Tamsui River estuary**

Yu-Ta Hsueh¹, Fu-Chun Wu^{1*}, Qinghua Ye², Steven Y. J. Lai³, and Yinphan Tsang⁴

¹Department of Bioenvironmental Systems Engineering, National Taiwan University, Taipei, Taiwan. ²Deltares, Delft, The Netherlands. ³Department of Hydraulic and Ocean Engineering, National Cheng Kung University, Tainan, Taiwan.

⁴Natural Resources and Environmental Management, University of Hawai'i at Mānoa, Honolulu, Hawai'i, USA.

(*Correspondence: fewu@ntu.edu.tw)

Contents of this file

Text S1 to S6

Figure S1 to S15

Table S1 to S2

Text S1. Delft3D Model

Delft3D, developed and maintained by Deltares, is an open-source model suite consisting of the Flow, Morphology, and Wave Modules [Lesser *et al.*, 2004; Deltares, 2014a, b]. The **Flow Module** solves the unsteady shallow-water equations under the assumptions of hydrostatic pressure and Boussinesq eddy viscosity [Deltares, 2014a]. The **Wave Module** adopts the phase-averaged SWAN model suitable for nearshore and estuaries [Booij *et al.*, 1999; Deltares, 2014b; SWAN Team, 2021]. It employs the action balance equation to compute the 2D field of wave action spectrum over a range of wave direction and frequency, taking into account the processes of wind energy input, wave generation and propagation, energy dissipation by bottom friction, whitecapping and depth-induced breaking, energy transfer by nonlinear wave-wave interactions, and refraction due to variations in depth and current. It also considers the longshore current and cross-shore setup driven by the wave-induced radiation stresses.

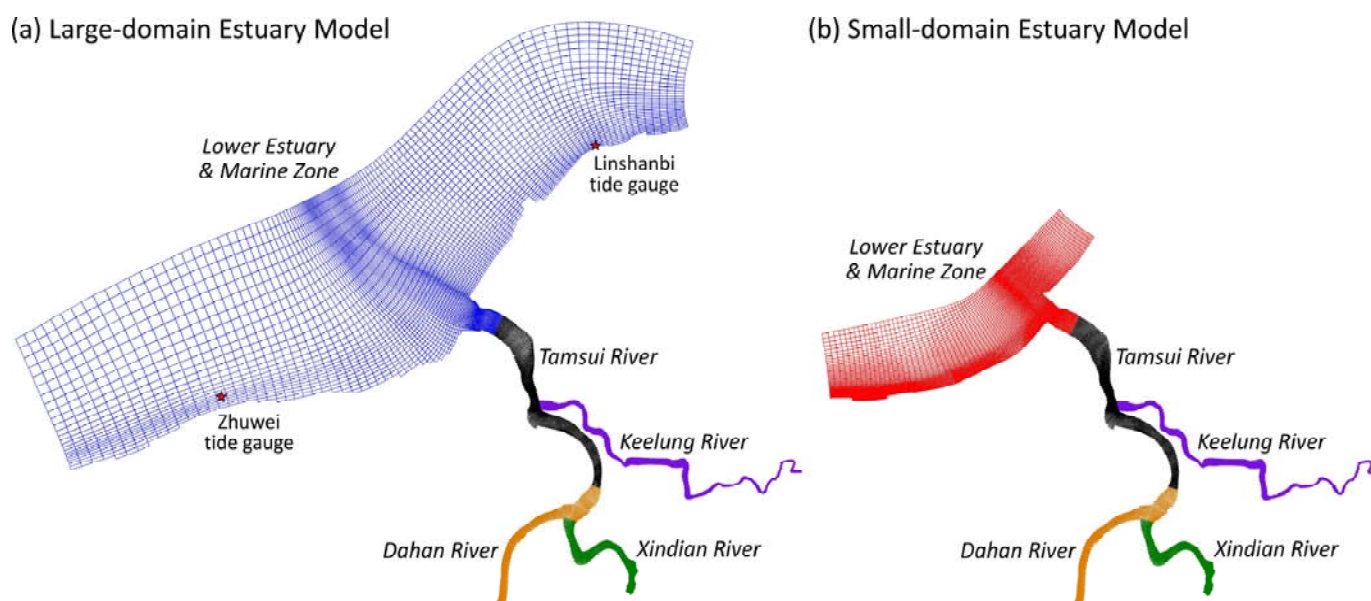
The **Morphology Module** employs the continuity equations of all sediment fractions to account for the contributions of suspended and bed loads. Non-cohesive sands (grain sizes $> 63 \mu\text{m}$) are transported as suspended and bed loads; cohesive muds (grain sizes $< 63 \mu\text{m}$) are transported as suspended load only. Suspended and bed load transport rates of sands (driven by currents and waves) are evaluated using the approach of *van Rijn* [1993] and *van Rijn et al.* [2001] (see Lesser [2009]). The exchange (erosion and deposition) fluxes of muds are determined using the Partheniades-Krone formulation [Partheniades, 1965], where the critical shear stresses for erosion and deposition (τ_E, τ_D) and erosion parameter M are to be calibrated. In this study, the default value of $\tau_D = 1,000 \text{ Pa}$ was used, implying a continuous deposition flux varying as a function of mud concentration and settling velocity [van der Wegen *et al.*, 2011b]. For each sand fraction, a median grain size D_{50} is specified to calculate settling velocity w_s . For each mud fraction, w_s must be specified by users (see Table S2 for calibrated parameter values).

Multi-layer Stratigraphy Model. In case of deposition, the deposited sediments are added to the top layer (surface layer with a fixed thickness), resulting in an upshifted bed surface. After mixing in the surface layer, the excess deposits are stored in the bookkeeping layer underneath. The bookkeeping

layer is filled up only to a specified thickness, if this thickness is exceeded a new bookkeeping layer is created atop the old one. If the number of bookkeeping layers exceeds the specified limit, the excess layers at the bottom of the stratigraphy stack are merged as a base layer, below which is a non-erodible bed. In case of erosion, only sediments in the surface layer are available for erosion, which lowers the bed surface. After erosion, the surface layer is replenished with sediment from the underlayer to retain a fixed thickness. In view of the sediment and flow characteristics investigated in this study, a surface layer of 0.2 m and 10 bookkeeping layers each of 1 m were chosen, based on the values suggested for similar sediment mixtures and morphodynamics [Geleynse *et al.*, 2010; van der Wegen *et al.*, 2011b; Dissanayake *et al.*, 2012; van der Vegt *et al.*, 2016; Valencia *et al.*, 2023].

Text S2. Computational Grid

For the **Flow Module**, a small-domain estuary model was nested in a large-domain estuary model. The small-domain model was focused on the estuarine/nearshore areas, covering a domain from the 30 m isobath up to the tributary tidal limits. To resolve local hydrodynamic and morphodynamic processes, the small-domain model used finer grid sizes varying from 350 m in the outer nearshore zone to 50 m in the intertidal/estuarine areas of interest, aimed to balance the computational efficiency and accuracy. The large-domain model extended cross-shore to the 60 m isobath, and alongshore to encompass two tide gauges (Linshanbi and Zhuwei) used for model validation. The large-domain model used coarser grid sizes, varying from 150 m in the nearshore to 800 m in offshore, supplying the hydrodynamic boundary conditions to the small-domain model after each time step. To enhance the computational efficiency, both domains were divided into five subdomains using the **domain decomposition (DD) technique** [Deltares, 2014c], these include: (1) lower estuary and marine zone, (2) Tamsui River, (3) Dahan River, (4) Xindian River, and (5) Keelung River (see figure below). Parallel computing was performed on these subdomains by exchanging information along the shared DD boundaries. For the river channels, the same subdomains were used by both the large- and small-domain models, with the grid sizes ranging from 10 to 100 m. Sensitivity tests revealed that further reducing the grid size led to no substantial differences in the simulation results.



Decomposition of (a) large- and (b) small-domain estuary models. Both models use the same river subdomains.

For the **Wave Module**, four layers of nested grid were used: (1) far-field open seas, covering an area of $2500 \times 2000 \text{ km}^2$ encompassing East and South China Seas, Taiwan Strait, Philippine Sea, and Pacific Ocean, (2) surrounding waters, covering an area of $400 \times 550 \text{ km}^2$, (3) northern waters, and (4) littoral zone, including a large- and a small-domain version (with 40-800 m and 40-350 m resolutions), which were coupled with the large- and small-domain estuary models. The cross-shore lateral boundaries of the littoral zone models were slightly expanded to prevent from the shadow areas of wave propagation [Deltares, 2014b].

Text S3. Input Reduction and Morphological Acceleration Techniques

Since the morphodynamic timescales are much longer than hydrodynamic timescales, three techniques were used to improve the efficiency of medium- to long-term (months to years) simulations, including: (a) input reduction, (b) parallel computing, and (c) morphological acceleration.

For **input reduction**, two approaches were used to schematize the hydrodynamic boundary conditions. (1) The first is wave input reduction, which schematizes the full wave climate as a set of *representative waves* with equal energy fluxes in the scatter plot of wave height vs. wave direction (Figure S3a) that best reproduce the longshore transport patterns of the full wave climate (Figure S3b) [Benedet et al., 2016]. (2) The second is a *morphological tide*, which is aimed to reproduce the same morphological changes as the full tidal time series using a shorter, representative diurnal tidal period (Figure S4a), which best retains the spring-neap cycle-averaged residual transport (Figures S4b-c) [Lesser, 2009; Roelvink & Reniers, 2012].

Simulations with individual *representative waves* were performed in parallel for a shorter time period (a few cycles of *morphological tide*), using a **parallel online approach** termed *Mormerge* [Roelvink, 2006]. In this study, the hydrodynamic simulation of non-typhoon periods was performed for 10 cycles of *morphological tide*, with 5 *representative waves* run in parallel. The morphological change in each time step was obtained by summing the results from individual *representative wave*, weighted by the proportion of each wave condition in the annual wave climate [Roelvink, 2006; Benedet et al., 2016]. The updated bathymetry was then used in the subsequent time step. *Mormerge* approach facilitates a smoother morphological evolution, allowing a greater acceleration factor to achieve a more efficient morphodynamic simulation [Luijendijk et al., 2019], as described below.

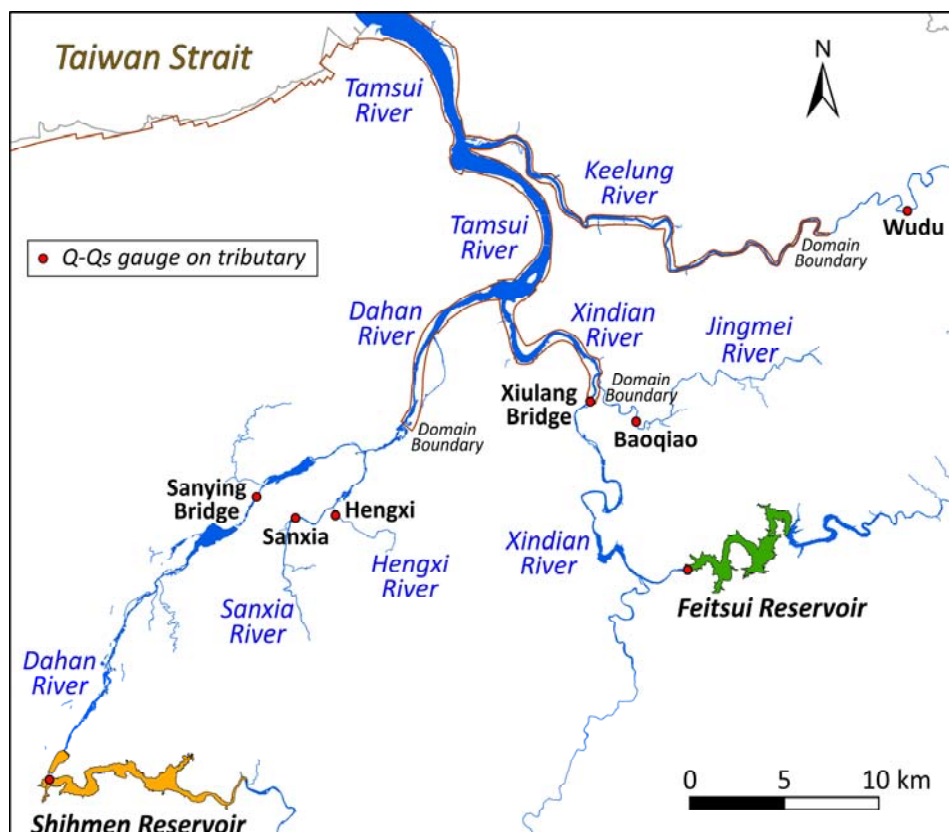
The **morphological acceleration factor**, f_{mor} , scales up the bed elevation changes calculated in each hydrodynamic time step, as expressed in equation (1), namely, the sediment continuity equation. This is equivalent to increasing the morphodynamic time step by a factor of f_{mor} , thereby accelerating the morphologic evolution [Lesser et al., 2004; Roelvink, 2006], and allowing for a long morphodynamic simulation to finish in a shorter period of hydrodynamic simulation. In this study, the morphodynamic simulations of non-typhoon periods were run for 100 cycles of *morphological tide* (equivalent to 103 days), achieved by performing hydrodynamic simulations over 10 cycles of *morphological tide* using $f_{mor} = 10$. However, there are upper limits of f_{mor} applicable to a given morphodynamic simulation. A robust, objective method to determine the greatest allowable f_{mor} does not exist [Ranasinghe et al., 2011]. Selection of a suitable f_{mor} remains a matter of judgement and sensitivity test. Lesser [2009] suggested that f_{mor} within 10-100 is suitable for coastal environments with significant wave actions.

We conducted a series of sensitivity tests for evolution of estuarine morphology over 700 cycles of *morphological tide* (equivalent to 2 yrs) using $f_{mor} = 10, 50, 70, 100$ and 140 , respectively, for 70, 14, 10, 7 and 5 cycles of *morphological tide*. The results revealed that the morphological changes in estuary zone were similar for all f_{mor} values used. However, in the mouth zone, the morphological changes resulting from $f_{mor} = 140$ deviated from those obtained with smaller f_{mor} , attributed to a violation of the linear assumption when a large f_{mor} was used in the wave-dominated mouth zone. Accordingly, a value of $f_{mor} = 10$ (much smaller than 100) was used in this study.

Text S4. Flow vs. Suspended Sand Load ($Q-Q_s$) Rating Curves of Downstream Tributaries

The discharge vs. suspended sand load ($Q-Q_s$) rating curves were derived from the long-term records (1991-2018) at six gauges on the downstream tributaries (see figure below for locations). These gauges are: Sanying Bridge (on Dahan River), Sanxia (on Sanxia River), Hengxi (on Hengxi River), Xiulang Bridge (on Xindian River), Baoqiao (on Jingmei River), and Wudu (on Keelung River). They are all located at upstream of the domain boundaries, thus these rating curves were used to specify the time series inputs of sand SSC on river boundaries. The tributary sands were sourced mainly from hillslope and channel erosion. In the $Q-Q_s$ rating curves listed below, Q_s are in ton/day, and Q are in m^3/s :

- Sanying Bridge: $\log Q_s = 0.139(\log Q)^2 + 0.921(\log Q) + 0.782$ ($R^2 = 0.89$) (S1a)
 Sanxia: $\log Q_s = 0.421(\log Q)^2 + 0.558(\log Q) + 0.534$ ($R^2 = 0.89$) (S1b)
 Hengxi: $\log Q_s = 0.393(\log Q)^2 + 0.859(\log Q) + 0.274$ ($R^2 = 0.88$) (S1c)
 Xiulang Bridge: $\log Q_s = 0.412(\log Q)^2 - 0.010(\log Q) + 1.202$ ($R^2 = 0.75$) (S1d)
 Baoqiao: $\log Q_s = 0.386(\log Q)^2 + 0.542(\log Q) + 0.731$ ($R^2 = 0.85$) (S1e)
 Wudu: $\log Q_s = 0.337(\log Q)^2 + 0.372(\log Q) + 0.842$ ($R^2 = 0.82$) (S1f)



Six gauges (on downstream tributaries) used to derive the flow vs. suspended sand load ($Q-Q_s$) rating curves.

Text S5. Model Validation

(1) Tide levels during non-typhoon period

The hourly tide levels during a non-typhoon period (6/10–7/9, 2008) were used to validate the Flow Module under regular climate condition. As morphodynamics were not simulated, the large-domain estuary model was used to perform the hydrodynamic simulations for a period of one month, covering two neap-spring tidal cycles. Daily flows were specified at the landward boundaries, wind waves were not considered.

The results at Linshanbi, Tamsui River mouth, and Zhuwei tide gauges (Figure S5) show that the tide level variations during the flood/ebb phases and neap-spring cycles are well reproduced by the model, confirmed by the nearly perfect skill scores of 0.99–1 (Table 2). The RMSE values are 0.10–0.11 m, all < 5% of the mean tidal range (2.2 m). The negative biases, ranging from -0.01 to -0.03 m, indicate a consistent trend of slight underestimation. Overall, the model performance is excellent.

(2) Water levels during typhoon period

The hourly water levels observed at three tide gauges and six flow gauges during Typhoon Sinlaku (9/10–9/19, 2008) were used to validate the model results under typhoon condition. The results at tide gauges are shown in Figures S6a-c, and those at flow gauges are shown in Figures S6d-i. Water levels at tide gauges were less affected by typhoon. The rising/falling limbs of the flood hydrograph observed at flow gauges are well reproduced by the model. The RMSE values are between 0.13–0.23 m at most gauges (Table 2), except those at Bailing Bridge and Dazhi Bridge (0.39 and 0.55 m), which are 2 to 3 times greater as the choked water levels at narrow cross-sections blocked by bridge piers during flood peaks were not fully resolved by the model. Most biases are negative, indicating a prevailing trend of underestimation. Nevertheless, the skill scores ranging 0.93–1 indicate excellent model performance.

(3) Flow velocities over tidal cycle

Flow velocities over a tidal cycle, recorded semi-hourly, were used to validate the Flow Module. The time series cross-sectional velocities during a non-typhoon period (2008/7/3) at five flow gauges (Guandu Bridge, Taipei Bridge, Xinhai Bridge, Zhongzheng Bridge, and Bailing Bridge) are shown in Figure S7. The observed patterns of tidal asymmetry were well reproduced by the model. The RMSE values ranging between 0.07–0.19 m/s (Table 2), with dominant positive biases, indicate a prevailing trend of slight overestimation. The skill scores are all > 0.75, of which four are between 0.96–0.99, indicating excellent model performance in depicting the velocity reversal observed in estuarine systems.

(4) Wave heights during typhoon period

Significant wave heights H_s observed at four wave gauges (Taipei Port, Hsinchu Buoy, Longdong Buoy, Guishandao Buoy) during Typhoon Sinlaku (9/10–9/19, 2008) were used to validate the Wave Module. The results are presented in Figure S8, where good agreement between the simulated and observed H_s is shown. Skill scores ranging 0.95–0.97 (Table 2) indicate excellent model performance in capturing the spatiotemporal variations of wave field during typhoon along the northern nearshore. The RMSE value of 0.33 m at Taipei Port is < 24% of the mean wave height (= 1.4 m), with prevalent positive biases indicating a trend of slight overestimation.

(5) Estuarine SSC during mud release events

The time series of SSC observed at Guandu Bridge station during the mud release events in 2008 were used to validate the sediment transport model (Figures S9a-c). Overall, the variations of SSC are well captured by the model. The skill scores of SSC are lower than those of water level and velocity (Table 2), yet the skill scores ranging between 0.71–0.83 indicate a reasonably excellent model performance. The sustained high SSC observed during the post-peak low-flow periods of Sinlaku and Jangmi and the lower flood flows of Fung-Wong are attributed to the well-known local turbidity maximum present near the Guandu Bridge station. This turbidity maximum is induced by salinity intrusion and estuarine baroclinic circulation that occur during low flows, trapping suspended sediment in the Guandu deep channel (Figure S9d) [Hsu *et al.*, 2006; Liu *et al.*, 2007; Chen *et al.*, 2015; Liu *et al.*, 2022]. Although this locally sustained high SSC during low flows was not captured by the 2DH model, its effects on the entire model domain would be minimal given the flood hydrographs used in Stage 1 (Figure 5b) and the moderate tributary inflows (annual mean flows) used in Stage 2.

Text S6. Zonal Budgets of Sand and Mud during Typhoon and Non-typhoon Periods

During typhoon periods, sands were mainly sourced from the tributaries (Figure S14a), with a total of 3.62 M ton input to the estuary zone, while 2.51 M ton (= 69% of input) was transported to the mouth zone, resulting in a net budget of +0.59 Mm³. For the mouth zone, the total sand input was 2.86 M ton (= sum of fluvial supply 2.51 M ton and wave-induced longshore drift 0.35 M ton) yet only 0.83 M ton was exported, indicating that more than 70% of the sand input was deposited in the mouth zone. The net budget of +1.28 Mm³ in the mouth zone was > twice the net budget in the estuary zone.

Due to higher mobility of mud, during typhoon periods a vast amount of 3.16 M ton (= 95% of 3.34 M ton mud input to the estuary zone) was transported to the mouth zone (Figure S14b), resulting in a relatively small net budget of +0.14 Mm³ in the estuary zone. The amount of mud input to the mouth zone (sum of fluvial supply 3.16 M ton and longshore drift 0.09 M ton) was almost entirely (> 97%) exported by flood advection and wave dispersion. As a result, the net budget of +0.07 Mm³ in mouth zone was only half of that in estuary zone.

During non-typhoon periods, bed shear stresses became weaker, the upstream sand supply dropped to 0.002 M ton (Figure S14c), being three orders of magnitude smaller than that during typhoon periods (= 3.62 M ton). The main drive of sand transport in the estuary zone was tidal currents. Due to tidal asymmetry, the seaward transport during ebb tides was greater than the landward transport during flood tides. The residual sand transport to the mouth zone was 0.09 M ton, rendering a negative net budget of -0.06 Mm³ in the estuary zone. Sand input to mouth zone was 0.26 M ton (sum of fluvial supply 0.09 M ton and longshore drift 0.17 M ton), of which 30% (0.08 M ton) was exported by tidal currents and waves. The net sand budget of +0.11 Mm³ was one order of magnitude smaller than that during typhoons (+1.28 Mm³).

Similarly, during non-typhoon periods the upstream mud supply of 0.06 M ton (Figure S14d) was two orders of magnitude smaller than that during typhoon periods (= 3.34 M ton). Yet, 0.32 M ton of mud (70% of mud deposits in the estuary and mouth zones during typhoon periods) was resuspended and exported to offshore by waves and tidal currents. The resulting negative net budgets of mud in the estuary and mouth zones were -0.09 and -0.05 Mm³, respectively.

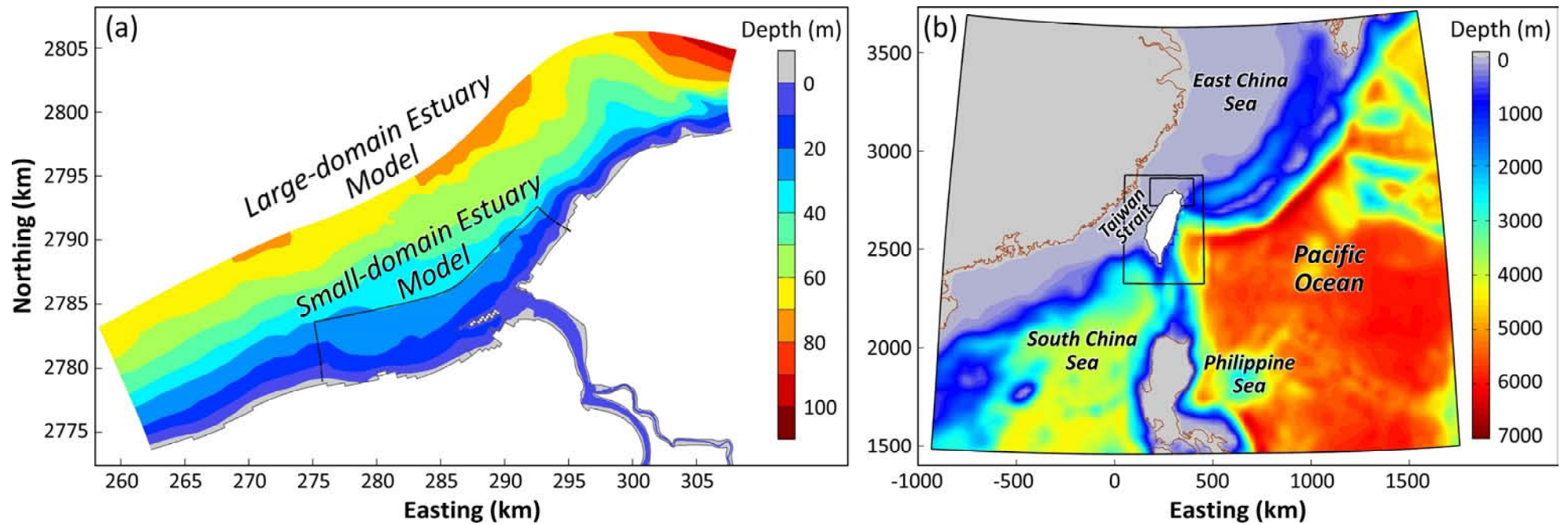


Figure S1. Bathymetric maps. (a) Estuary model domains. Small-domain model covers the estuarine and nearshore areas. Large-domain model extends to offshore. (b) Wave model domains. The boundaries of the far-field open seas, surrounding waters, and northern waters are also shown.

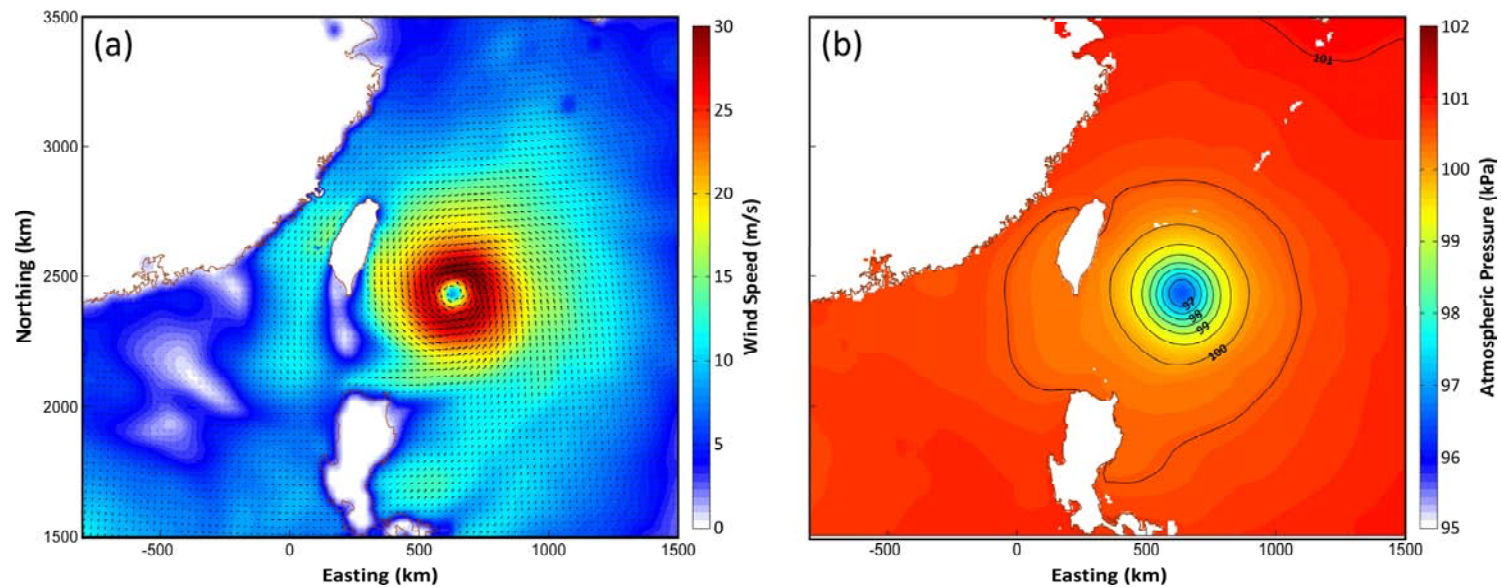


Figure S2. ERA5 reanalysis data: (a) wind field, and (b) atmospheric pressure field during Typhoon Sinlaku (2008/9/11, 22:00, Taiwan, GMT+8).

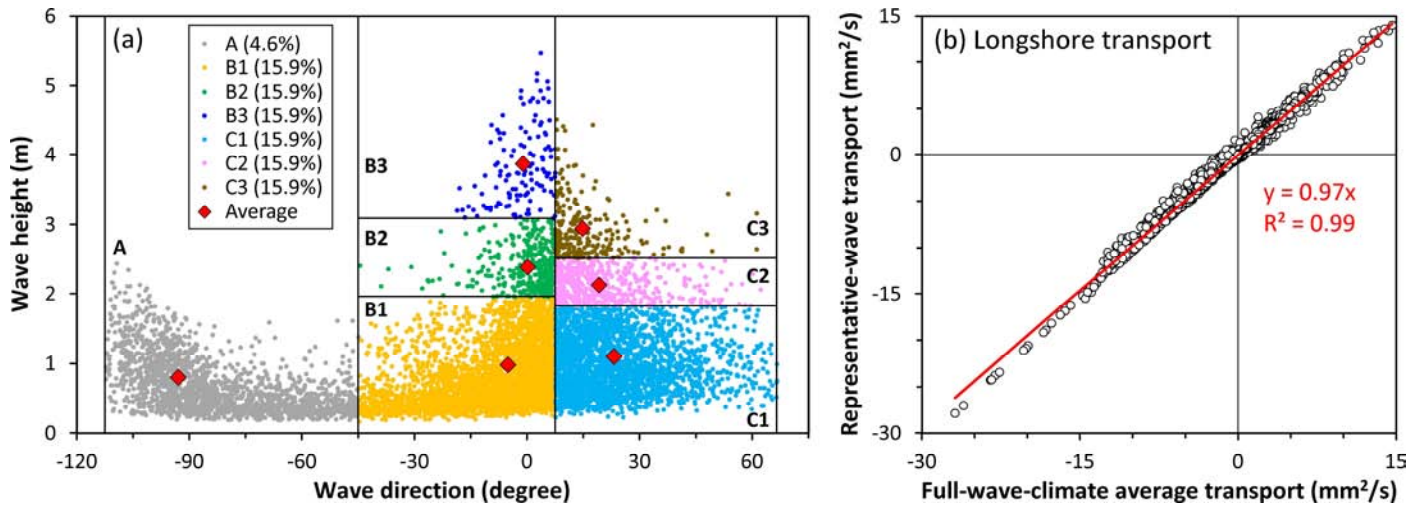


Figure S3. (a) Scatter plot of wave height vs. wave direction. Full wave climate was schematized as seven partitioned representative waves, with equal energy flux (15.9%) in each subgroup of B and C zones. Red diamonds indicate average of each subgroup. (b) Representative waves reproduced optimally the longshore sediment transport of full wave climate (positive northeastward), with the trend line having a slope $\rightarrow 1$ and an $R^2 \rightarrow 1$. B3 and C3 subgroups were not used in our simulations of typhoon seasons as these subgroups are driven by strong northeast monsoons in winter and spring (non-typhoon seasons).

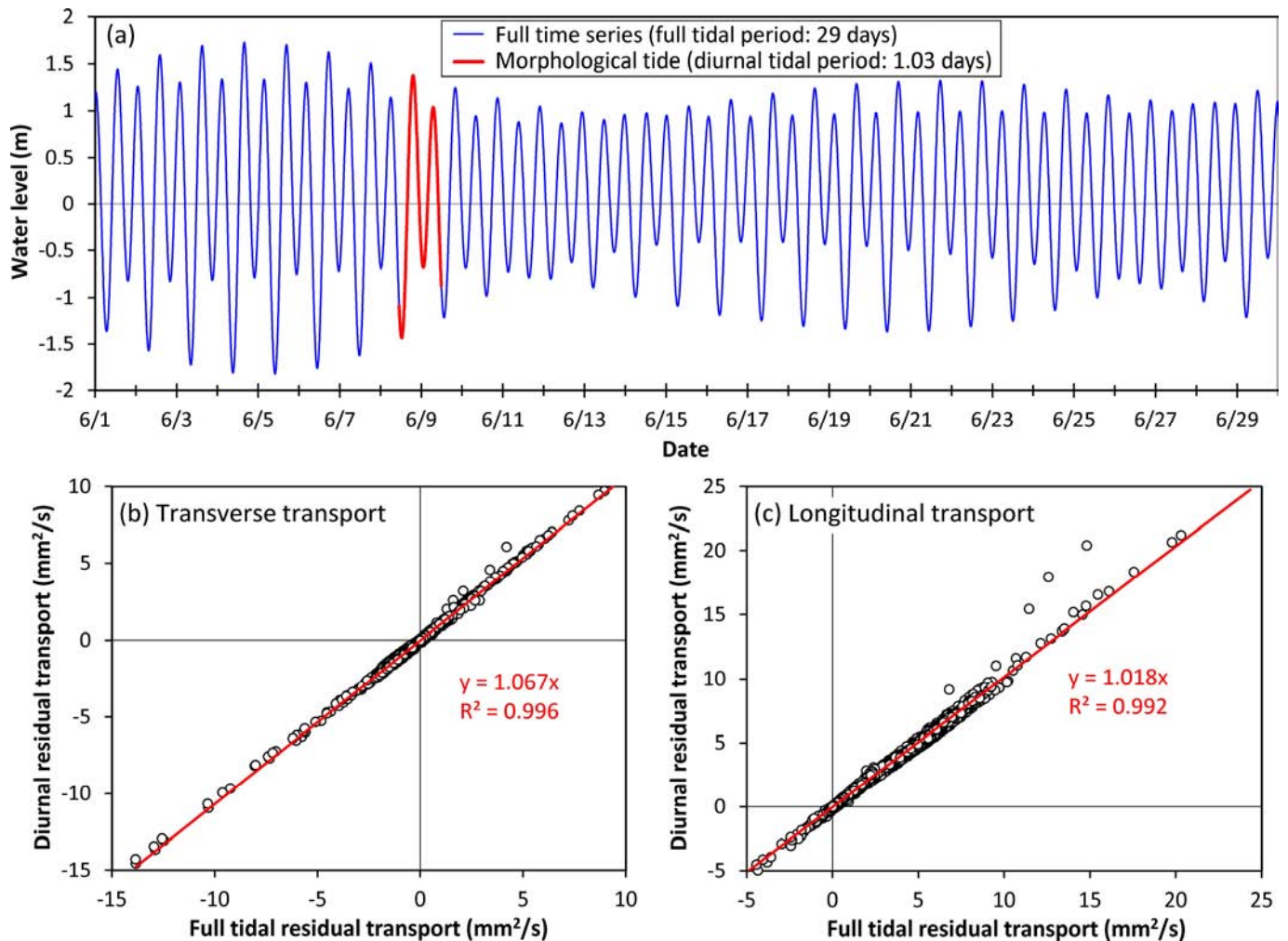


Figure S4. (a) Time series of tide level at Tamsui River mouth (full tidal period: 29 day) and morphological tide (diurnal period: 1.03 day). (b-c) Morphological tide best retains spring-neap cycle-averaged residual sediment transports, with trend lines having slopes $\rightarrow 1$ and $R^2 \rightarrow 1$, revealed by scatter plots of transverse and longitudinal residual transports (positive to the right bank or seaward).

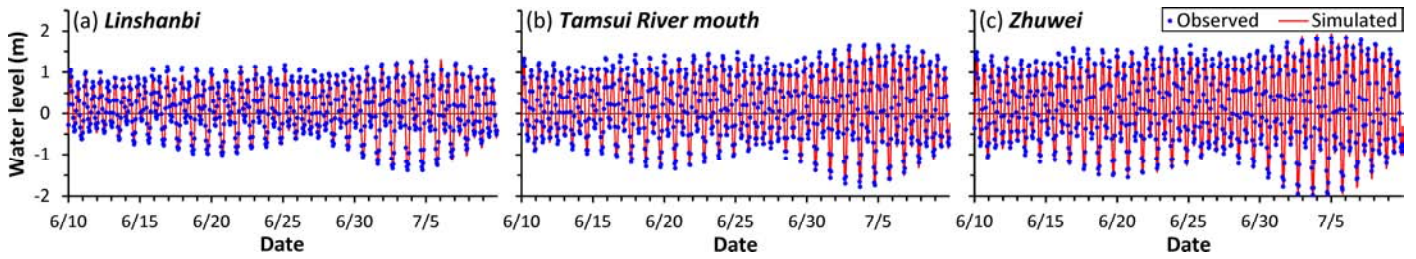


Figure S5. Time series of observed and simulated tide levels during a non-typhoon period (6/10–7/9, 2008) at three tide gauges: (a) Linshanbi; (b) Tamsui River mouth; (c) Zhuwei (locations see Figure 3).

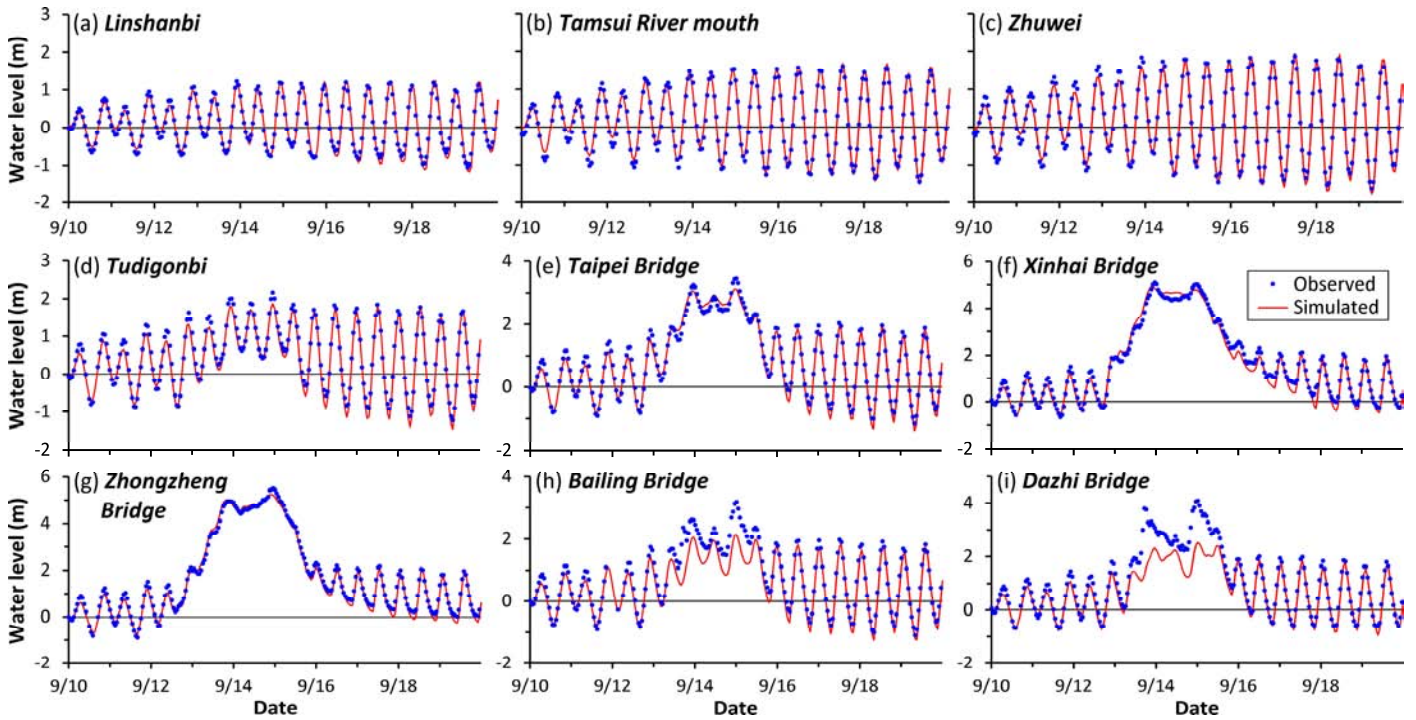


Figure S6. Time series of observed and simulated water levels during Sinlaku at three tide gauges and six flow gauges: (a) Linshanbi, (b) Tamsui River mouth, (c) Zhuwei, (d) Tudigonbi, (e) Taipei Bridge, (f) Xinhai Bridge, (g) Zhongzheng Bridge, (h) Bailing Bridge, and (i) Dazhi Bridge (see Figures 3a & 4a for locations).

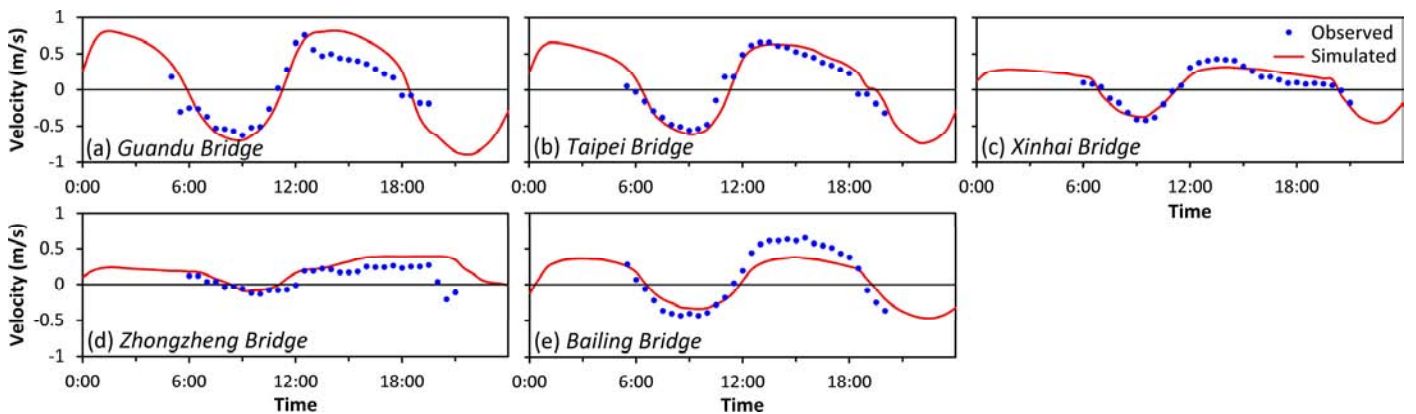


Figure S7. Time series of observed and simulated estuarine velocities over a semidiurnal tidal cycle in non-typhoon period (2008/7/3) at five flow gauges: (a) Guandu Bridge, (b) Taipei Bridge, (c) Xinhai Bridge, (d) Zhongzheng Bridge, and (e) Bailing Bridge (locations see Figure 4a). Positive and negative velocities indicate seaward and landward.

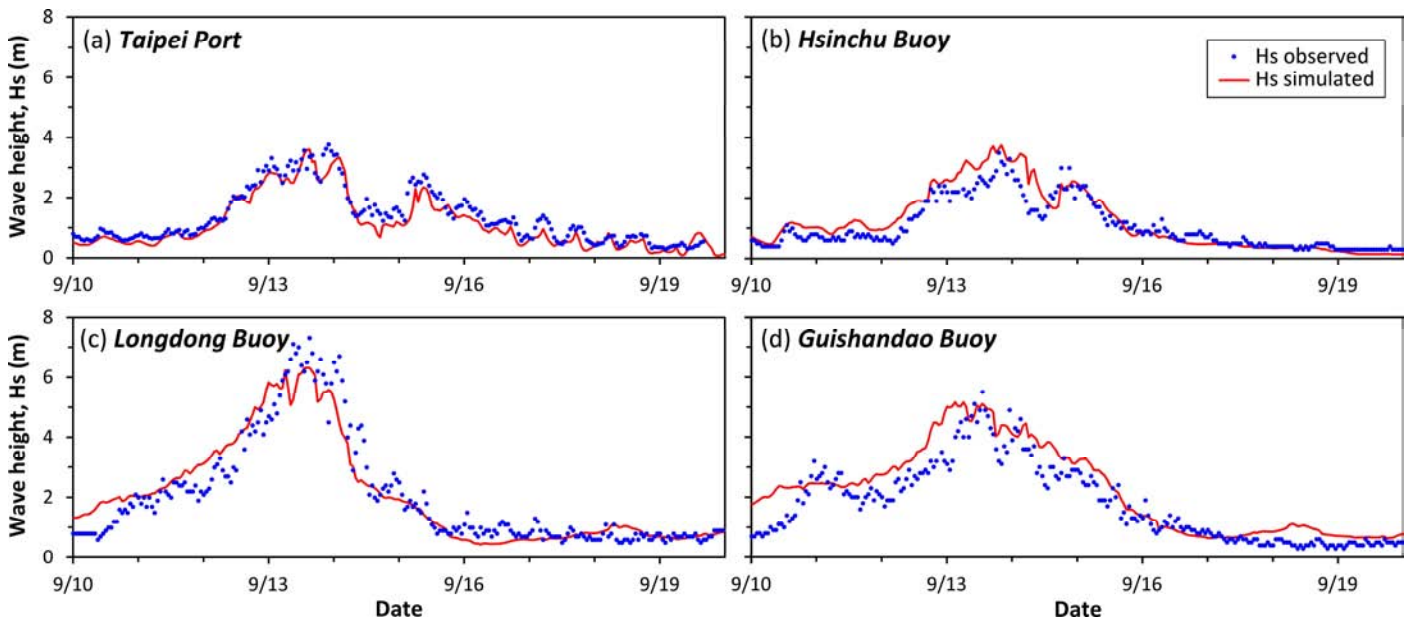


Figure S8. Time series of observed and simulated significant wave heights H_s during Typhoon Sinlaku, at four wave gauges: (a) Taipei Port, (b) Hsinchu Buoy, (c) Longdong Buoy, and (d) Guishandao Buoy (see Figure 3a for locations).

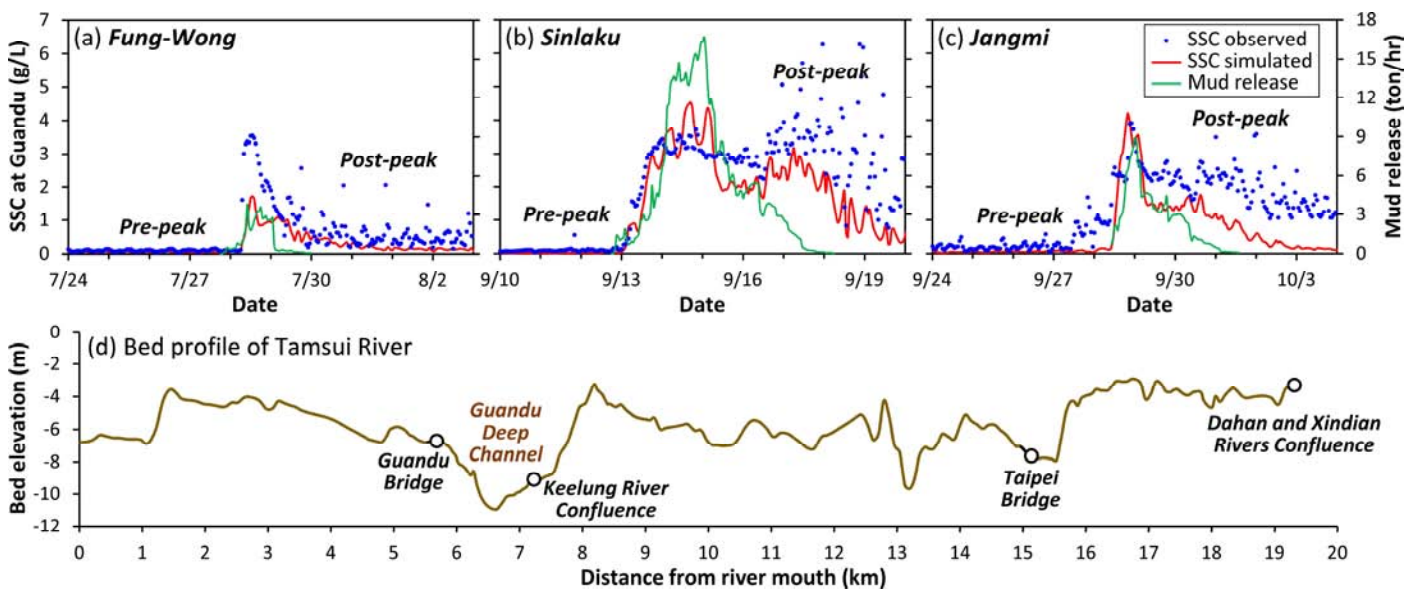


Figure S9. (a-c) Time series of observed and simulated SSC at Guandu Bridge station, along with the time series of reservoir mud release, during three typhoons in 2008: Fung-Wong (7/24–8/2), Sinlaku (9/10–9/19), and Jangmi (9/24–10/3). (d) Bed profile along the thalweg of the Tamsui River. The sustained high SSC observed during the post-peak low flows of Sinlaku and Jangmi and lower flood flows of Fung-Wong are attributable to the well-known local turbidity maximum present near the Guandu Bridge station. This turbidity maximum is induced by salinity intrusion and estuarine baroclinic circulation that particularly occur during low flows, trapping suspended sediment in the Guandu deep channel [e.g., Hsu *et al.*, 2006; Liu *et al.*, 2007; Chen *et al.*, 2015; Liu *et al.*, 2022]. Although this locally sustained high SSC during low flows was not captured by the 2DH model, its effects on the entire model domain would be minimal given the flood flows used in Stage 1 and the moderate tributary inflows (annual mean flows) used in Stage 2.

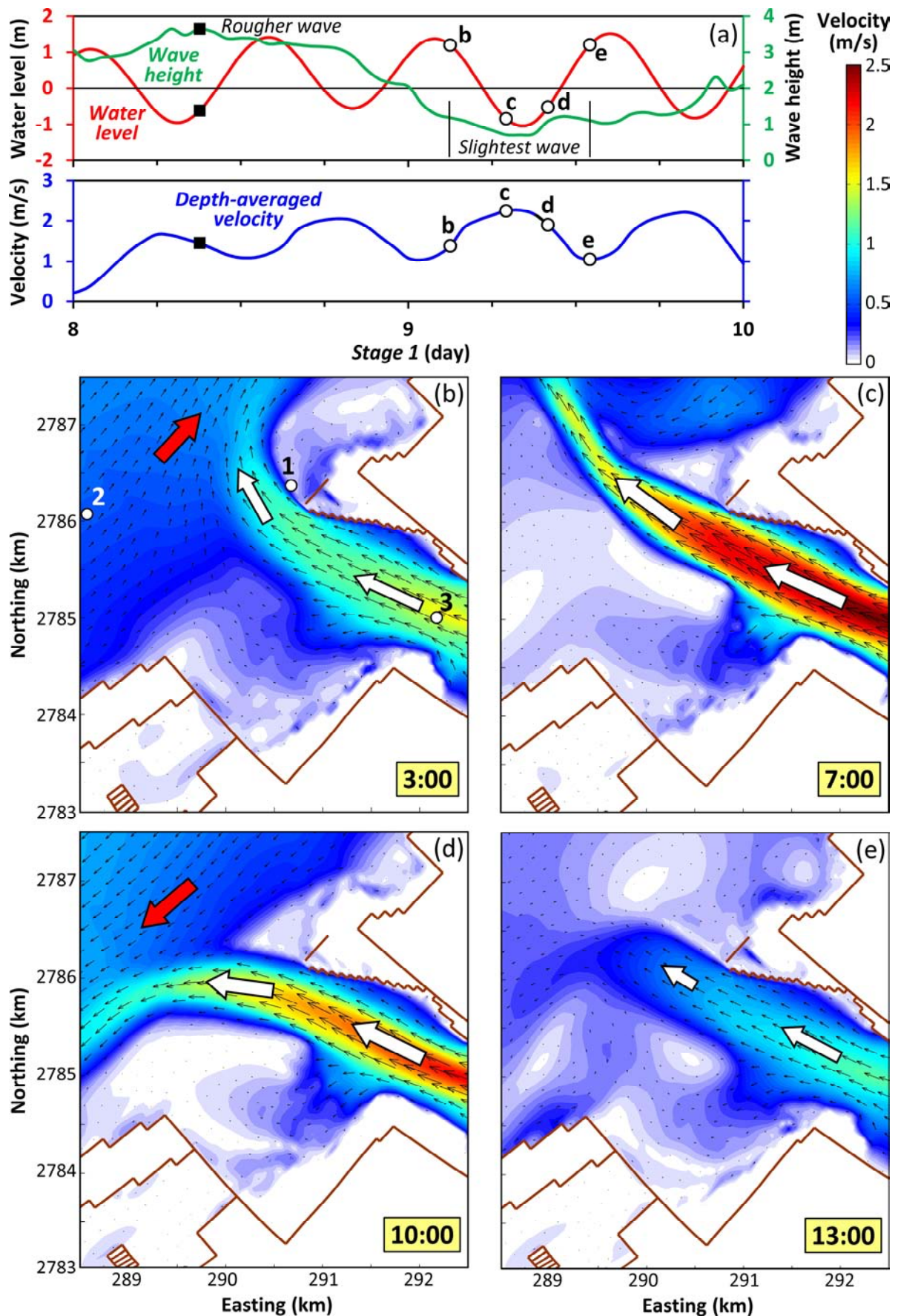


Figure S10. Swinging of exiting jet flow over a tidal cycle during Sinlaku (day 10, Stage 1). (a) Time series of simulated tide level at Tamsui River mouth gauge (labeled as 1 in (b)), wave height at Taipei Port (labeled as 2 in (b)), and velocity at mid-throat (labeled as 3 in (b)). (b-e) Flowfields in the mouth zone at 3:00, 7:00, 10:00 and 13:00 when the wave climate was slightest (labeled as b, c, d, e in (a)). White and red arrows indicate directions of jet flow and tidal current. The swinging of exiting jet flow was responsible for the fan-shaped deposit off the mouth (see Figures 4b-c).

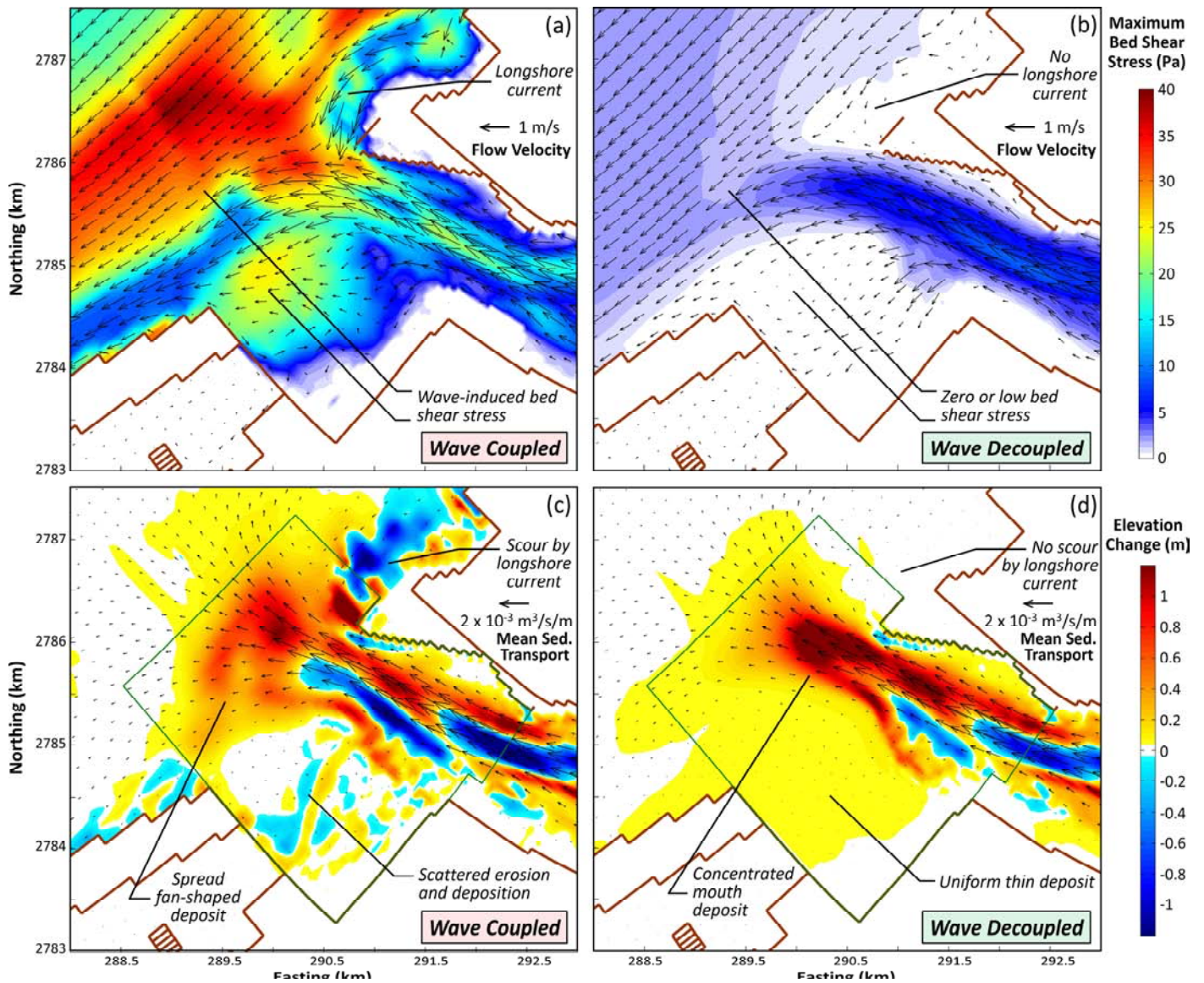


Figure S11. Comparison of simulation results with and without coupling Wave module. (a-b) Superimposed maximum bed shear stress field during Sinlaku and velocity field at 9:00, day 9 (Stage 1) when the wave climate was rougher (black squares, Figure S10a). (c-d) Superimposed bed elevation change and mean sediment transport field during Stage 1. Waves exerted additional bed shear stress that caused resuspension and transport of bottom sediments, spreading out an otherwise concentrated mouth deposit.

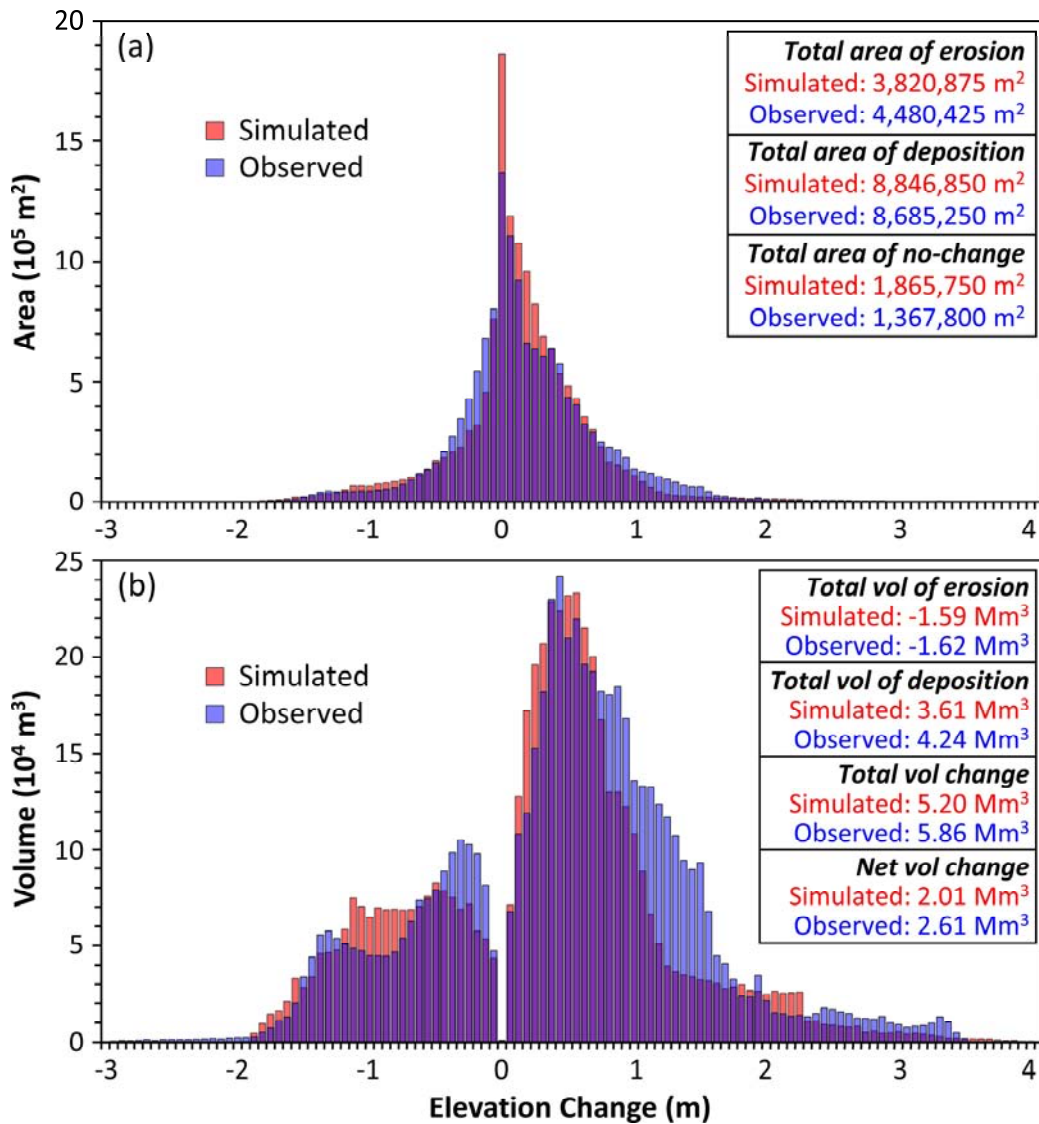


Figure S12. (a) Areal and (b) volumetric histograms of bed elevation change, derived from the observed and simulated differences between the pre- and post-Scenario 1 bathymetries of the validation area. Compared to the observed result, the model underestimated 0.66 km² of erosion area (4.5% of the validation area). In return, the model overestimated the areas of deposition and no-change by 1.1 and 3.4% of the validation area. The simulated total erosion volume of 1.59 Mm³ was 1.7% smaller than the observed 1.62 Mm³, while the simulated deposition volume of 3.61 Mm³ was 14.9% smaller than the observed 4.24 Mm³. The resulting deficits in the simulated *total volume change* (= sum of absolute volume changes) and *net volume change* (= deposition volume – erosion volume) were 0.66 and 0.60 Mm³, being 11 and 23% of the observed *total* and *net volume changes* (5.86 and 2.61 Mm³).

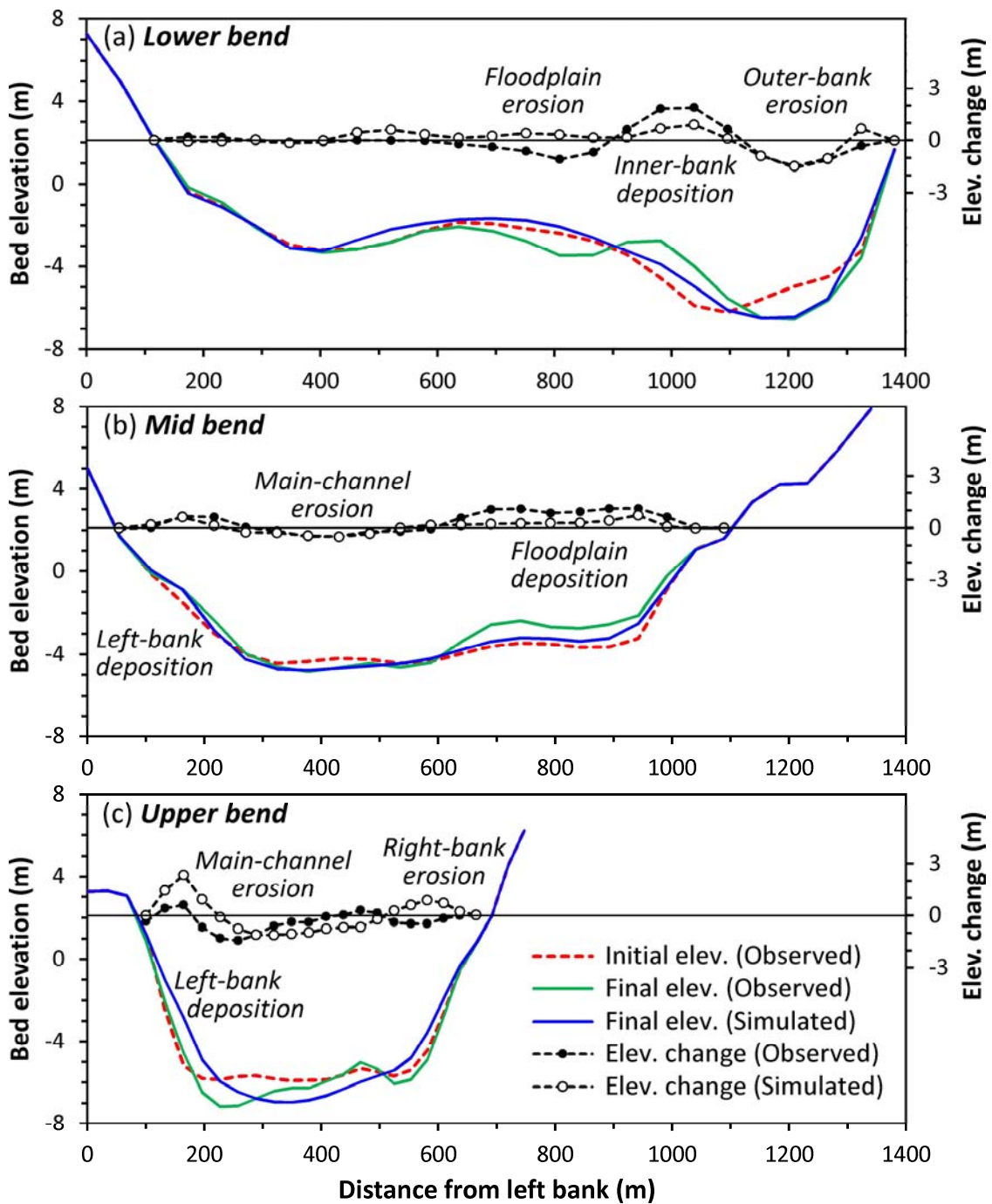


Figure S13. Observed and simulated profiles of bed elevation change between the pre- and post-Scenario 1 bathymetries at three cross-sections in the (a) lower bend (Bali Ferry Dock), (b) mid bend (Hongshulin), and (c) upper bend (Tudigonbi) of the estuary zone (see Figures 4b-4c for their locations). At the lower bend, the observed outer-bank erosion was well captured by the model, while the erosion over floodplain and inner-bank deposition were underestimated. At the mid bend, the main-channel scour and left-bank deposition were precisely reproduced, while the deposition over floodplain was underestimated. At the upper bend, the observed main-channel scour and left-bank deposition were reproduced, whereas the slight erosion at the right bank was not apparent.

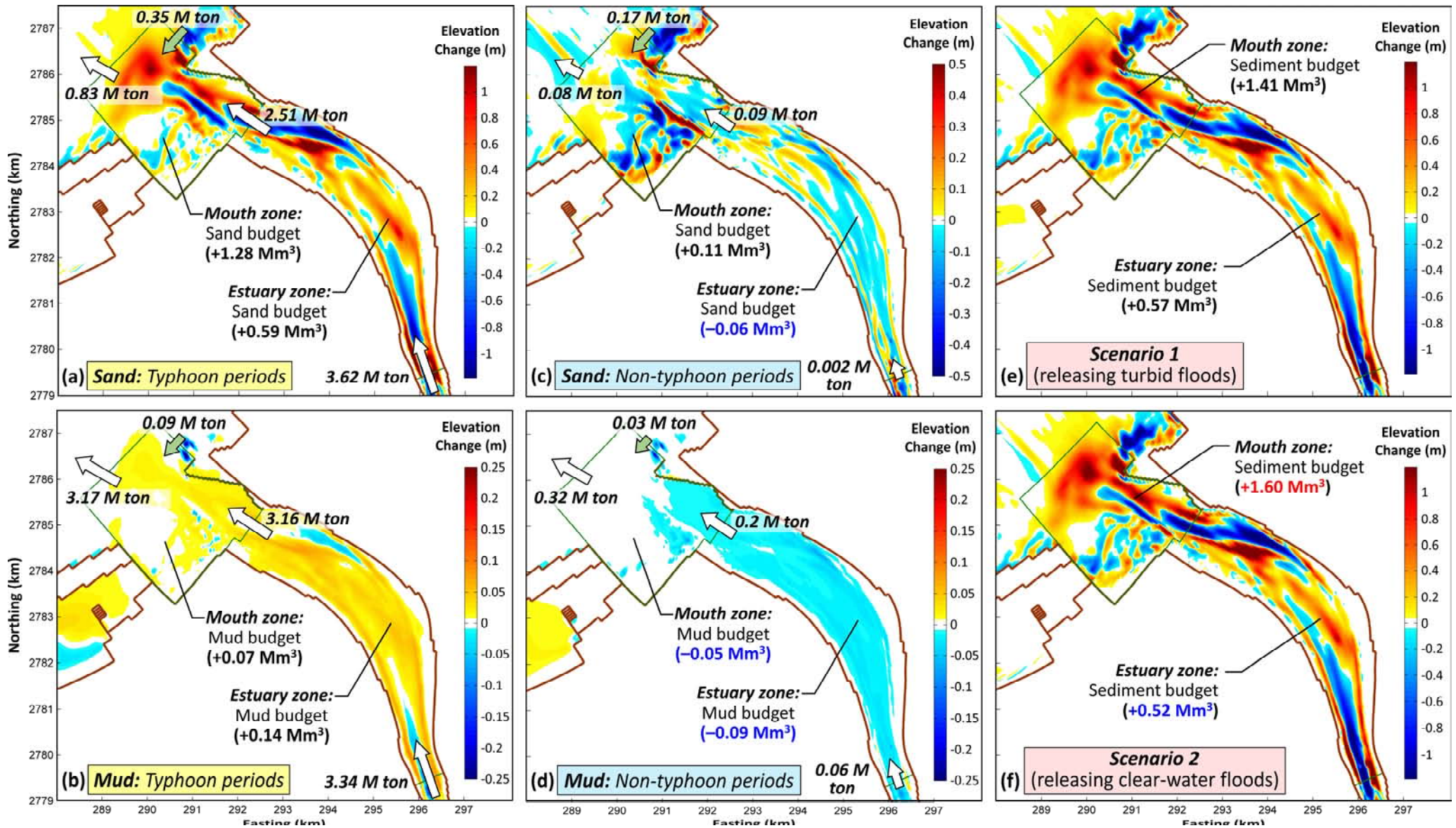


Figure S14. (a-d) Simulation results of Scenario 1 for sand and mud fractions during typhoon and non-typhoon periods (Stages 1 and 2): Bed elevation change, cumulative transports, and zonal budgets. White arrows indicate directions of transport by fluvial flows and tidal currents; green arrows indicate directions of transport by longshore currents. (e-f) Comparing the simulation results of Scenarios 1 and 2 (releasing turbid and clear-water floods): Bed elevation change and zonal sediment budgets. Bed elevation changes are highly similar, yet zonal sediment budgets are of notable difference.

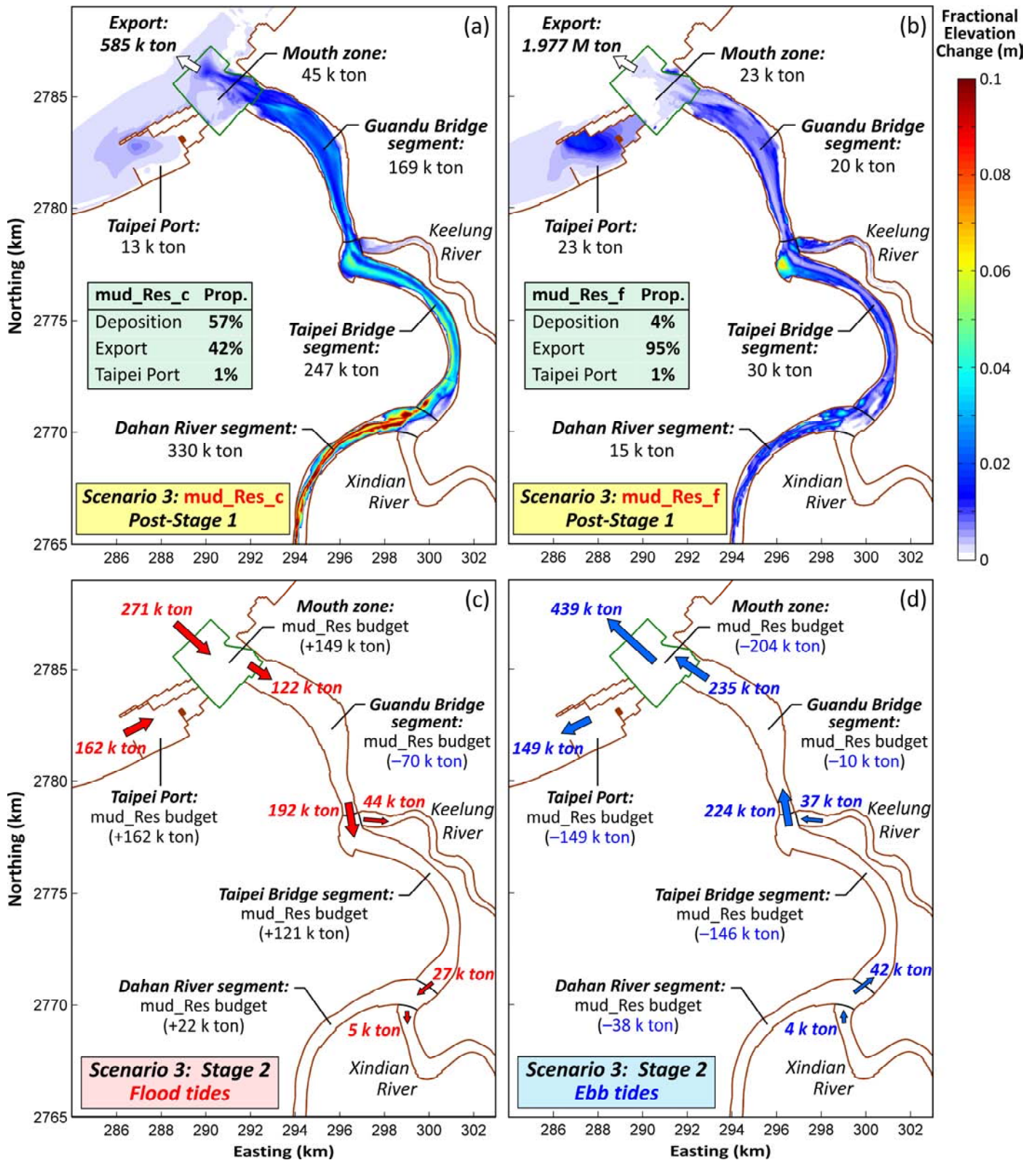


Figure S15. Spatiotemporal distributions of reservoir-released muds. (a-b) Post-Stage 1 bed elevation changes and zonal budgets of coarse and fine muds (`mud_Res_c` and `mud_Res_f`) in Dahan River segment, Taipei Bridge segment, Guandu Bridge segment, mouth zone, and Taipei Port. Proportions of `mud_Res_c` and `mud_Res_f` deposited in the study area, exported to offshore, and carried to the Taipei Port are summarized in inset tables. (c-d) Stage 2: cumulative transports and zonal budgets of total muds (`mud_Res`) during flood and ebb tides. Due to tidal asymmetry, residual transports of `mud_Res` were seaward.

Table S1. Global cases of reservoir sediment release. Red- and blue-shaded cases, respectively, had mud and sand/gravel as the main type of sediment released.

No.	Reservoir	River (Country)	Design capacity ¹	Frequency (year implemented)	Operation mode	Main type of sediment released (D_{50})	Coastal erosion	References
1	Agongdian	Agongdian (Taiwan)	36.7 Mm ³	Annually (2005-2015)	Drawdown sluicing	Mud (17 μ m)	Yes	<i>Chen & Tsai [2017]; Wang et al. [2018]</i>
2	Baira	Baira (India)	9.6 Mm ³	First flushing (1983)	Empty flushing	Mud (40 μ m)	No	<i>Chaudhry et al. [2014]</i>
3	Beauvoir, Saint-Hilaire, Pizançon, La-Vanelle, Beaumont-Monteux	Lower Isère (France)	11.8 Mm ³ , 6.8 Mm ³ , 13.8 Mm ³ , 3.9 Mm ³ , 3.3 Mm ³	2 concerted events (2008, 2015)	Empty flushing	Mixed: silt (40-15 μ m) and clay (4 μ m); sand (100-210 μ m)	Yes	<i>Camenen et al. [2019]</i>
4	Bodendorf, Fisching	Mur (Austria)	450 Km ³ , 800 Km ³	4 concerted events (1996-2012)	Empty flushing	Mud-gravel (10 μ m - 4.6 mm)	No	<i>Reckendorfer et al. [2019]</i>
5	Cachí	Reventazón (Costa Rica)	54 Mm ³	Annually since 1973 (1996)	Empty flushing	Mud (14 μ m)	No	<i>Brandt & Swenning [1999]</i>
6	Cancano	Upper Adda (Italy)	124 Mm ³	Annually (2010-2012)	Empty flushing	Mud (16 μ m)	No	<i>Espa et al. [2019]</i>
7	Carraízo (or Loíza)	Loíza (Puerto Rico)	26.8 Mm ³	Hurricane María (2017)	Drawdown sluicing	Mud (38 μ m)	Yes	<i>Gellis et al. [2006]; Morris [2020b]</i>
8	Cerro del Águila	Mantaro (Peru)	38.4 Mm ³	First flushing (2017)	Empty flushing	Mud (1 μ m)	Yes	<i>Rollo et al. [2018]</i>
9	Champagneux	Upper Rhône (France)	Run-of-river dam	Every 3 yrs (2016)	Empty flushing	Mud (10 μ m)	Yes	<i>Alliau et al. [2016]</i>
10	Chancy-Pougny (with Verbois & Génissiat)	Upper Rhône (Switzerland-France)	Run-of-river dam	Every 3 yrs (1945-2003); renewed strategy (2012)	Empty flushing	Mud (24 μ m)	Yes	<i>Lepage et al. [2020]</i>
11	Cherry Creek	Tributary South Platte (USA)	18.7 Mm ³	Annually since early 1980s	Pressure flushing	Mud (n/a) ²	No	<i>Shelley et al. [2022]</i>
12	Dashidaira, Unazuki	Kurobe (Japan)	9.01 Mm ³ , 24.7 Mm ³	Annual concerted events since 2001	Empty flushing	Mud (35 μ m)	Yes	<i>Sumi et al. [2007]; Sumi [2008]</i>
13	Dez	Dez (Iran)	3.3 Bm ³	Several times since 1963 (2000)	Pressure flushing	Mud (< 10 μ m)	No	<i>Moridi & Yazdi [2017]</i>
14	Fall Creek	Middle Fork Willamette (USA)	142 Mm ³	Annually since 2012 (2012-2016)	Empty flushing	Sand (0.3 mm)	No	<i>Schenk & Bragg [2014]; Gibson & Crain [2019]</i>
15	Gebidem	Massa (Switzerland)	9.2 Mm ³	Annually since 1969 (1969-2013)	Empty flushing	Mixed: sand and gravel (1.7 mm)	No	<i>Meile et al. [2014]</i>
16	Génissiat	Upper Rhône (France)	56 Mm ³	17 events since 1955 (1997-2012)	Empty flushing	Mud (32 μ m)	Yes	<i>Guertault et al. [2014, 2018]</i>
17	Gmünd (with Durlassboden)	Gerlosbach (Austria)	930 Km ³	Annual concerted events since 1967	Empty flushing	Sand-gravel (1-30 mm)	No	<i>Leobacher & Blauhut [2010]; White [2001]</i>
18	Grangent	Upper Loire (France)	57 Mm ³	1 event (1995-96)	Empty flushing	Mud (12 μ m)	No	<i>Marot et al. [2005]; Dhivert et al. [2015]</i>
19	Guernsey	North Platte (USA)	97.2 Mm ³	Annually since 1959	Empty flushing	Mud (16 μ m)	No	<i>Shelley et al. [2022]</i>
20	Halligan	North Fork Poudre (USA)	8 Mm ³	An episodic event (1996)	Empty flushing	Mud (16 μ m)	No	<i>Wohl & Cenderelli [2000]</i>
21	Heisonglin	Yeyu (China)	8.6 Mm ³	Annually since 1962	Empty flushing	Mud (25 μ m)	No	<i>White [2001]; Zhou [2007]</i>
22	Hengshan	Tangyu (China)	13.3 Mm ³	Every 3-5 yrs (1974-86)	Empty flushing	Mud (20 μ m)	No	<i>White [2001]</i>
23	Howard Hanson	Green (USA)	32.1 Mm ³	3 events (2003, 2004, 2007)	Empty flushing	Mud-sand (16-125 μ m)	No	<i>Eriksen & Easthouse [2010]</i>
24	Ichari	Tons (India)	11.6 Mm ³	Annually since 1976	Empty flushing	Gravel-cobble (n/a) ²	No	<i>White [2001]</i>
25	Joaquín Costa (or Barasona)	Ésera (Spain)	92 Mm ³	Annually (1950s); 3 events (1995-98)	Empty flushing	Mud (15 μ m)	No	<i>Avendaño-Salas et al. [2000]</i>
26	Khashm El-Girba	Atbara (Sudan)	1.32 Bm ³	Annually since 1971 (34 events, 1971-2009)	Drawdown sluicing + Empty flushing	Mud (22 μ m)	No	<i>Adam & Suleiman [2022]</i>
27	Langmann	Teigitsch (Austria)	320 Km ³	Annually (2006-2009)	Empty flushing	Sand (0.14 mm)	No	<i>den Boer [2011]</i>

Table S1. (continued)

No.	Reservoir	River (Country)	Design capacity ¹	Frequency (year implemented)	Operation mode	Main type of sediment released (D_{50})	Coastal erosion	References
28	Madesimo	Liro (Italy)	130 Km ³	1 event (2010)	Empty flushing	Mud (33 μ m)	No	<i>Espa et al.</i> [2019]
29	Mangahao (Storage #2)	Mangahao (New Zealand)	2.01 Mm ³	Annually since 1969 (1969)	Empty flushing	Mud (< 40 μ m)	No	<i>Milne</i> [1969]; <i>White</i> [2001]
30	Nanqin	Nanqin (China)	10.2 Mm ³	Every 3-4 yrs since 1984	Empty flushing	Mixed: mud and sand (< 75 μ m)	No	<i>White</i> [2001]; <i>Zhuang et al.</i> [2021]
31	Naodehai	Liu (China)	193 Mm ³	Annually since 1971 (1995-98)	Drawdown sluicing	Mud-sand (6-189 μ m)	No	<i>Xia & Liu</i> [2003]; <i>Zhang et al.</i> [2004]
32	Nathpa Jhakri	Sutlej (India)	343 Mm ³	Annually since 2005	Empty flushing	Mud (n/a) ²	Yes	<i>IHA</i> [2022]
33	Paonia	Muddy Creek (USA)	25.8 Mm ³	First flushing (2016)	Empty flushing	Mud (25 μ m)	No	<i>Shelley et al.</i> [2018]; <i>Huang et al.</i> [2019]
34	Pulangi	Pulangi (Philippines)	67 Mm ³	First flushing (2007)	Drawdown sluicing	Mixed: sand and mud (0.2 mm)	Yes	<i>Tabios</i> [2020]
35	Rio di Pusteria	Rienz (Italy)	1.7 Mm ³	Every 2+ yrs since 2001 (2014, 2019)	Empty flushing	Mixed: mud and sand (83 μ m)	No	<i>Kaffas et al.</i> [2021]; <i>Folegot et al.</i> [2021]
36	Roccasparvera	Stura di Demonte (Italy)	580 Km ³	An emergency flushing (2016)	Empty flushing	Mud (n/a) ²	No	<i>Doretto et al.</i> [2019]
37	Saigo, Ouchibaru	Lower Mimi (Japan)	2.45 Mm ³ , 7.49 Mm ³	First concerted event (2017)	Drawdown sluicing	Sand (1 mm)	Yes	<i>Sumi et al.</i> [2015]; <i>Nukazawa et al.</i> [2020]
38	Saint-Egrève, six Lower Isère	Isère (France)	Run-of-river dams	2 concerted events (2008, 2010)	Sluicing + Flushing	Mud (34 μ m)	No	<i>Peteuil et al.</i> [2018]; <i>Launay et al.</i> [2019]
39	Saint-Martin-La-Porte	Arc (France)	68 Km ³	Annually (2012, 2016)	Empty flushing	Mud (21 μ m)	No	<i>Besnier et al.</i> [2016]; <i>Legout et al.</i> [2018]
40	Sanmenxia	Yellow (China)	9.75 Bm ³	Annually since 1973	Sluicing + Flushing	Mud (30 μ m)	Yes	<i>White</i> [2001]; <i>Wang et al.</i> [2005]
41	Santa María	Samalá (Guatemala)	216 Km ³	Annually since 2009 (2009-17)	Empty flushing	Mud (19 μ m)	Yes	<i>Zamora</i> [2018]
42	Santo-Domingo	Santo-Domingo (Venezuela)	3 Mm ³	First flushing (1978)	Empty flushing	Mud (46 μ m)	No	<i>Chaudhry et al.</i> [2014]
43	Sefidrud	Sefid-Rud (Iran)	1.8 Bm ³	Annually since 1981 (1981-90)	Empty flushing	Mud (n/a) ²	Yes	<i>Hassanzadeh</i> [1995]; <i>Espa et al.</i> [2019]
44	Sernio	Upper Adda (Italy)	700 Km ³	Annually (2009, 2010)	Empty flushing	Mixed: mud and sand (93 μ m)	No	<i>Espa et al.</i> [2019]
45	Setoishi	Kuma (Japan)	9.93 Mm ³	Annually since 2016 (2018)	Sluicing + Flushing	Mud (50 μ m)	No	<i>Furukawa et al.</i> [2019]
46	Shihmen	Dahan (Taiwan)	309 Mm ³	During flood since 2008; added mud sluiceway (2012)	Turbidity current venting	Mud (5.7 μ m)	Yes	<i>Wang et al.</i> [2018]; <i>Lee et al.</i> [2022]
47	Shuicaozi	Yili (China)	9.58 Mm ³	8 events (1964-1981)	Sluicing + Flushing	Mud (5 μ m)	No	<i>Yang</i> [2003]
48	Spencer	Niobrara (USA)	12.9 Mm ³	Twice a year since 1950s (until 2019)	Empty flushing	Sand (0.25 mm)	No	<i>Shelley et al.</i> [2022]; <i>Gibson & Boyd</i> [2016]
49	Three Gorges	Yangtze (China)	39.3 Bm ³	Annually since 2012 (2012-19)	Drawdown sluicing	Mud (44 μ m)	Yes	<i>Ren et al.</i> [2021]; <i>Liu et al.</i> [2022]
50	Üch-Korgon	Naryn (Kyrgyzstan)	56.4 Mm ³	Annually since 1963	Empty flushing	Mud (n/a) ²	No	<i>White</i> [2001]; <i>OJSCEPP</i> [2018]
51	Valgrosina	Upper Adda (Italy)	1.3 Mm ³	Annually (2006-2009)	Empty flushing	Mud (15 μ m)	No	<i>Espa et al.</i> [2019]
52	Vaussaire	Rhue (France)	1.5 Mm ³	Every 1-3 yrs (2003-2015)	Drawdown sluicing	Mud (49 μ m)	No	<i>Frémion et al.</i> [2016a, 2016b]
53	Verbois	Rhône (Switzerland)	13 Mm ³	Every 3 yrs (1969-2003); renew (2016)	Empty flushing	Mud (24 μ m)	Yes	<i>Lepage et al.</i> [2020]; <i>Cattanéo et al.</i> [2021]
54	Warsak	Kabul (Pakistan)	170 Mm ³	5 events (1976-1979)	Empty flushing	Mud (31 μ m)	No	<i>Chaudhry</i> [1982]; <i>White</i> [2001]
55	Xiaolangdi	Yellow (China)	12.7 Bm ³	Annual WSRS since 2002	Empty flushing	Mud (15 μ m)	Yes	<i>Yu et al.</i> [2013]; <i>Wang et al.</i> [2017]
56	Zengwen	Zengwen (Taiwan)	748 Mm ³	Annually (2010-2015); added new tunnel (2018)	Turbidity current venting	Mud (n/a) ²	Yes	<i>Wang et al.</i> [2018]; <i>Morris</i> [2020a]

¹ Km³: kilo (= 10³) cubic meters; Mm³: million (= 10⁶) cubic meters; Bm³: billion (= 10⁹) cubic meters.² n/a: median grain size D_{50} not available from literature.

Table S2. Calibrated parameter values of the Flow and Morphology Modules

Module	Parameter	Value	Remark
Flow	Manning's roughness coefficient, n	0.025–0.03 (Dahan River) 0.02–0.035 (Xindian River) 0.03–0.045 (Keelung River) 0.018 (estuary, nearshore) 0.045 (floodplain)	Based on suggested values for Tamsui River estuarine system [TRMO, 2014]
	Horizontal eddy diffusivity D_H and eddy viscosity ν_H	$D_H = 1 \text{ m}^2/\text{s}$ (estuary, nearshore) $D_H = 5 \text{ m}^2/\text{s}$ (rivers) $\nu_H = 1 \text{ m}^2/\text{s}$	Based on suggested ranges [Deltares, 2014a]
Morphology	Sediment fractions	Coarse sand: $D_{50} = 500 \mu\text{m}$ Medium sand: $D_{50} = 200 \mu\text{m}$ Fine sand: $D_{50} = 100 \mu\text{m}$ Coarse mud: $w_s = 0.26 \text{ mm/s}$ Fine mud: $w_s = 0.011 \text{ mm/s}$	Sands: field data [TRMO, 2015]. Muds: sensitivity tests that best reproduced the observed SSC and deposition [WRPI, 2008]
	Critical shear stress for mud erosion, τ_E	0.1 Pa	From Tamsui River estuary model [Liu <i>et al.</i> , 2002]
	Mud erosion rate constant, M	$2 \times 10^{-5} \text{ kg/m}^2/\text{s}$	Calibration based on Zhu & Wiberg [2022]
	Critical flow depth for sediment motion	0.25 m	2.5 times the default value (to avoid excessive erosion)
	Bed stratigraphy	Surface layer: 0.2 m thick 10 underlayers: each 1 m thick	Based on values suggested for similar sediments [van der Wegen <i>et al.</i> , 2011b]
	Sediment grain density (SGD); Dry bed density (DBD)	SGD: $2,650 \text{ kg/m}^3$ DBD (sands): $1,600 \text{ kg/m}^3$ DBD (coarse mud): $1,060 \text{ kg/m}^3$ DBD (fine mud): 200 kg/m^3	Calibrated values based on suggested ranges for similar sediments [van Rijn, 2007, 2013; Deltares, 2014a]